Fall 2013

Computational Fluid Dynamics (cfd) Modeling of a Laboratory Scale Coal Gasifier

Kiel S. Schultheiss

Recommended Citation

Schultheiss, Kiel S., "Computational Fluid Dynamics (cfd) Modeling of a Laboratory Scale Coal Gasifier" (2013). *Electronic Theses and Dissertations*. 894.
https://digitalcommons.georgiasouthern.edu/etd/894

COMPUTATIONAL FLUID DYNAMICS (CFD) MODELING OF A LABORATORY SCALE COAL GASIFIER

by

Kiel Schultheiss

(Under Direction of Cheng Zhang)

Abstract

Furthering gasification technology is an essential part of advancing clean coal technologies. In order to seek insight into the appropriate operations for the formation of synthetic gas (syngas) a numerical simulation was performed to predict the phenomena of coal gasification in a laboratory scale entrained-flow coal gasifier. The mesh for the model was developed with ICEM CFD software and the chemical and physical phenomena were modeled using the fluid flow solver ANSYS FLUENT. Mesh independence was verified. The model was validated with experimental data from several studies performed on a laboratory scale gasifier.

Systematic examination of the model was performed by varying primary and secondary inlet concentrations of steam and oxygen in regular intervals. Studies were also performed to investigate the effects of coal particle size and steam preheat temperatures. The effect of the turbulence model was also investigated by employing two turbulence models.

Of the two turbulence models used the standard k-ε model showed the best agreement with experimental data. Model predictions found that increasing the steam concentration or preheat temperatures in the secondary inlet generally decreases CO production, while increasing CO_2 and H_2 concentrations. Increasing the steam content in the secondary inlet showed no signifigants effects on predicted temperatures in the gasifier. Increasing the oxygen concentration in the primary inlet generally increases exit temperatures, CO, and CO_2 production, while decreasing H_2 concentrations.It was found that decreasing the particle size increases the , CO, and H_2 concentration, while decreasing the CO_2 concentrations.

COMPUTATIONAL FLUID DYNAMICS (CFD) MODELING OF A LABORATORY SCALE COAL GASIFIER

by

Kiel S. Schultheiss

B.S., Georgia Southern University, 2010

A Thesis Submitted to the Graduate Faculty of Georgia Southern University in
Partial Fulfillment of the Requirements for the Degree

MASTER OF SCIENCE

STATESBORO, GEORGIA

2013

COMPUTATIONAL FLUID DYNAMICS (CFD) MODELING OF A LABORATORY SCALE COAL GASIFIER

by

KIEL S SCHULTHEISS

Major Professor: Cheng Zhang

Committee: Anirudda Mitra

Mosfequr Rahman

TABLE OF CONTENTS

Chapter

LIST OF FIGURES

Figure Page

LIST OF TABLES

Table Page

CHAPTER 1

INTRODUCTION

1.1 Brief History of World Energy Consumptions

The global demand for energy is increasing dramatically. It is expected to rise 50% in the next 25 years. The majority of the world's energy demand is predominately supplied by hydrocarbon fuels, which contribute over 90% of the world's energy requirements [1]. Coal is an essential source of energy, contributing to 25.1% of the world's total energy consumption. Over 40% of the world's electricity is supplied by coal. As the world's finite amount of fossil fuel and biomass reserves and resources dwindle, economics will drive a shift in the demand and use of these resources. The lifetime of oil reserves is expected to last 50 to 75 years with 150 years of resources. Natural gas is expected to last about twice that long. In comparison coal is abundant and is expected to last for hundreds of years [1].

1.2 Characteristics of Coal

Coal's ready availability and subsequent lower costs is driving a greater demand for coal energy. The use of coal is expected to increase 48% from 2006 to 2030 [2]. Fig. 1 shows the Energy Information Administrations (EIA) prediction for the increase in worldwide energy demand.

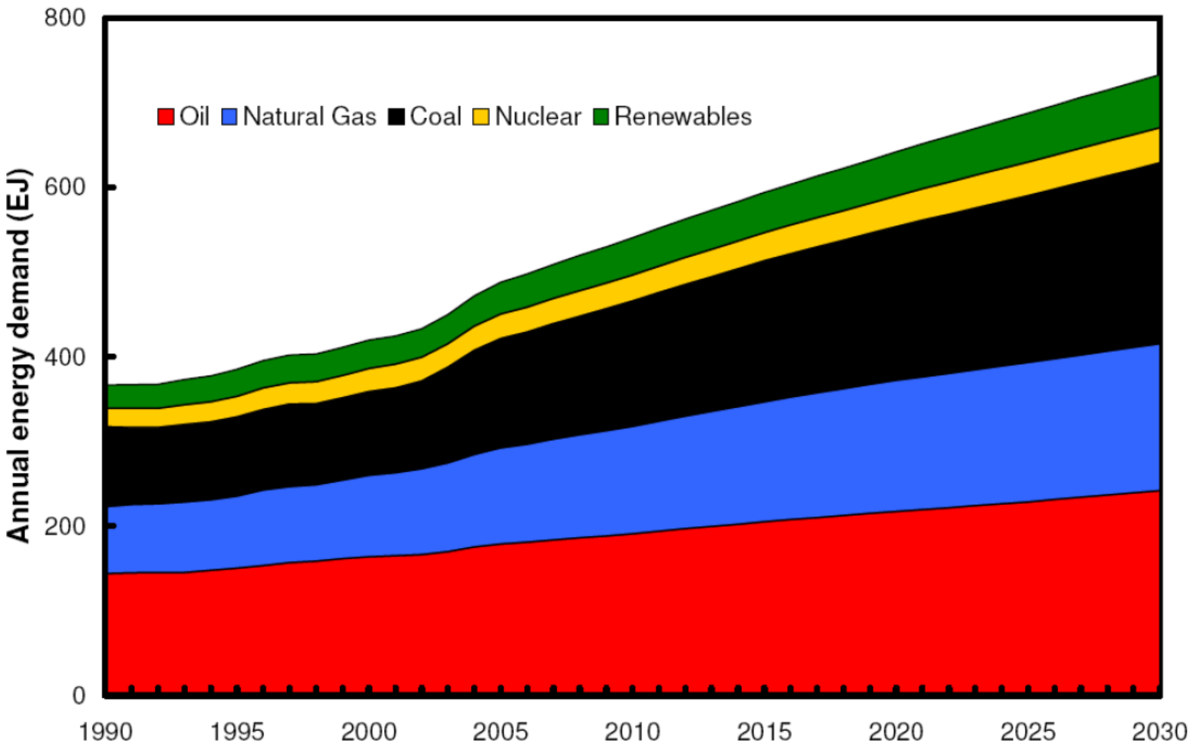

Figure 1: EIAs world energy demand prediction [2].

Unfortunately coal power plants are the single largest source of CO_2 emissions worldwide [1]. Coal power production is about 50% as efficient as oil. For example oil, has on average1 toe/tonne, while coal has almost 0.5 toe/tonne (in conventional energy units, 1 Mtoe = 41,868 TJ) [1]. Fig. 2 illustrates the predicted rise in CO_2 emissions from coal.

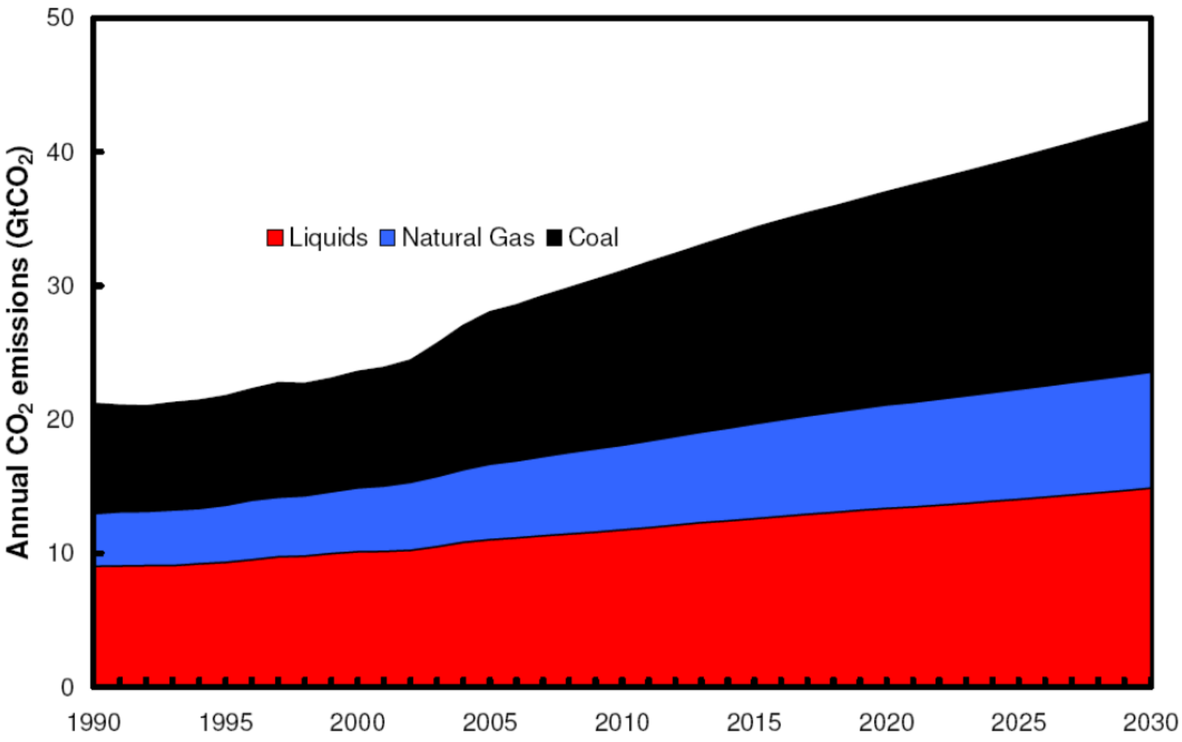

Figure 2: EIAs world CO_2 emissions prediction [2].

1.3 Coal Gasification Process

Gasification is the process of turning carbonaceous fuels (coal or biomass) into a gaseous product that can be turned into chemical feedstocks, containing a mixture of carbon monoxide and hydrogen. The process typically involves reacting the fuel with a limited amount of oxygen, steam or less often air at high temperatures. The gasification process can be generally described in four basic steps.

1. First directly after injection, the feedstock heats up, then undergoes pyrolysis which releases moisture and volatiles bound in the feedstock. This is called devolatilization and is represented by the following reaction:

$$feedstock \rightarrow Char + Volatiles + tar$$

2. Then the volatiles combust with an injected oxidant called the "gasification agent" (Kumar, 2011) generating heat and producing CO_2 and H_2O. The gas phase reactions include:

$$CO + 0.5O_2 \rightarrow CO_2$$

$$H_2 + 0.5O_2 \rightarrow H_2O$$

3. The devolatized feedstock particles then react with O_2, CO_2 and H_2O present in the mixture to produce synthetic gas called syngas, which consists of H_2 and CO. The heterogeneous reactions include:

$$C + \frac{1}{2}O_2 \rightarrow CO$$

$$C + CO_2 \rightarrow 2CO$$

$$C + H_2O \rightarrow CO + H_2$$

4. After the production of the syngas the water gas shift reaction, shown below, continues in the gas phase. This helps balance the major gas phase species in the aft section of the reactor.

$$CO + H_2O \Leftrightarrow CO_2 + H_2$$

There are several advantages to coal gasification. Using syngas is more efficient than simply combusting the coal. There is more feedstock and product flexibility including applications for renewable biomass. Also, harmful emissions such as NO_x, SO_x, and CO_2 are also reduced.

1.4 Brief History of Gasification

The process of coal gasification was first discovered by an Italian Priest and professor of physics, Felice Fontana. He states in his 1780 laboratory book "If one quenches glowing coal with distilled water one obtains ignitable air [3]." Coal gasification was first used commercially in 1812 to produce "town gas" for street lamps [4].

1.5 Types of Coal Gasification

There are three major types of gasifiers fixed bed, fluidized bed, and entrained flow.

Fixed bed gasifiers are comprised of a fixed bed of coal or biomass where the gasification agent flows in a counter-current or co-current configuration. This type of gasifier must use a fuel with high mechanical strength and must be non-caking in order to form a permeable bed. For this reason the throughput is relatively low for the fixed bed gasifier. Gas exit temperatures are relatively low which means a high thermal efficiency. Lower exit temperatures increase tar and methane production therefor product gas must be extensively cleaned.

Fluidized bed gasifiers use fuel that is fluidized in air, oxygen or steam. The ash is removed dry or as heavy agglomerates that defluidize in the bed. In dry ash gasifiers the temperatures are relatively low therefore the fuels must be highly reactive. This makes low grade fuels particularly suitable for fluidized bed gasifiers. Fuel throughput is greater than fixed bed but less than the entrained flow gasifier.

Entrained flow gasification uses a dry pulverized solid that forms an atomized liquid fuel slurry which is gasified with air, oxygen or steam. Entrained flow gasifiers are characterized by relatively higher temperatures, allowing a higher throughput to be achieved. Because the coal particles are separated so well from one another most coals are suitable for entrained flow gasification. However due to higher temperatures in the gasifier the thermal efficiency is lower as the product gas must be cooled before it can be cleaned. Higher temperatures also mean no methane or tar is not present in the product gas but the oxygen requirement is relatively higher. Although energy is consumed milling the feedstock into pulverized coal, the majority of the energy consumed comes from the production of oxygen for gasification [5]. The major advantages to entrained flow gasification over other gasification processes are:

1. Feedstock flexibility: Nearly any type of coal can be used without regard to physical properties; also biomass can be used as feedstock.
2. Higher CO/CO_2 ratio is possible.
3. Higher potential through puts are possible.
4. Lower amounts of tars and heavy hydrocarbons are formed.
5. Carbon conversion approaches 100%.
6. Mechanical design is simpler
7. The product gas contains relatively low methane content; making it better suited for processing into liquid fuels.

According to the DOE/NETL 2007 database, all but one of gasification plants planned worldwide will employ gasifiers of the entrained flow type [6]. Accordingly, the present study focuses on the modeling and analysis of the entrained-flow gasification process only.

1.6 Description and applications of CFD modeling

The evolution of gasifier design has been based more out of operational expediency than rigorous understanding of relevant physical phenomena [4]. Most if not all industrial gasifiers were designed before computational fluid dynamic (CFD) models were developed or practical for application. CFD models developed in the past have lacked accurate sub-models to predict the detailed physics and chemistry of the coupled nonlinear phenomena occurring during solid fuel gasification. Predicting gasification involves the coupling of several physical, chemical and dynamic phenomena. This includes devolatilization, turbulent mixing, homogeneous and heterogeneous reactions, radiative and convective heat transport, etc. Fluid (gas and liquid) flows are governed by partial differential equations (PDE) which represent conservation laws for the mass, momentum, and energy. Computational Fluid Dynamics (CFD) is the art of replacing such PDE systems by a set of algebraic equations which can be solved using digital computers. CFD systems contain elaborate sub models that can be used to understand the physical and chemical processes in the gasifier, optimize gasifier design and invent novel gasification methods and concepts. Fig. 3 shows a block diagram representing components of a CFD model and their interactions.

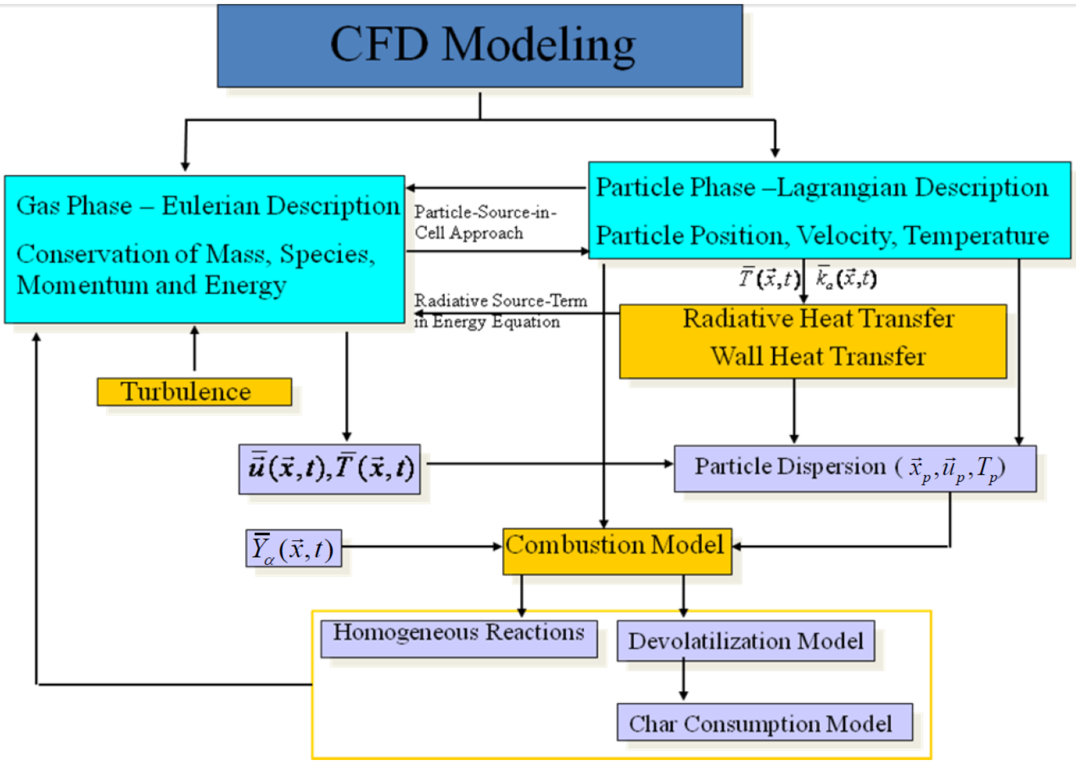

Figure 3: Block diagram representing components of a CFD model and their interactions [7].

CFD modeling can be used to help resolve injector and refractory liner failure, efficient space utilization, addressing high capital costs and optimization of gasifier operating conditions. This thesis focuses on optimization of entrained flow gasifier operating conditions, in particular the effects of steam and oxygen.

CHAPTER 2

BACKGROUND AND MOTIVATION

During World War II Germany performed extensive research on coal gasification when their petroleum supply lines were cut off. After WWII, Africa continued the development of coal gasification technologies, where it supplied up to 50% of their fuel needs [8] . Though the U.S. market had shifted away from coal gasification, as natural gas became a more popular fuel source, some coal gasification research continued in the U.S. In 1945 the Bureau of Mines Morgantown Research Center began their coal research. In 1950 they began researching the coal gasification process. Between 1953 and 1962 the Bureau of Mines extensively researched pressurized gasification of coal in an experimental entrained flow reactor [9] [10]. A laboratory-scale gasifier similar to the Bureau of Mines gasifier was studied by the Eyring Research Institute from 1974 to 1978 [11] [12].

As natural gas was abundant, cheaper, and cleaner than coal, the United States for the most part did not revisit coal gasification as an alternative energy research until the energy crisis of the 1970s, where the price of oil skyrocketed. The energy crisis sparked a new era of gasification research. Research facilities across the U.S. began to study coal gasification. This research included the effects of an array of parameters including the effects of gasifier type and design, pressure, particle size, feedstock type, mass throughput, coal rank etc. as well as further investigating various phenomena associated with coal gasification and combustion such as devolatilization, pyrolysis, and heterogeneous reaction rates. Coal devolatilization has been studied extensively including research by: Batchelder et al. (1953), Howard and Essenhigh (1967), Anthony and Howard (1976), Suuburg et al. (1978, 1979), Solomon and Colket (1979), and Howard (1981) [13]. These studies found the total amount of volatile mater for a certain coal type to be a strong function of the final temperature. The heating rate was of minor importance. Nakles et al. reported in 1982 that temperature is a major factor in coal devolatilization [14]. Solomon and Hamblen found that coal type alone had little influence on coal pyrolysis kinetics. Extensive process design for the Bureau of Mines gasifier system was performed by Mountain Fuel Resources (MFI) [15].

Brigham Young University (BYU) researchers started studying entrained-flow gasification in the 1970s. Skinner built a laboratory scale reactor in 1980. Skinner used gas and particle samples obtained from inside the reactor to study the details of pulverized coal gasification. Skinner found that increased coal moisture from steam added into the secondary inlet lowered predicted carbon conversion and hydrogen concentration [16]. In 1982 and ‘83 experimental test programs were conducted by Highsmith and Soelburg respectively to provide detailed internal maps from the BYU gasifier using Utah bituminous coal at atmospheric pressure [13]. In 1984 Azuhata investigated the effects of pressure, flame type, particle size, coal feed rate, and the effects of steam. Brown furthered this study extensively by researching the effects of steam coal volatile mater, steam partitioning, steam/coal ratio, oxygen/carbon (O/C) ratio, coal feed rate, particle size, conversion of particles within a distribution, and variation in mass mean particle size among coal type [13]. Brown found that increasing the steam input in either the primary or secondary had detrimental effects on carbon conversion, the carbon monoxide/carbon dioxide ratio, and the hydrogen concentration.

In accompaniment to experimental techniques, computational fluid dynamic (CFD) software has become a powerful tool to investigate and optimize the gasification process. Many attempts have been made at computer modeling gasification systems. One dimensional models were formulated for entrained-bed gasifiers by Ubhayaker in 1977, Sprouse in 1980, Beck in 1980 and Smith and Smoot in 1980 [13]. For a very limited amount of these cases the codes produced generally good agreement with experimental data. Wen and Chaung developed a one-dimensional model to research the operation of the Texaco pilot-scale gasifier under various operating conditions [17]. In 1979 and ’80 respectively Smith et al. and Fletcher developed a series of two-dimensional axisymmetric and 3-D models for gasification and combustion. [13] Chen et al. conducted research on the effects of the heterogeneous reaction rate, coal type, particle size, air/coal partitioning to the two stages, throat, diameter ratio and swirl ratio by constructing a CFD model of a pilot-scale two-stage air-blown entrained flow gasifier [18] [19]. Watanabe and Otaka perfomed CFD modeling of a research-scale Mitsubishi Heavy Industries (MHI) gasifier in order to study the effects of the O/C ratio and coal type [20]. Kumar performed a multi-scale gasification model emphasizing on the development and validation of key submodels. Kumar used the CFD package ANSYS FLUENT to analyze the most popular CFD submodels [7]. Zhang studied the effects of the equivalence ratio, particle size, and swirl using a similar numerical model of coal gasification in an entrained flow gasifier based of off the BYU gasifier design [21]. The objective of Kumar’s and Zhang’s research was to build confidence in the predictive capability of their numerical models.

CHAPTER 3

METHOD

Chapter 3 describes the theory and governing equations of the CFD model considered in this study. ANSYS FLUENT 13.0 CFD software was used to model following physical and chemical processes: turbulent flow of the gas phase, particle tracking including turbulent dispersion, devolatilization and heterogeneous reactions of the particle phase, turbulent combustion of the gas phase, and radiative heat transfer.

The equation for conservation of mass called the continuity equation is given by,

$$\frac{\partial \rho}{\partial t} + \nabla \cdot (\rho \vec{v}) = S_m \tag{1}$$

where the source term S_m is the mass added to the continuous phase from the dispersed second phase.

The equation for the conservation of momentum is given by

$$\frac{\partial}{\partial t}(\rho \vec{v}) + \nabla \cdot (\rho \vec{v}\vec{v}) = -\nabla p \ + \nabla \ \cdot (\bar{\bar{\tau}}) + \rho \vec{g} + \vec{F} \tag{2}$$

where p is the static pressure, $\bar{\bar{\tau}}$ is the stress tensor defined below. $\rho \vec{g}$ and $\vec{F}$ are the gravitational and external body forces.

The stress tensor, $\bar{\bar{\tau}}$, is given by

$$\bar{\bar{\tau}} = \mu[(\nabla \vec{v} + \nabla \vec{v}^T) - \frac{2}{3} \nabla \cdot \vec{v} \bar{\bar{I}}] \tag{3}$$

where μ is the molecular viscosity, $\bar{\bar{I}}$ is the unit tensor, and $\nabla \cdot \vec{v}$ is the effect of volume dilation. The radial and axial momentum conservation equations for two dimensional axisymmetric geometries are given by

$$\frac{\partial}{\partial t}(\rho v_x) + \frac{1}{r}\frac{\partial}{\partial_x}(r\rho v_x v_x) + \frac{1}{r}\frac{\partial}{\partial r}(r\rho v_r v_x)$$

$$= -\frac{\partial p}{\partial x} + \frac{1}{r}\frac{\partial}{\partial x}\left[r\mu\left(2\frac{\partial v_x}{\partial x} - \frac{2}{3}(\nabla \cdot \vec{v})\right]\right. + \frac{1}{r}\frac{\partial}{\partial r}\left[r\mu\frac{\partial v_x}{\partial r} + \frac{\partial v_r}{\partial x}\right)\left.\right] + F_x \tag{4}$$

$$\frac{\partial}{\partial t}(\rho v_r) + \frac{1}{r}\frac{\partial}{\partial_x}(r\rho v_x v_r) + \frac{1}{r}\frac{\partial}{\partial r}(r\rho v_r v_r)$$

$$= -\frac{\partial p}{\partial r} + \frac{1}{r}\frac{\partial}{\partial x}\left[r\mu\left(2\frac{\partial v_r}{\partial x} + \frac{\partial v_x}{\partial r}\right)\right] + \frac{1}{r}\frac{\partial}{\partial r}\left[r\mu\frac{\partial v_r}{\partial r} - \frac{2}{3}(\nabla \cdot \vec{v})\right)\left.\right] - 2\mu\frac{v_r}{r^2}$$

$$+ \frac{2}{3}\frac{\mu}{r}(\nabla \cdot \vec{v}) + \rho\frac{v_z^2}{r} + F_r \tag{5}$$

where

$$\nabla \cdot \vec{v} = \frac{\partial v_r}{\partial x} + \frac{\partial v_r}{\partial r} + \frac{v_r}{r} \tag{6}$$

and v_z is the swirl velocity.

The Energy Equation is given by,

$$\frac{\partial}{\partial t}(\rho E) + \nabla \cdot \left(\vec{v}(\rho E + p)\right) = \nabla \cdot \left[k_{eff}\nabla T - \sum_j h_j \vec{J_j} + \left(\bar{\bar{\tau}}_{eff} \cdot \vec{v}\right)\right] + S_h \tag{7}$$

where k_{eff} is the effective conductivity ($k + k_t$), where k_t is the turbulent thermal conductivity, and $\vec{J_j}$ is the diffusion flux of species j. E is given by

$$E = h - \frac{p}{\rho} + \frac{v^2}{2} \tag{8}$$

where sensible enthalpy h is defined for ideal gases as

$$h = \sum_j Y_j h_j \tag{9}$$

where Y_j is the mass fraction of species j and

$$h_j = \int_{T_{ref}}^{T} c_{p,j}\,dT$$

(10)

where T_{ref} is 298.15 K.

The source of energy S_h is the heat of chemical reactions since there are no added volumetric heat sources and is given by

$$S_{h.reaction} = -\sum_{j} \frac{h_j^0}{M_j} \mathcal{R}_j$$

(11)

where h_j^0 is the enthalpy of formation of the species j and $\mathcal{R}_j$ is the volumetric rate of creation of species.

The species transport equation is given by

$$\frac{\partial}{\partial t}(\rho Y_i) + \nabla \cdot (\rho \vec{v} Y_i) = -\nabla \cdot \vec{J_i} + R_i + S_i$$

(12)

where R_i is the net rate of production of species i by chemical reaction and S_i is the rate of creation by addition from the dispersed phase.

In turbulent flows, the mass diffusion is computed in the following form:

$$\vec{J_i} = \left(\rho D_{i,m} + \frac{\mu_t}{Sc_t}\right) \nabla Y_i - D_{T,i} \frac{\nabla T}{T}$$

(13)

where Sc_t is the turbulent Schmidt number ($\frac{\mu_t}{\rho D_t}$ where μ_t is the turbulent viscosity and D_T is the turbulent diffusivity). The default Sc_t 0.7 was used for the cases described in this study.

Two turbulence models used were the Standard and Realizable Viscous Model k-epsilon turbulent models.

The Realizable Viscous Model k-epsilon (2 equation) model is a relatively new model developed and has two main distinctions from the standard k-epsilon model. There is a new formation for turbulent viscosity and a new transport equation for the dissipation rate, epsilon. The transport equation is derived from an exact equation for the transport of the mean-square velocity fluctuation.

The modeled transport equations for k and ε in the Standard and Realizable k – ε model are

$$\frac{\partial}{\partial t}(\rho k) + \nabla \cdot (\rho \vec{v} k) = \nabla \cdot [\left(\mu + \frac{\mu_t}{\sigma_k}\right) \nabla k] + G_k + G_b - \rho \varepsilon - Y_m + S_k$$

(14)

and

$$\frac{\partial}{\partial t}(\rho\varepsilon) + \nabla\cdot(\rho\vec{v}\varepsilon) = \nabla\cdot[\left(\mu+\frac{\mu_t}{\sigma_\varepsilon}\right)\nabla\varepsilon] + \rho C_1 S_\varepsilon - \rho C_2\frac{\varepsilon^2}{k+\sqrt{\nu\varepsilon}} + C_{1\varepsilon}\frac{\varepsilon}{k}C_{3\varepsilon}G$$

(15)

where

$$C_1 = \max\left[0.43, \frac{\eta}{\eta+5}\right]$$

(16)

$$C_{1\varepsilon} = 1.44, \quad C_2 = 1.9,$$

$$\sigma_\varepsilon = 1.2, \ \ \sigma_k = 1.0$$

$$\eta = S\,\frac{k}{\varepsilon}, \ \ S = \sqrt{2S_{ij}S_{ij}}$$

(17), (18)

In these equations, G_k represents the production of turbulence kinetic energy, is modeled using the following equation.

$$G_k = -\rho\overline{u_i'u_j'}\frac{\partial u_j}{\partial u_j}$$

(19)

To evaluate G_k in a manner consistent with the Boussinesq hypothesis,

$$G_k = \mu_t S^2$$

(20)

where S is the modulus of the mean rate-of-strain tensor, defined as

$$S = \sqrt{2}S_{ij}S_{ij}$$

(21)

In the Standard and Realizable k – ε Model the eddy viscosity is computed from

$$\mu_t = \rho C_\mu\frac{k^2}{\varepsilon}$$

(22)

The difference between the Standard and the Realizable k – ε Models is the consideration of C_μ. In the Standard k – ε Model C_μ is a constant and is given by

$$C_\mu = 0.09$$

In the Realizable $k-\varepsilon$ Model C_μ is no longer a constant and is given by

$$C_\mu = \frac{1}{A_0 + A_s \frac{kU^*}{\varepsilon}}$$

(23)

where

$$U^* \equiv \sqrt{S_{ij}S_{ij} + \tilde{\Omega}_{ij}\tilde{\Omega}_{ij}}$$

(24)

and

$$\tilde{\Omega}_{ij} = \Omega_{ij} - \varepsilon_{ij}w_k$$

(25)

$$\Omega_{ij} = \overline{\Omega_{ij}} - \varepsilon_{ij}w_k$$

(26)

where $\overline{\Omega_{ij}}$ is the mean rate-of-rotation tensor viewed in a rotating reference frame with the angular velocity w_k. The model constants $A_0$and $A_s$are given by

$$A_0 = 4.04, A_s = \sqrt{6}\cos\phi$$

where

$$\phi = \frac{1}{3}\cos^{-1}(\sqrt{6}W) \ , \quad W = \frac{S_{ij}S_{jk}S_{ki}}{\tilde{S}^3},$$

(27), (28)

$$\tilde{S} = \sqrt{S_{ij}S_{ij}} \ , \quad S_{ij} = \frac{1}{2}(\frac{\partial u_j}{\partial x_i} + \frac{\partial u_i}{\partial x_j})$$

(29), (30)

For turbulent flows the "modeled" energy equation is given by the following:

$$\frac{\partial}{\partial t}(E) + \frac{\partial}{\partial x_i}[u_i(\rho E + p)] = \frac{\partial}{\partial x_i}(k_{eff}\frac{\partial T}{\partial x_i} + u_i(\tau_{ij})_{eff}) + S_h$$

(31)

where E is the total energy, k_{eff} is the effective thermal conductivity, and $(\tau_{ij})_{eff}$ is the deviatoric stress tensor, defined as

$$(\tau_{ij})_{eff} = \mu_{eff}\left(\frac{\partial u_j}{\partial x_i} + \frac{\partial u_i}{\partial x_j}\right) - \frac{2}{3}\mu_{eff}\frac{\partial u_k}{\partial x_k}\delta_{ij}$$

(32)

The effective thermal conductivity is given by

$$k_{eff} = k + \frac{c_p \mu_t}{Pr_t}$$

(33)

where k is the thermal conductivity and the Prandlt number is set to 0.85, the default value for the turbulent Prandtl number.

The radiative heat transfer is considered using the FLUENT discrete ordinates (DO) radiation model.

Turbulent Combustion is predicted using the Finite rate/Eddy-dissipation model. The Eddy dissipation model assumes reactions are relatively fast and the system is limited solely by turbulent mixing. As this is not always the case, the Eddy dissipation model can be combined with finite-rate chemistry. In this FLUENT model the kinetic rate is calculated as well as the reaction rate prediction from the Eddy dissipation model. The slower reaction rate is used if a turbulent mixing is low, which limits the reaction rate or if turbulence is high, but the kinetic rate is low which will limit the reaction rate.

Where the finite rate is given by the Arrhenius expression

$$\hat{R}_{i,r} = (\Gamma v''_{i,r} - v'_{i,r})(k_{f,r} \prod_{j=1}^{N} [C_{j,r}]^{\eta'_{j,r}} - k_{b,r} \prod_{j=1}^{N} [C_{j,r}]^{v''_{j,r}}$$

(34)

where $v''_{j,r}$ is the product species stoichiometric coefficient and Γ is the net effect of third bodies on reaction rate given by

$$\Gamma = \sum_{j}^{N} \gamma_{j,r} C_j$$

(35)

where $\gamma_{j,r}$ is the third body efficiency of the *j*th species in the *r*th reaction.

The forward rate constant for reaction *r*, $k_{f,r}$ is calculated using the Arrhenious equation

$$k_{f,r} = A_r T^{\beta_r} e^{-E_r/RT}$$

(36)

where A_r represents the pre-exponential factor, $\beta_r$is the temperature exponent, E_r is the activation energy for *r*th reaction, and R is the universal gas constant.

The following reactions were defined for each case defined. Table 1 gives a description of each reaction.

$mv - vol \rightarrow 0.364CO + 0.083H_2 + 0.021N_2 + 0.0071H_2S + 0.636CH_x$……...Reaction 1
$C(s) + 0.5O_2 \rightarrow CO$……………………………………………………………Reaction 2
$C(s) + CO_2 \rightarrow 2CO$……………………………………………………………Reaction 3
$C(s) + H_2O \rightarrow H_2 + CO$…………………………………………………………Reaction 4
$H_2 + 0.5O_2 \rightarrow H_2O$……………………………………………………………Reaction 5
$CO + 0.5O_2 \rightarrow CO_2$……………………………………………………………..Reaction 6
$CO + H_2O \rightarrow CO_2 + H_2$………………………………………………………….Reaction 7
$CO_2 + H_2 \rightarrow CO + H_2O$………………………………………………………….Reaction 8
$CH_x + 0.5O_2 \rightarrow 2H_2 + CO$………………………………………………………Reaction 9
$CH_x + H_2O \rightarrow 3H_2 + CO$………………………………………………………..Reaction 10

CH_x is a hydrocarbon molecule modeled as (tar+C_2+C_3+HCL+CH_4). Kumar et. al. state that since tar is the dominant species in these fragments and the oxygen content in tar is only 5-10% by weight and <5% by mole, assuming (tar+C2+C3+HCL) to be comprised of carbon and hydrogen only is justified [22]. The stoichiometric coefficient x in CH_x, is then derived from coal mass balance. For the Utah Bituminous No. 5 coal used in the following research, x ≈ 1.98 and the volatile composition is given by Reaction 1.

It is assumed that CH_x obeys reaction kinetics similar to common light hydrocarbon molecules like CH_4. Kumar et. al. state that the choice of CH_4 reaction kinetics is justified because the reaction rates with O_2 and H_2O of many hydrocarbons, including CH_4, do not vary greatly from each other [22]. A sensitivity analysis on the kinetic constants of Reactions 9 and 10 was performed by Kumar et. al. It was found that varying the kinetic constants found no significant impact on the final results.

Table 1: Reaction Properties

Reaction	Reaction Type	Rate Exponent (respectively)	Pre-Exponential Factor
Reaction 1	Devolatilization	1	0
Reaction 2	Particle Surface Gasification	0 , 1	0
Reaction 3	Particle Surface Gasification	0 , 1	0
Reaction 4	Particle Surface Gasification	0 , 1	0
Reaction 5	Volumetric Combustion	0.25 , 1.5	6.8000E+15
Reaction 6	Volumetric Combustion	1 , 0.25	2.2387E+12
Reaction 7	Volumetric Gas phase water gas shift	1 , 1	2.7500E+09
Reaction 8	Volumetric Gas phase water gas shift	1 , 1	1.0377E+11
Reaction 9	Volumetric Combustion	0.5 , 1.25	4.4000E+11
Reaction 10	Volumetric Combustion	1 , 1	3.0000E+08

CHAPTER 4

NUMERICAL ANALYSIS

This chapter describes the numerical models created for this study. First the baseline case is described in section 4.1. Section 4.1 also shows the methods used to validate the numerical predictions, including convergence, mesh independence. To gain confidence in the validity of the numeric model, in section 4.2, FLUENT predictions were compared to previous experimental and predictive data.

In order to investigate the effects of steam and oxygen concentrations in the secondary and primary streams a systematic numerical analysis was performed. This involved varying the concentration of steam and oxygen in the secondary and primary inlets, respectively, in regular intervals and interpreting the results. Section 4.3 describes the systematic effects of steam concentrations in the secondary inlets. The systematic effects of oxygen concentration in the primary inlet are described in section 4.4. The results of these numerical analyses are discussed in Chapter 5.

Cases deemed optimal were those with increased CO and H_2 production, decreased CO_2.

4.1 Basic Case Setup

This section describes the baseline case setup investigated in this study. This case is referred to as "Case 1." The reactor geometry is described in section 4.1.1 Section 4.1.2 states the boundary conditions, and section 4.1.3 describes the coal injection properties.

4.1.1 Gasifier Geometry

The gasifier considered in this study was based off the BYU laboratory gasifier mentioned in section 3.1. The original schematics for the BYU gasifier are shown in Fig 4.

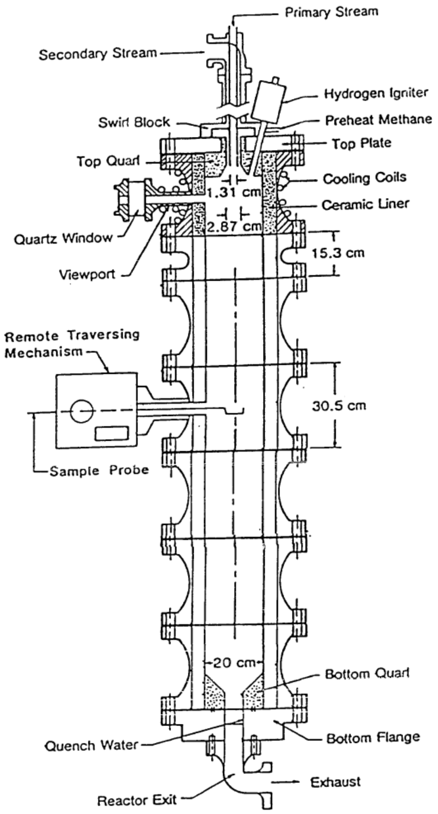

Figure 4: Schematic of Brigham Young University experimental gasifier [13]

Fig. 5. shows the geometry used in this research.

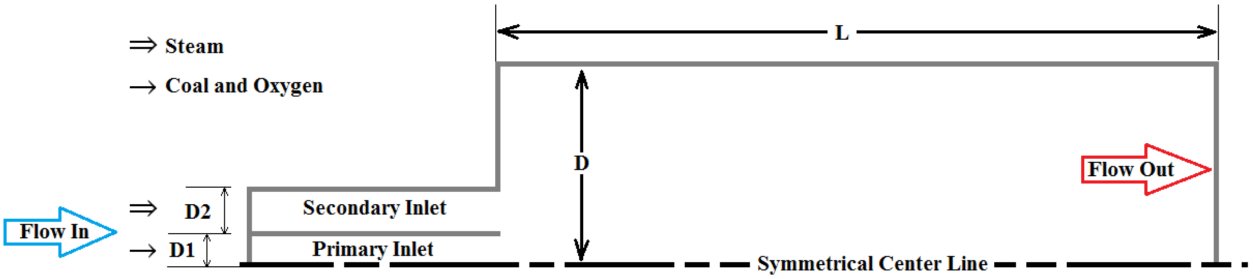

Figure 5: Symmetric reactor geometry

where

D = 0.2 m
D1 = 0.0131 m
D2 = 0.0287 m
L = 2.0 m
L2 = 0.1 m

4.1.2 Boundary Conditions

Table 3 describes the boundary conditions defined in FLUENT.

Table 2: Case 1 Boundary Conditions

Zone	Mass Flow Specification Method	Species	Mass Flow Rate (kg/sec)	Temperature (K)	Turbulence Specification Method	Turbulence Intensity (%)	Hydraulic Diameter (m)
Primary Inlet	Mass Flow Rate	Oxygen	0.00729	367	Intensity and Hydraulic Diameter	10	0.0131
Secondary Inlet	Mass Flow Rate	Steam	0.00184	450	Intensity and Hydraulic Diameter	10	0.0287
Outlet	N/A	N/A	N/A	N/A	Intensity and Hydraulic Diameter	10	0.2000

4.1.3 Coal Properties

The coal used in the present study was Utah bituminous No. 5. The Proximate and Elemental Analyses are given in Table 3.

Table 3: Proximate and Elemental Analysis of Test Coal (Weight Percent)

Proximate (wet Basis)	
Moisture	2.4
Ash	8.3
Volatiles	45.6
Fixed Carbon	43.7
Higher Heating Value (MJ/kg as received)	29.8
Elemental (dry basis)	
Ash	8.5
H	6
C	71
N	1.3
S	0.5
O	12.7
Mass Mean Particle Diameter (microns)	41.4

4.1.4 Injection Properties

Coal particles where injected into the primary inlet. Five different injections were defined. Each injection has the same properties except the injection diameters were varied. A Surface Injection type was chosen for each injection. Combusting Particle type was selected for the injections and the diameter distribution was set to uniform. The injection point properties for each of the five injections are shown in Table 4.

Table 4: Injection Point Properties

X-Velocity (m/s)	50
Y-Velocity (m/s)	0
Coal Particle Diameter 0(µm)	3.0
Coal Particle Diameter 1(µm)	20.0
Coal Particle Diameter 2(µm)	28.0
Coal Particle Diameter 3(µm)	50.0
Coal Particle Diameter 4(µm)	80.0
Temperature (K)	367
Total Flow Rate (kg/s)	0.001327

4.2 Validation of Method

Section 4.2 demonstrations the methods used to validate the mesh and various CFD sub models used to describe this case. In order to verify convergence section 4.2.1 shows how convergence was validated for each case. Section 4.2.2 demonstrates how the mesh was verified by showing mesh independence. The model was then validated using data from the FLUENT case predictions compared to experimental data from Soelburgs 1984 study, Browns 1985 study, as well as PCGC-2 predictions from Browns 1985 research.

4.2.1 Proof of Convergence

As each case was processed, scaled residuals were monitored until they stabilized. To ensure convergence the static temperature and velocities at the axisymmetric centerline were plotted at three different iterations. Each temperature and velocity profile comparison was plotted in 10,000 iteration increments. Convergence for the baseline case Case 1 is shown in Figures 6 and 7. Convergence for each case was validated using the same method. For reference, the symmetrical contours for “Iteration 3” are shown at the bottom of each figure.

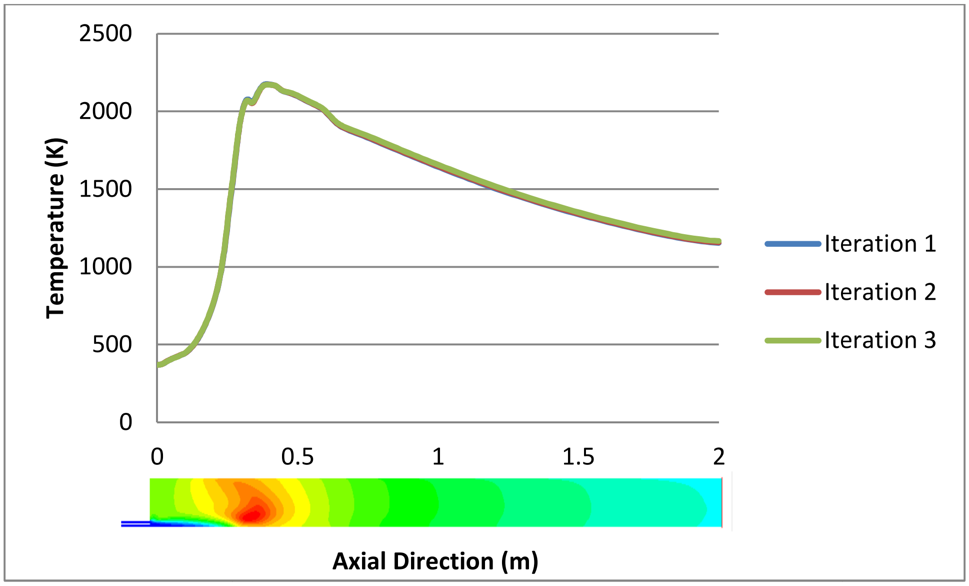

Figure 6: Proof of Convergence; Temperature profile comparison at three separate iterations in 10,000 iteration intervals

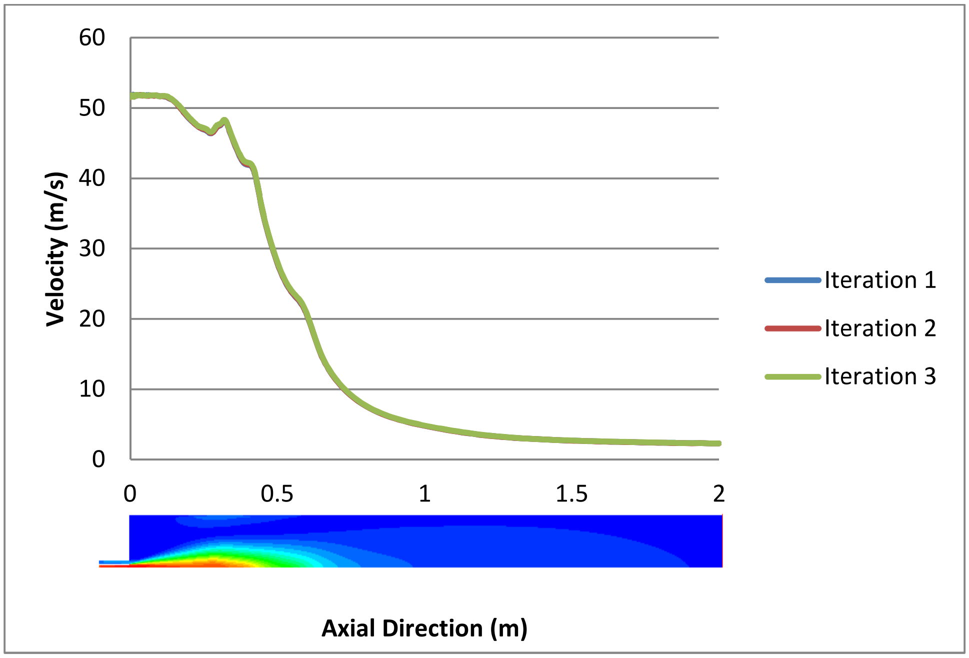

Figure 7: Proof of Convergence; Velocity profile comparison at three separate iterations in 10,000 iteration intervals

4.2.2 Mesh Independence

Mesh independence was verified by doubling the mesh in the x and y directions, thus quadrupling the refinement i.e. number of cells. Fig. 8 shows what the original mesh construction looked like. Fig 9 shows the refined mesh called “Doubled.” The mesh sizes are given in Table 5.

Table 5: Mesh sizes for original and refined meshes

Case	Level	Cells	Faces	Nodes	Partitions	Cell Zones	Face Zones
Case 1	0	13752	27778	14027	1	1	7
Doubled	0	55008	110564	55557	1	1	7

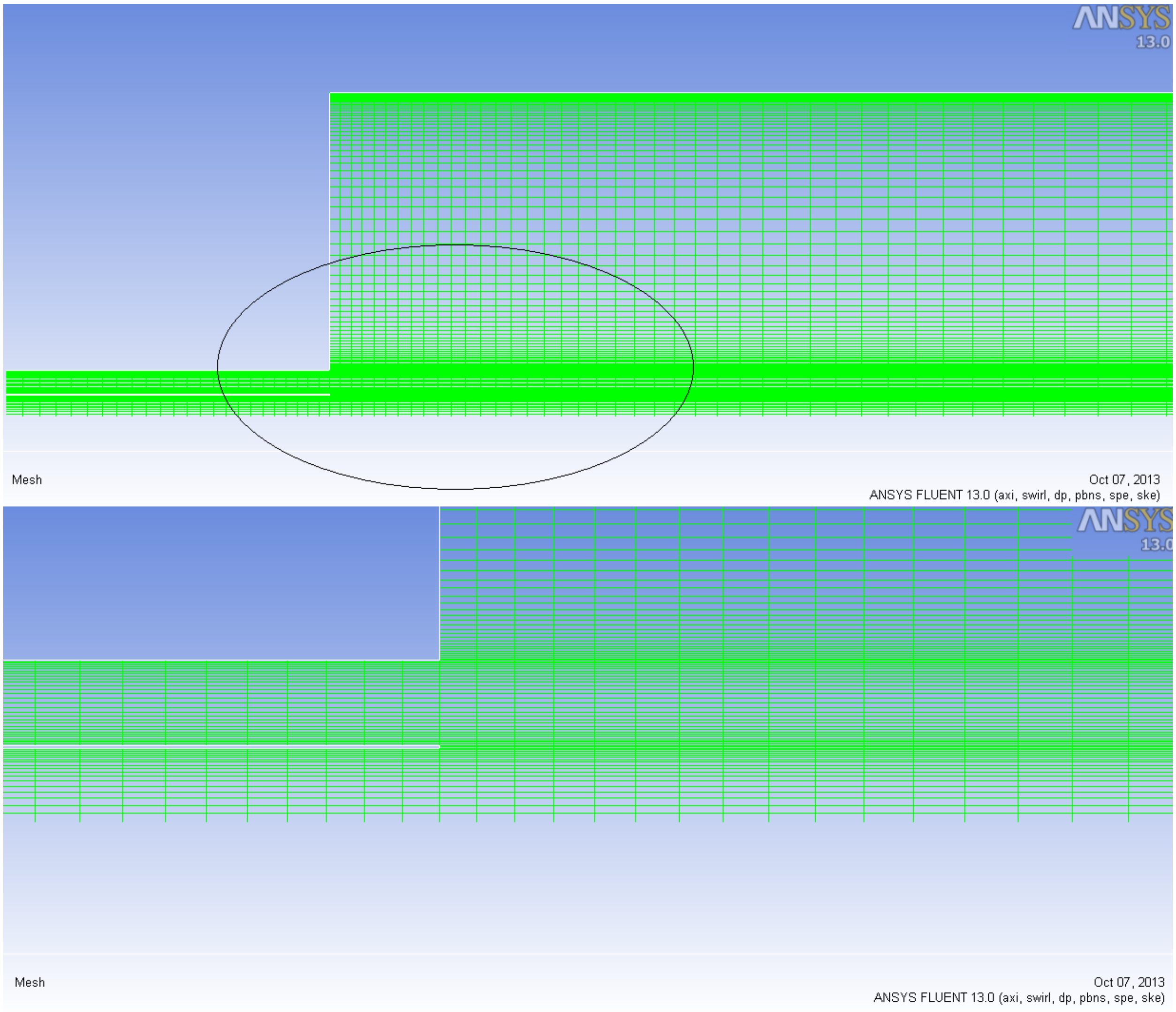

Figure 8: Mesh before refinement. Bottom picture displays the detail inside of the ellipse.

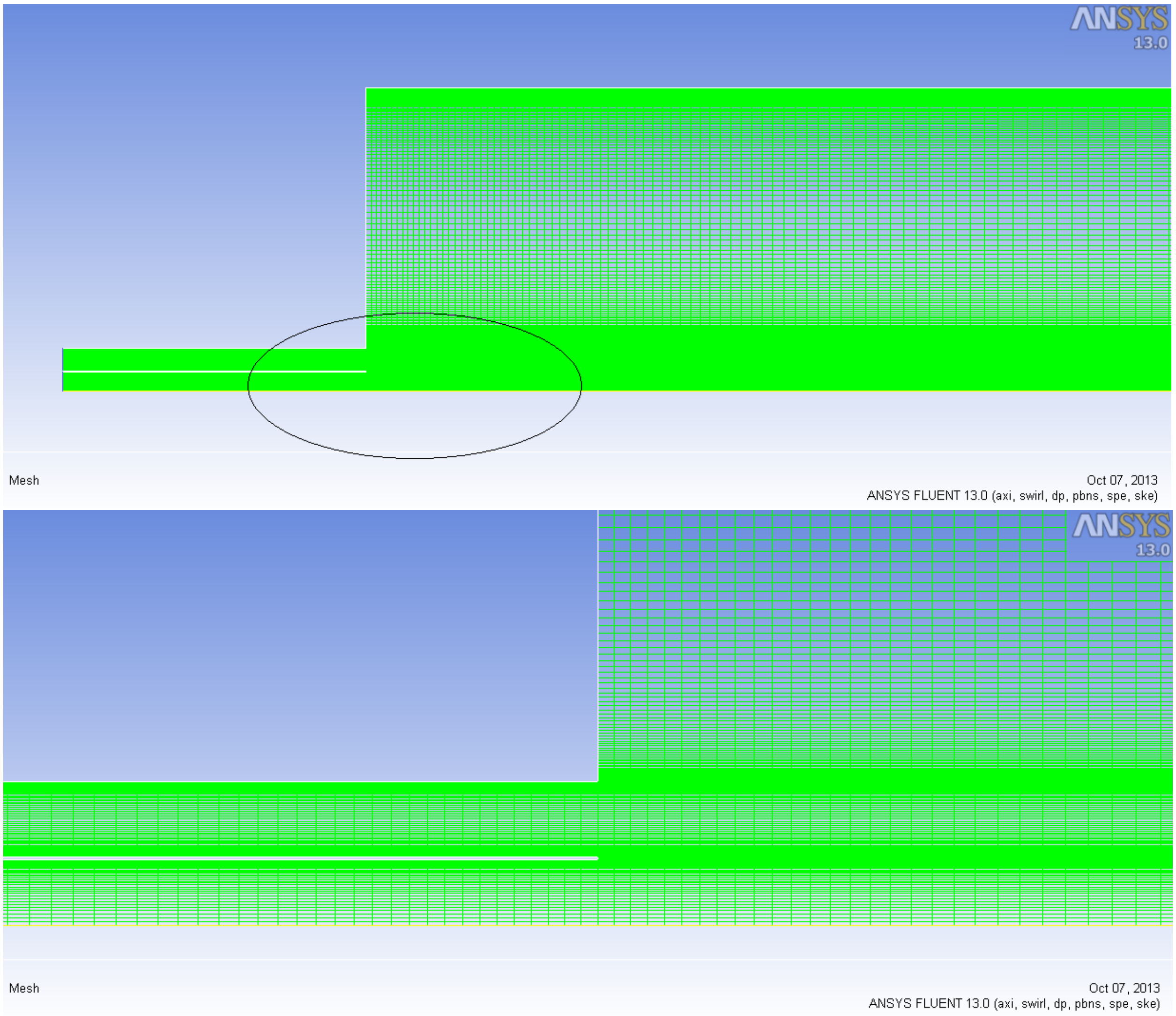

Figure 9: Mesh after Refinement (Doubled mesh). Bottom picture displays the detail inside of the ellipse

The velocity and temperature profiles for the original and refined mesh are shown in Figures 10 and 11. For reference, the symmetrical contours of each species from the original case “Case 1” predictions are shown at the bottom of each figure in this section.

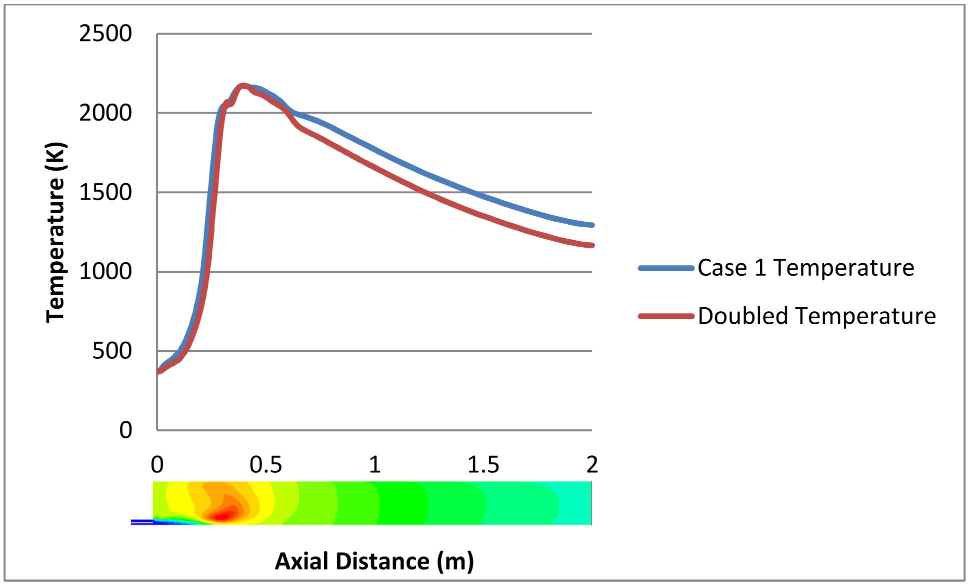

Figure 10: Validation of mesh adaption; Comparison of original mesh "BYU2D" and the refined mesh "Doubled" temperature (K) along axisymmetric centerline

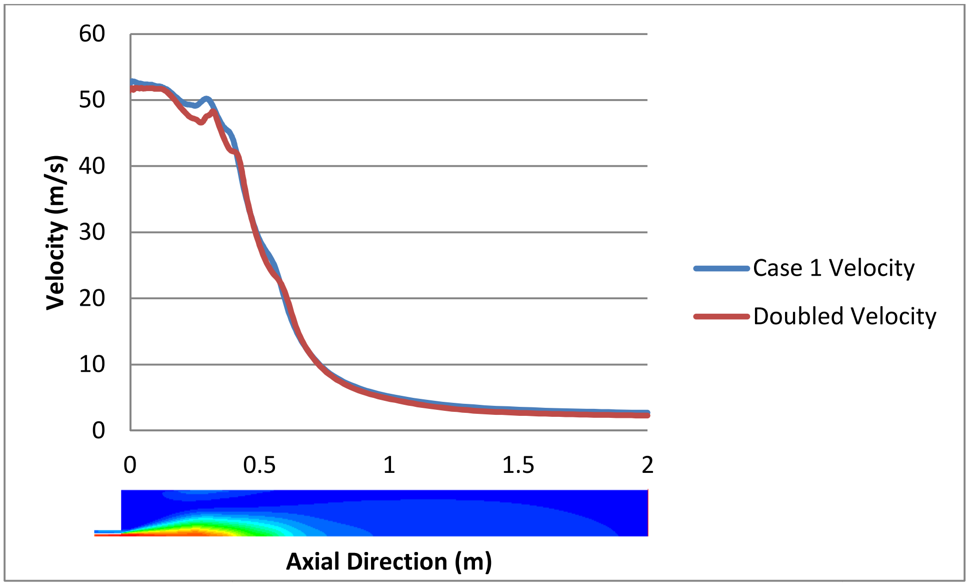

Figure 11: Validation of mesh adaption; Comparison of original mesh "BYU2D" and refined mesh "Doubled" velocities along axisymmetric centerline

The temperature and velocity profiles show relatively good agreement with an average error of 3.2% and 1.1 % respectively. Therefore the results are considered to be mesh independent.

4.2.3 Model Validation

In order to gain confidence in the validity of the FLUENT predictions, the baseline case “Case 1” which was modeled using the standard and realizable $k-\varepsilon$ turbulence model was compared with previous experiments and predictions. These include Browns 1985 experimental and PCGC-2 predictive data as well as Solberg’s 1982 predictions. For reference, the symmetrical contours of each species from the standard k-e turbulence model predictions are shown at the bottom of each figure. For reference the contours of Case 1 are displayed in Appendix A, and a comparison of the Case 1 FLUENT predictions and Brown’s 1985 experimental data is given in Appendix B.

Gas Concentrations Considered in Wet Mole Percentage

i. H_2
ii. H_2O
iii. CO
iv. CO_2
v. O_2

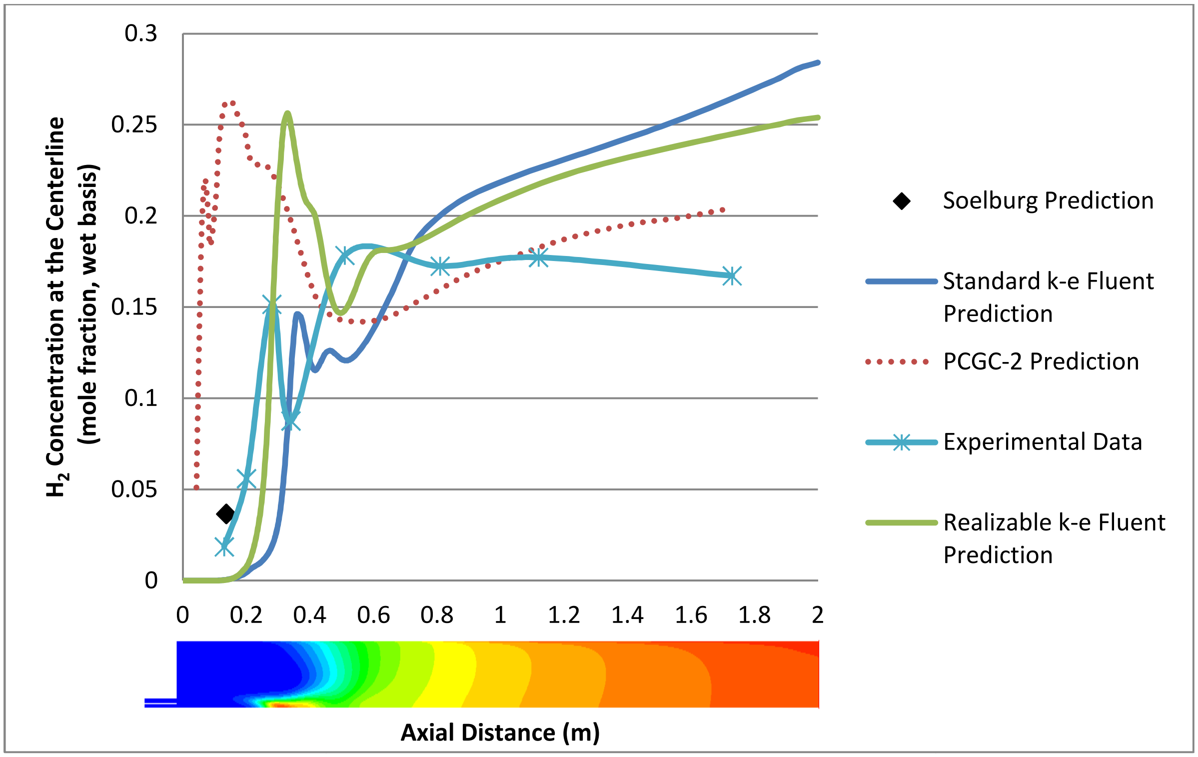

Figure 12: Comparison of Soelburg, Fluent, and PCGC-2 Predictions and Experimental Data at the Reactor Centerline for Concentration

The mole fraction PCGC-2 prediction was subject to an error of up to 100% in the forward region[13]. The Standard Fluent Prediction shows much better agreement in the forward region than the PCGC-2 prediction and the Realizable Fluent Prediction.

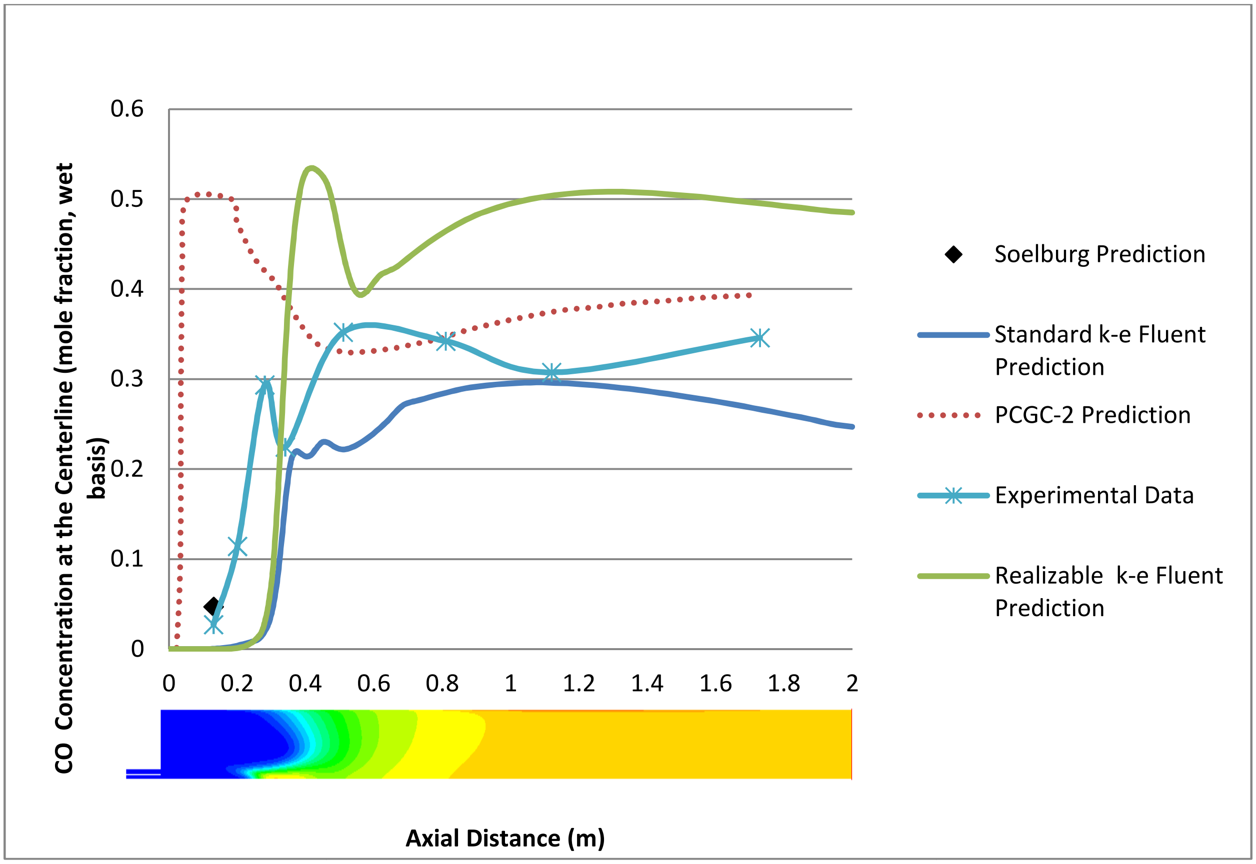

Figure 13: Comparison of Soelburg, Fluent, and PCGC-2 Predictions and Experimental Data at the Reactor Centerline for Concentration

Production of was predicted by PCGC-2 to start nearer the reactor inlet than was observed experimentally by Brown. Peak values 50 percent higher than the experimental values were observed [13].

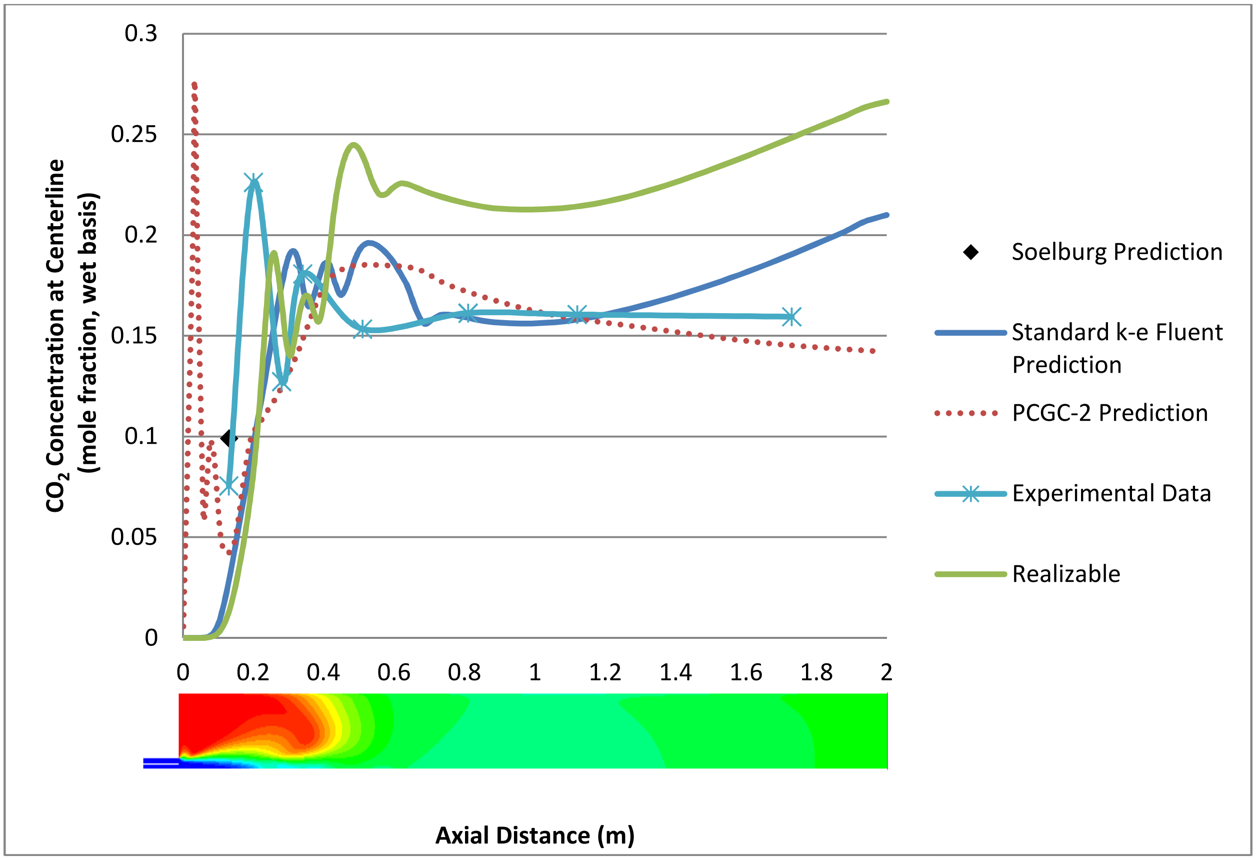

Figure 14: Comparison of Soelburg, Fluent, and PCGC-2 Predictions and Experimental Data at the Reactor Centerline for Concentration

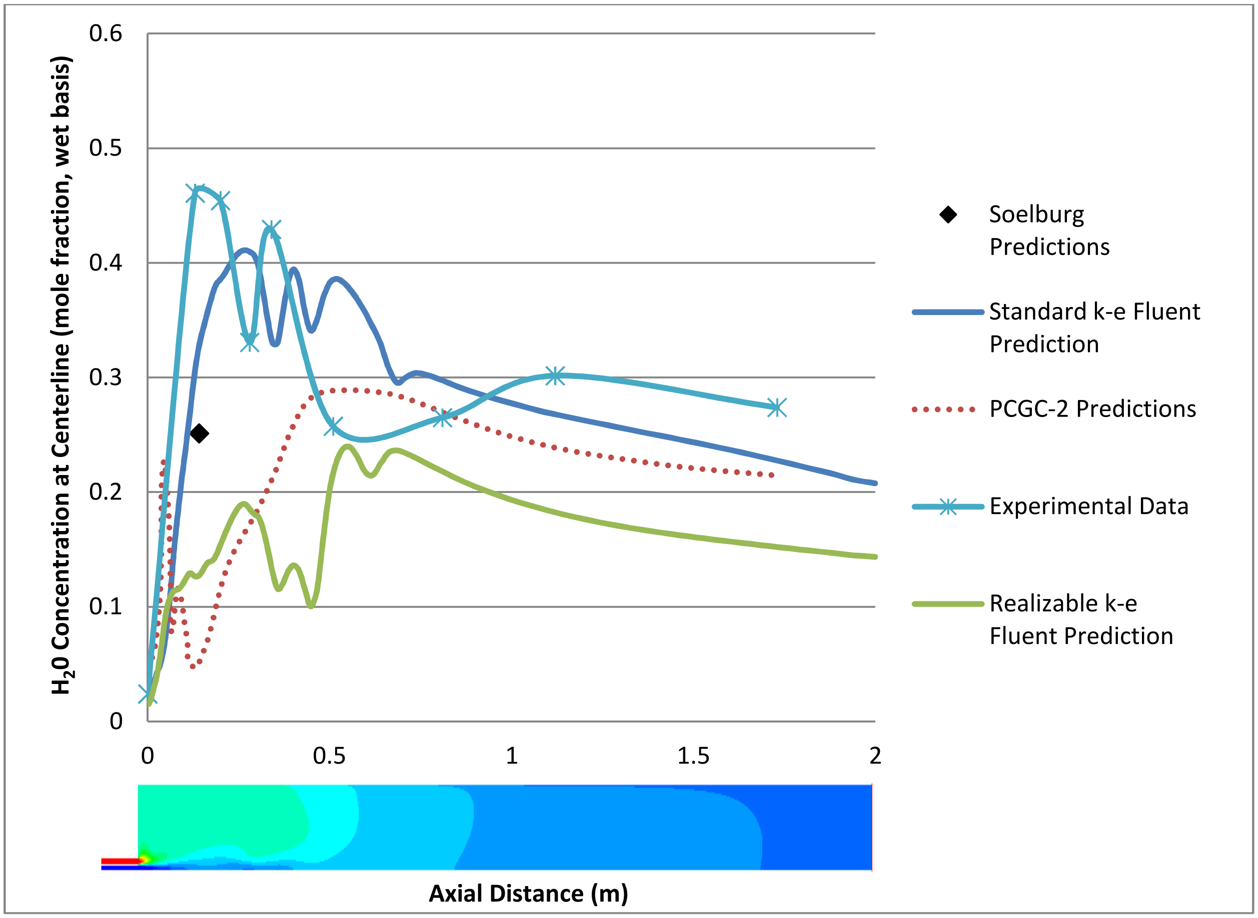

Figure 15: Comparison of Soelburg, FLUENT, and PCGC-2 Predictions and Experimental Data at the Reactor Centerline for Concentration

The mole fraction PCGC-2 prediction was subject to an error of 14% [13]. Fig. 15 shows the Standard Fluent Prediction for the mole fraction, and also shows much better agreement with the experimental data than the PCGC-2 prediction and the Realizable Fluent Prediction.

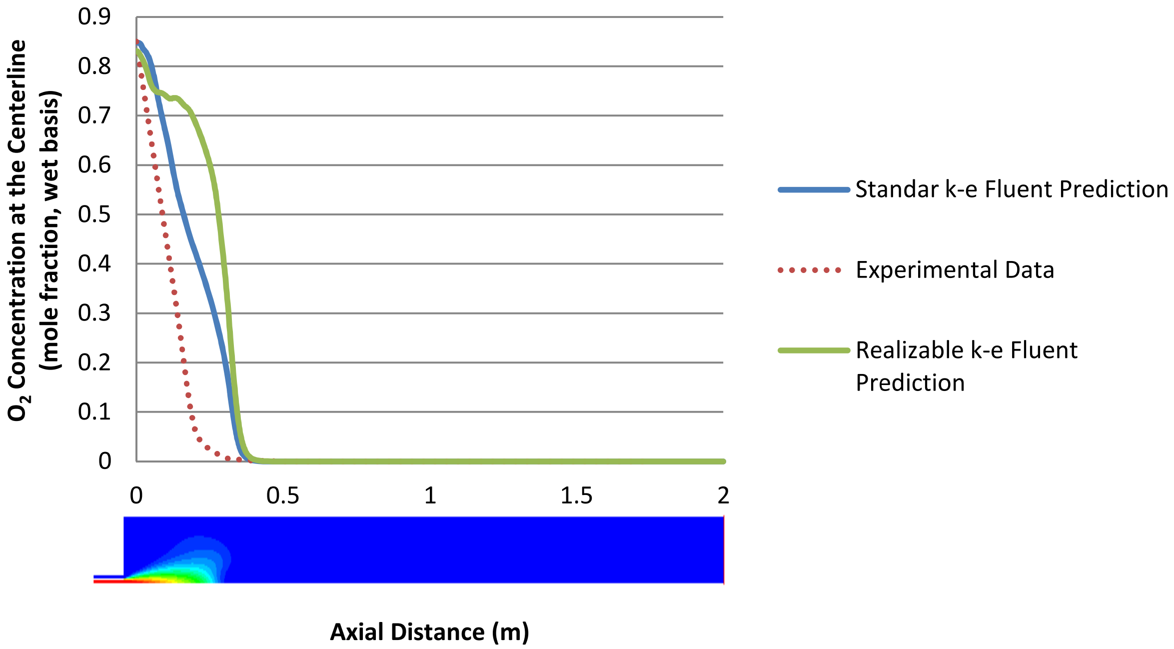

Figure 16: Comparison of Soelburg, FLUENT, and PCGC-2 Predictions and Experimental Data at the Reactor Centerline for Concentration.

It was reported in Brown's study that coal weight loss to the gas phase was over 65% (dry basis) by the 0.40 meter position. This weight loss accounted for over 150% of the proximate volatile mater content [13]. This initial rapid weight loss was attributed to the devolatilization of the coal, which was found to be completed by the 0.50-0.60 meter axial position. Less rapid weight loss down steam was attributed to the heterogeneous reactions thought to begin near the 0.40 meter axial position.

Brown states the discrepancy of the PCGC-2 predictions in the forward region of the gasifier suggests that the devolatilization was modeled incorrectly. The model assumed that each element in the coal devolatizes at the same rate [13]. Brown states that since Utah No. 5 coal has a relatively high carbon and hydrogen concentration and relatively low oxygen content, this generalization in devolatilization would tend to increase the and concentrations due to devolatilization. The Standard Fluent model showed good agreement to experimental data in the forward region of the gasifier from the inlet up to between 0.40 and 0.50 meters. This suggests the devolatilization was modeled sufficiently. After the 0.40 meter position the experimental data and FLUENT predictive data diverge. The error in the aft region suggests could be attributed the modeling of the volumetric heterogeneous reactions.

4.3 Effects of Steam in Secondary Inlet

This section investigates the effects of steam concentration in the secondary inlet. This was done by varying the concentration of steam input in the secondary inlet by ten percent increments from 50 to 100 percent of the base case, “Case 1,” described in section 4.1. The operating conditions for each case are given by Table 6. For reference, the symmetrical contours of each species from the original case “Case 1” predictions are shown at the bottom of each figure in this section.

Table 6: Species Concentrations Flowing Into Secondary Inlet

Case	Steam in Secondary Inlet	Mass Fraction H_2O	Mass Fraction N_2
Case 1	100% Steam	1	0
Case S-50	50% Steam	0.5	0.5
Case S-60	60% Steam	0.6	0.4
Case S-70	70% Steam	0.7	0.3
Case S-80	80% Steam	0.8	0.2
Case S-90	90% Steam	0.9	0.1

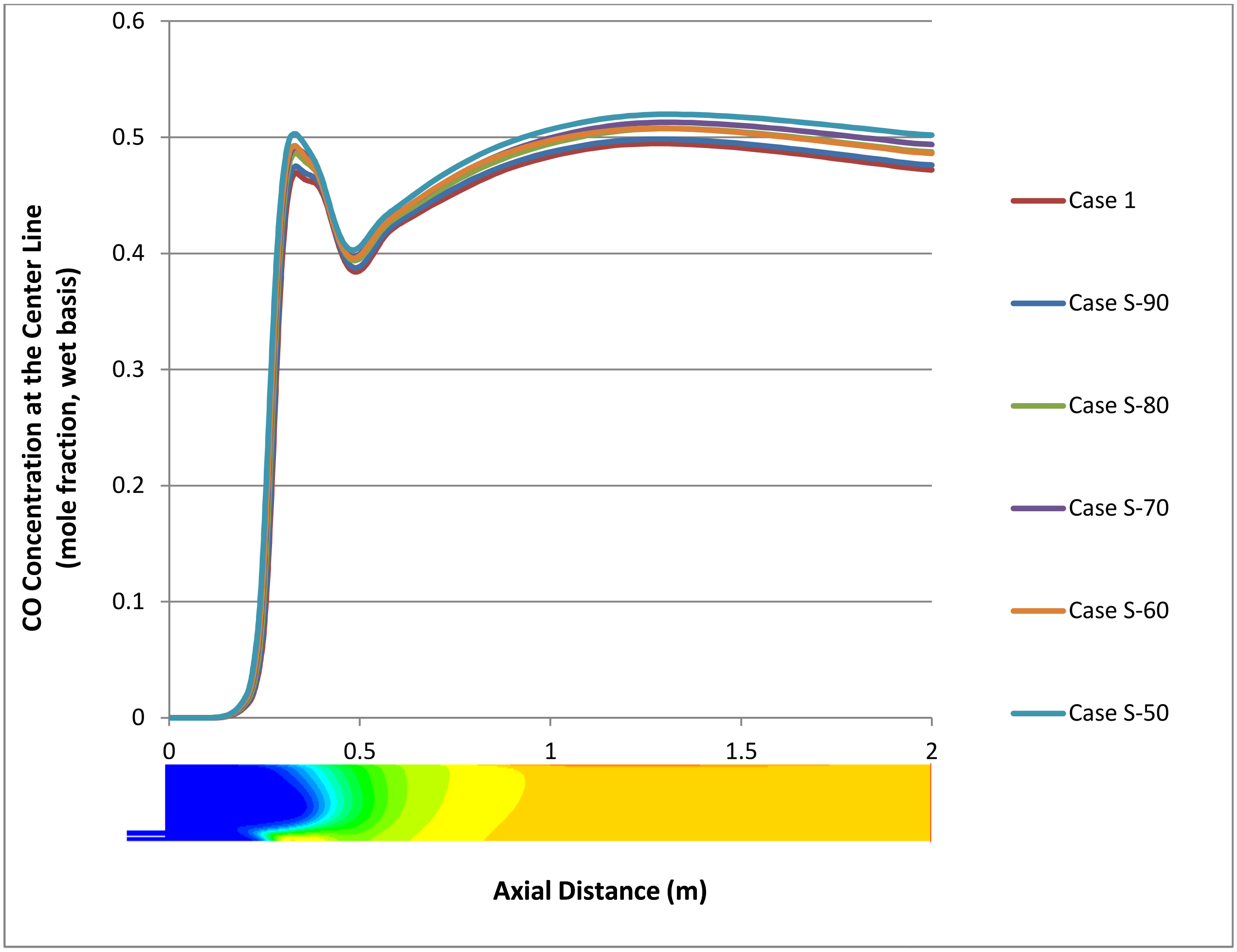

Figure 17: Comparison of concentrations from FLUENT prediction at the reactor centerline

Higher steam throughput in the secondary inlet generaly decreases production while increasing the concentrations. This is true for every case except Case S-70.

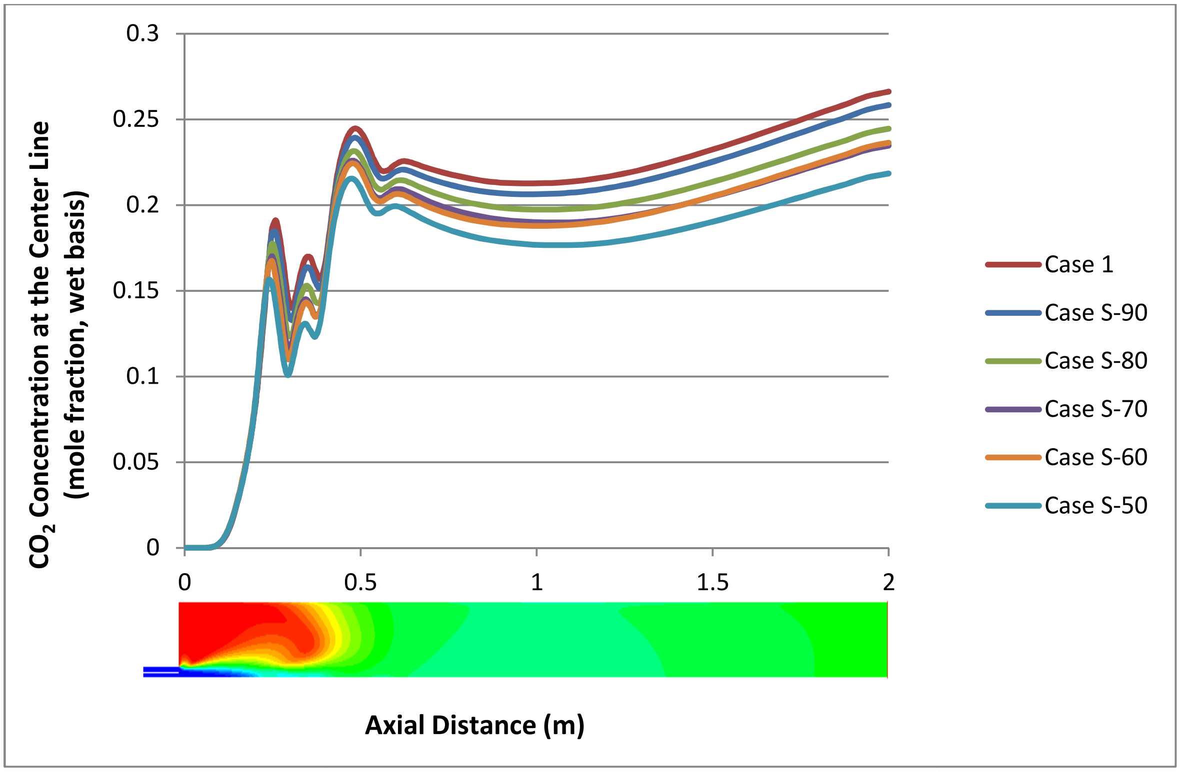

Figure 18: Comparison of concentrations from FLUENT prediction at the reactor centerline

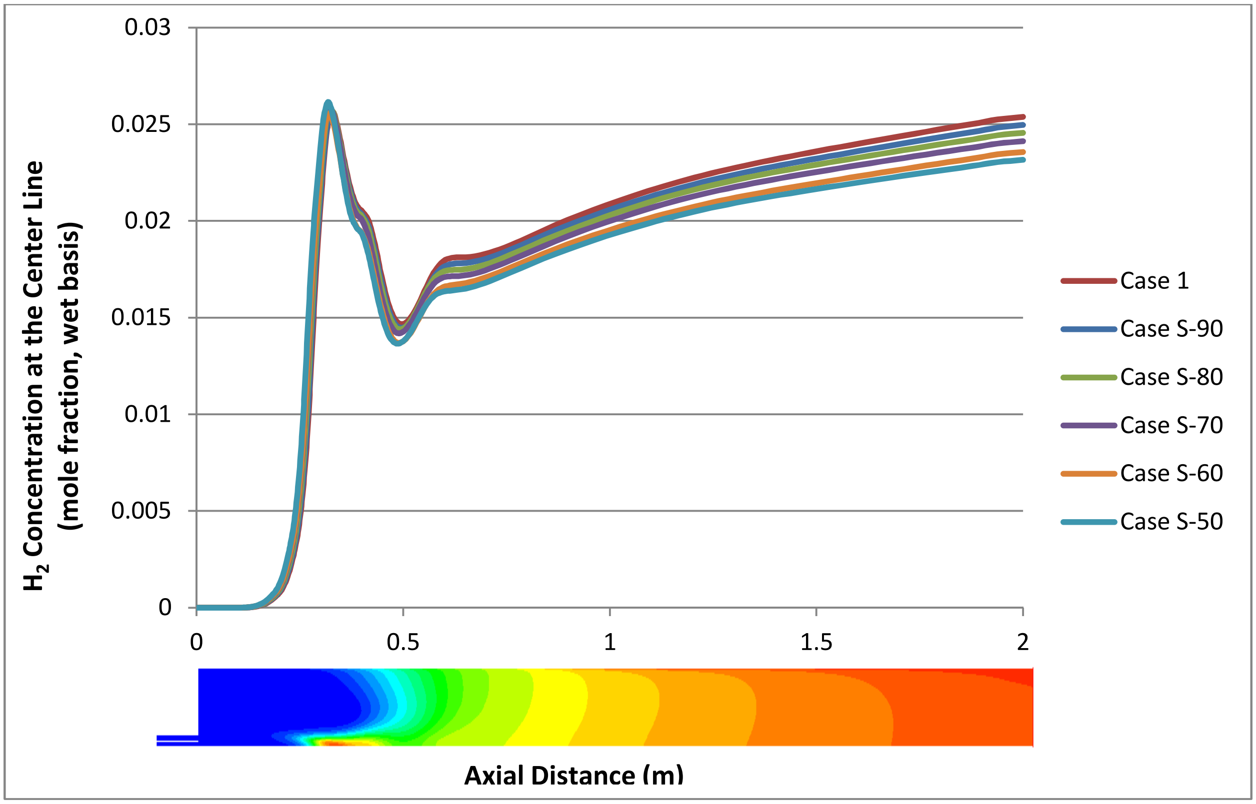

Figure 19: Comparison of concentrations from FLUENT prediction at the reactor centerline

Fig. 20 shows a clear relation of steam concentration on hydrogen production. The function of steam inputs effect on exit hydrogen concentration is shown in Fig. 21 and follows a linear path. The function can be given by the equation

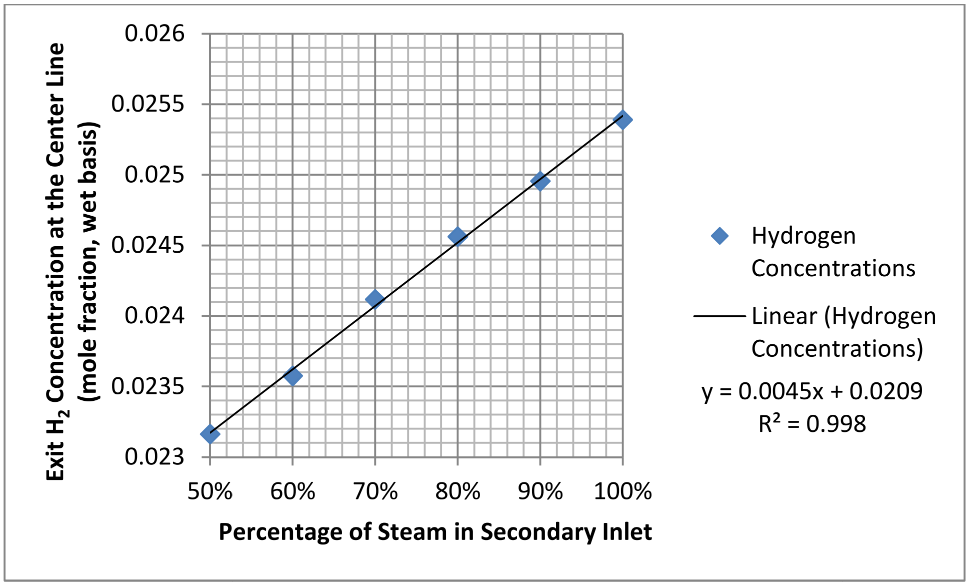

Figure 20: Exit Hydrogen Concentrations from 50 to 100% Steam in Secondary Stream

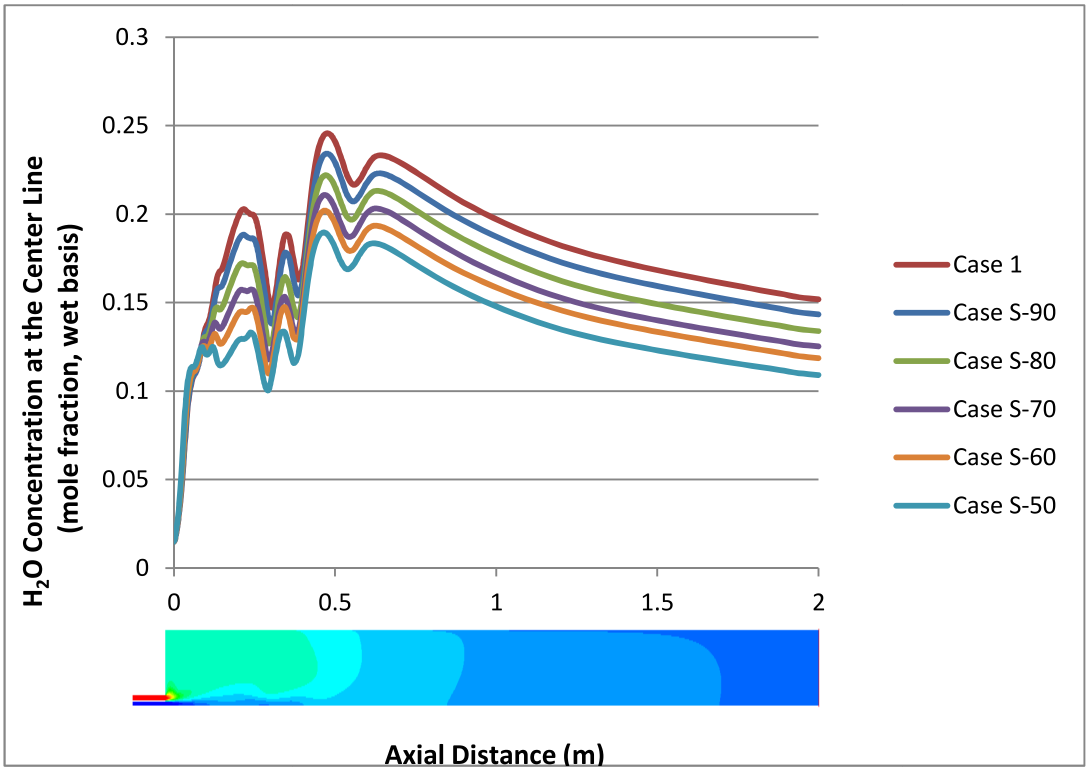

Figure 21: Comparison of concentrations from FLUENT prediction at the reactor centerline

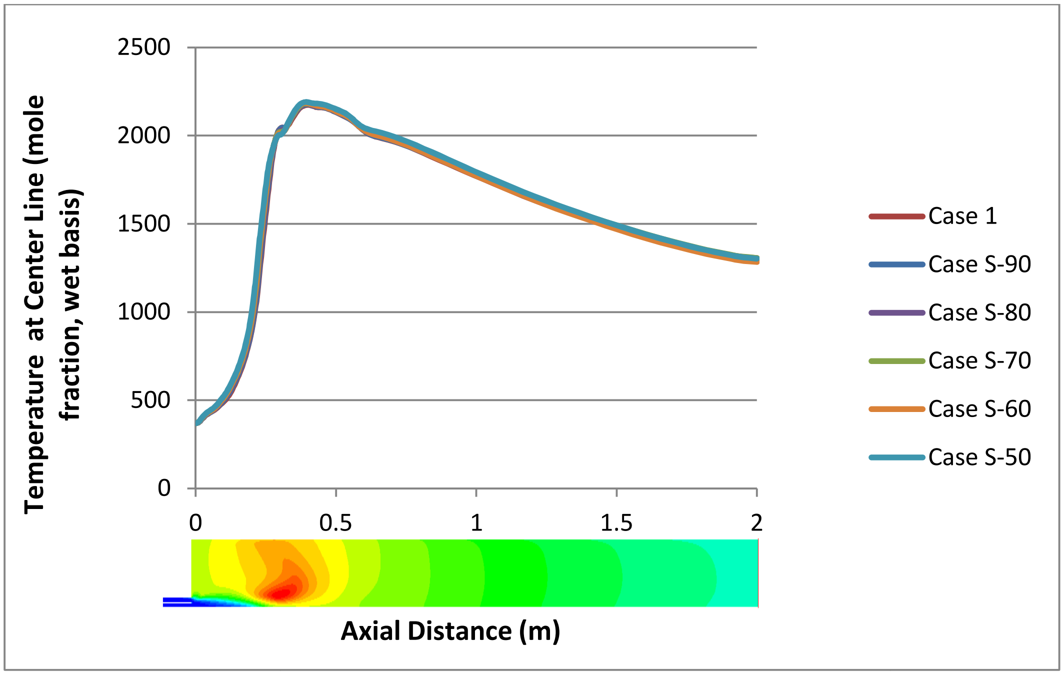

Figure 22: Comparison of Static Temperature (K) from FLUENT prediction at the reactor centerline

Fig 22 shows FLUENT predicts steam concentration in the secondary inlet has no significant effect on reactor temperatures.

4.4 Effects of Oxygen in Primary Inlet

This section investigates the effects of oxygen concentrations in the primary inlet. This was done by varying the concentration of oxygen input in the primary inlet from 60 to 115 percent of the base case, “Case 1,” described in section 4.1. The operating conditions for each case are given by Table 7.

Table 7: Species Concentrations Flowing Into Primary Inlet

Case	Oxygen in Primary Inlet	Mass Fraction	Mass Fraction	Mass Fraction
Case 1	Original %	0.832669	0.0132365	0.154049
Case O-50	50%	0.429571	0.0132365	0.557192
Case O-60	60%	0.499601	0.0132365	0.487161
Case O-70	70%	0.582868	0.0132365	0.403894
Case O-80	80%	0.666135	0.0132365	0.320627
Case O-90	90%	0.749402	0.0132365	0.237360
Case O-110	110%	0.915936	0.0132365	0.070827
Case O-115	115%	0.957569	0.0132365	0.029193

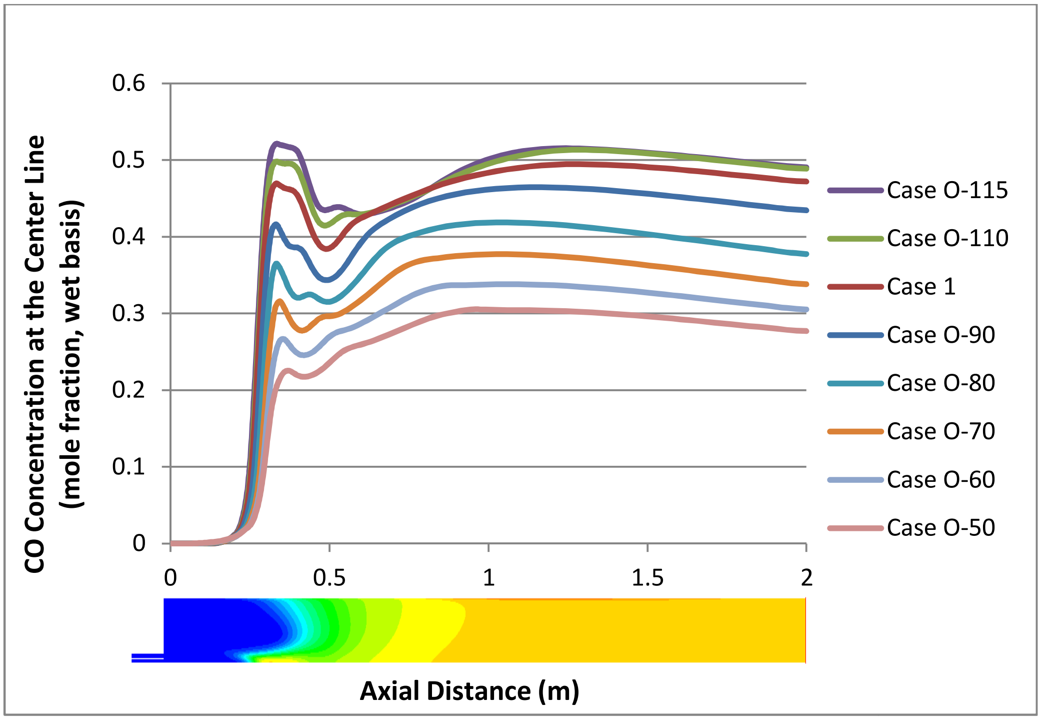

Figure 23: Comparison of concentrations from FLUENT prediction at the reactor centerline

Fig. 23 shows as the concentration in the primary stream is decreased the *CO* concentration decreases.

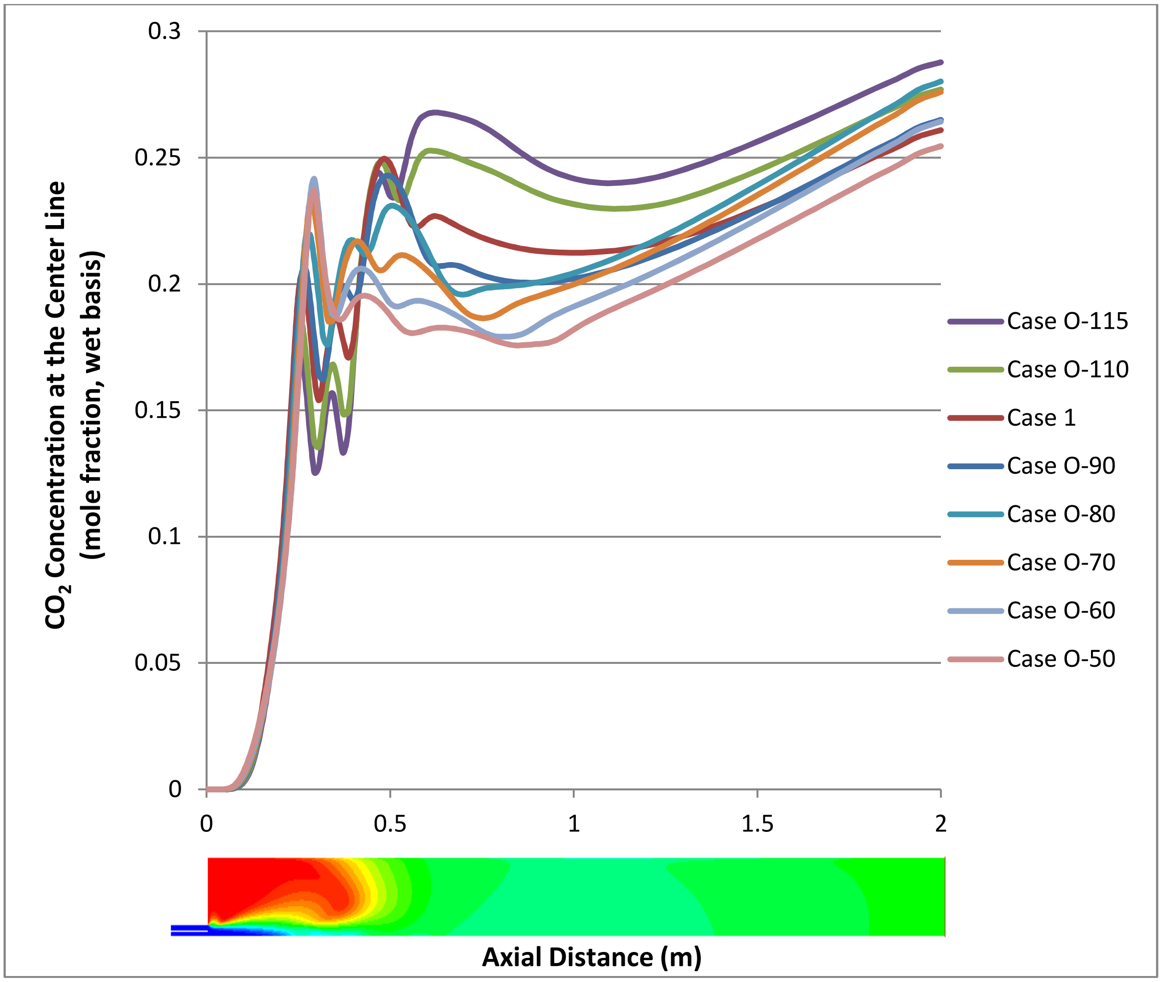

Figure 24: Comparison of concentrations from FLUENT prediction at the reactor centerline

As the as the oxygen content in the primary stream is increased the carbondioxide concentration increases.

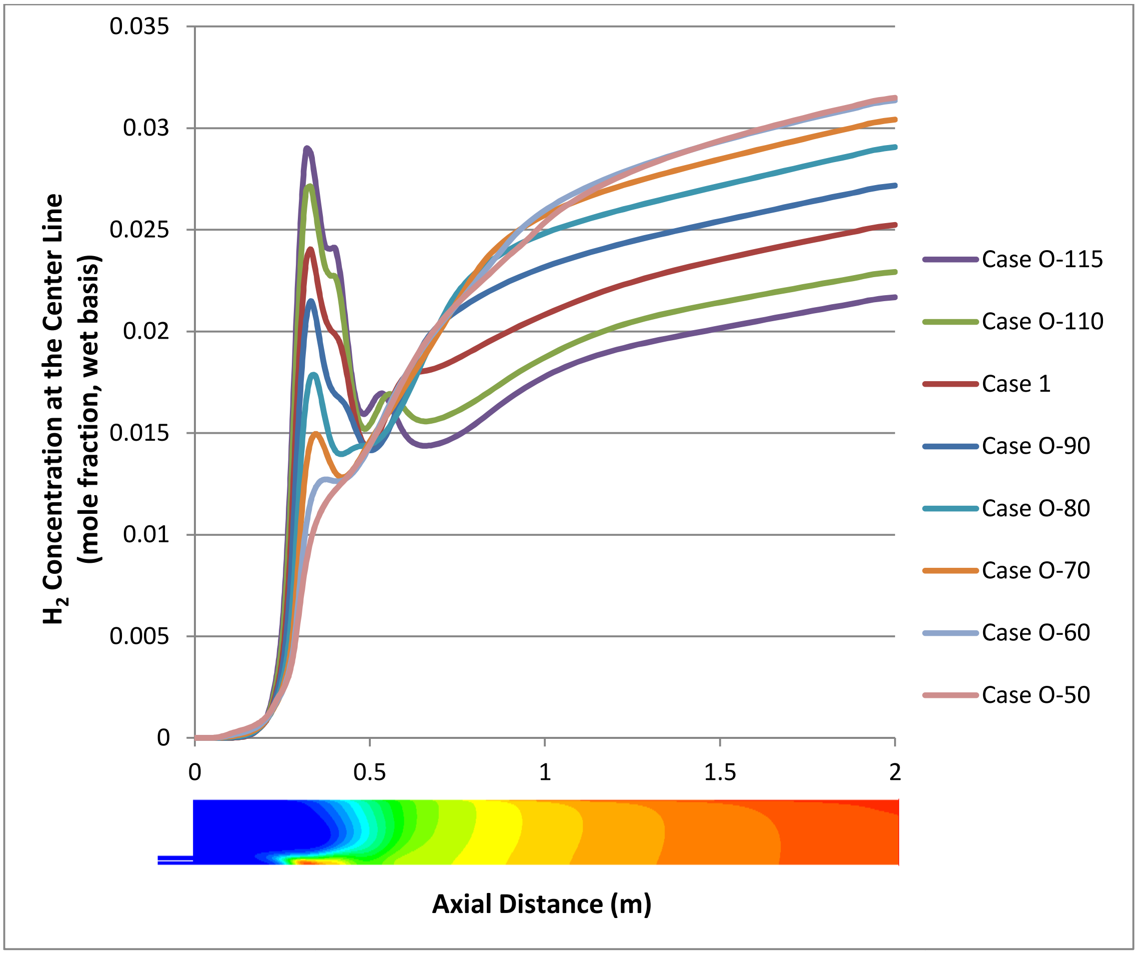

Figure 25: Comparison of concentrations from FLUENT prediction at the reactor centerline

Increasing the oxygen content in the primary stream decreases the concentrations. The exit hydrogen concentration as a function of oxygen concentration is shown in Fig. 26 and can be describe by the second order polynomial equation

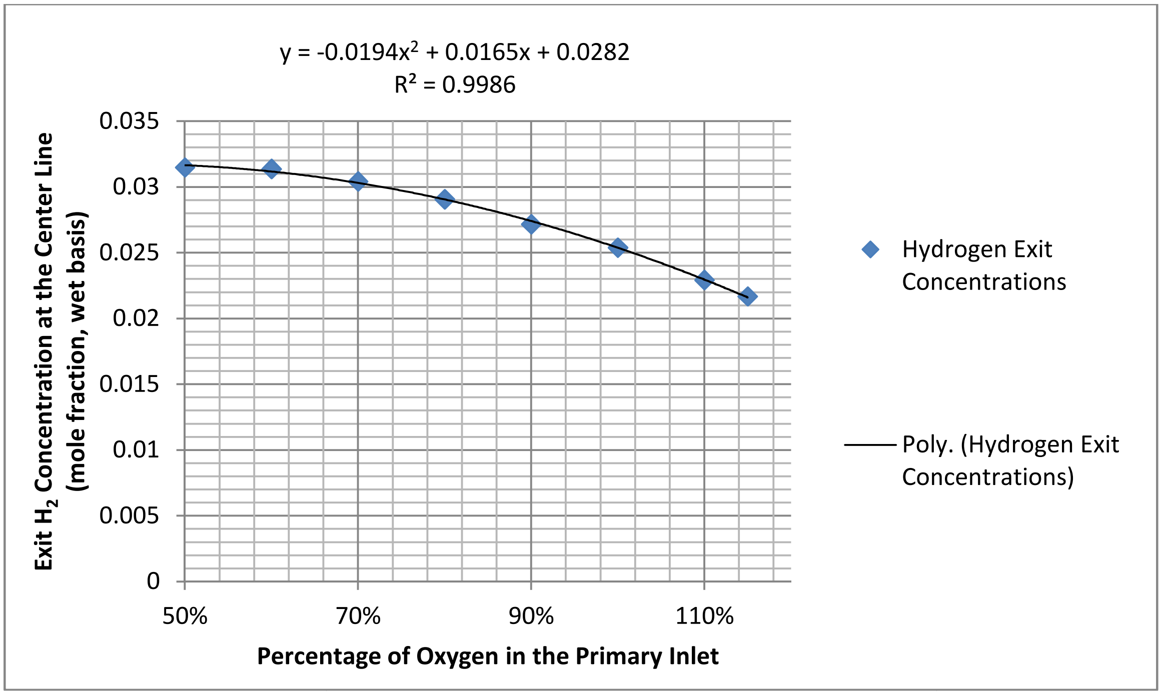

Figure 26: Hydrogen Exit Concentrations from 50 to 115 % Oxygen flowing into the primary stream

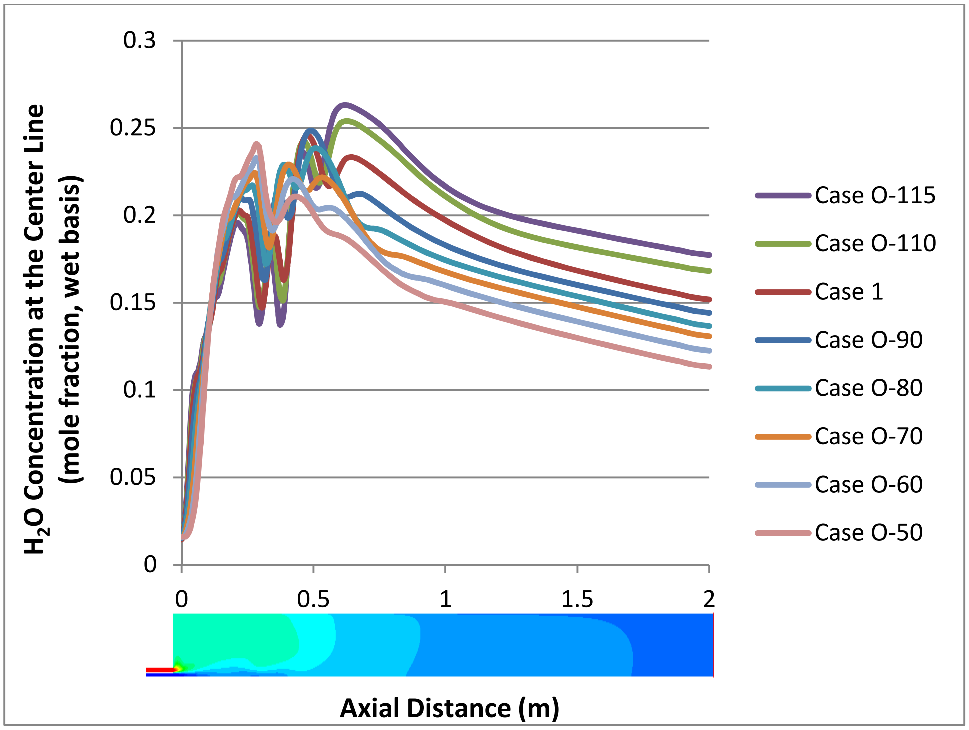

Figure 27: Comparison of concentrations from FLUENT prediction at the reactor centerline

concentrations decrease with decreasing primary inlet oxygen throughputs.

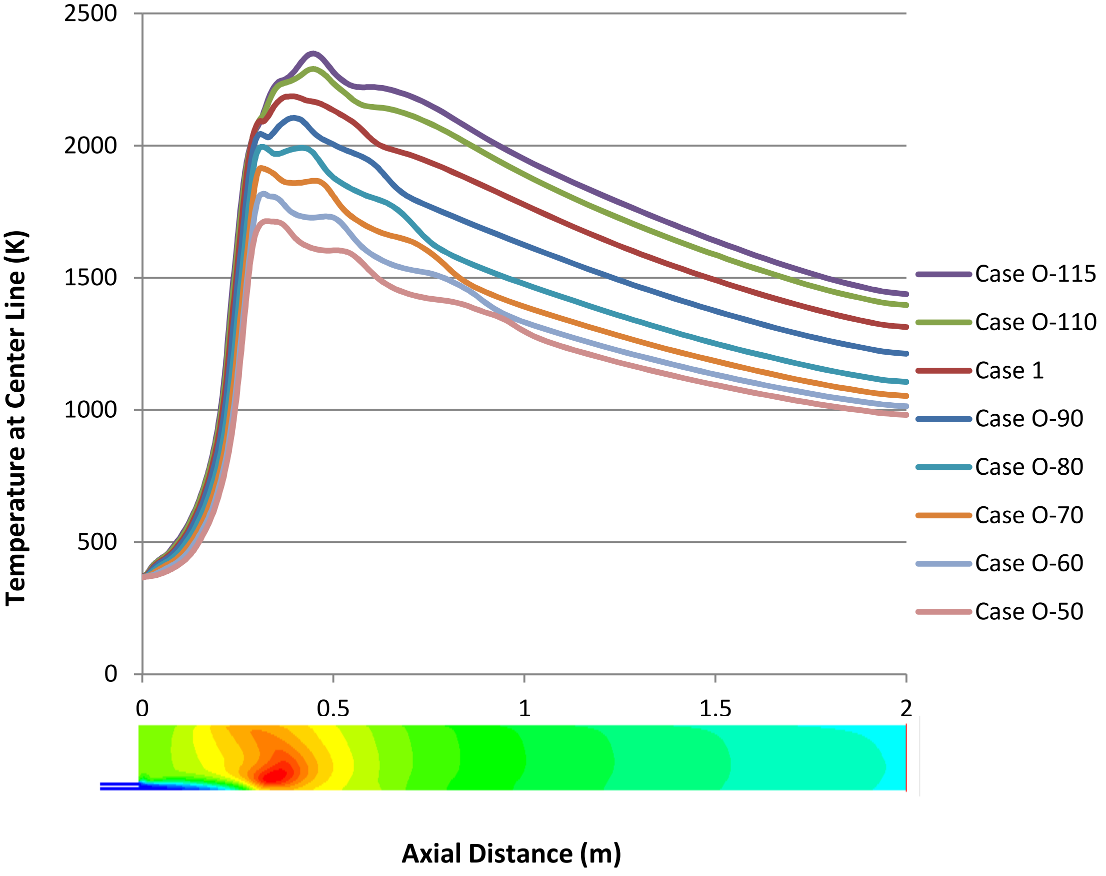

Figure 28: Comparison of Static Temperature (K) from FLUENT prediction at the reactor centerline

Temperature in the gasifier increase as oxygen concentration increases.

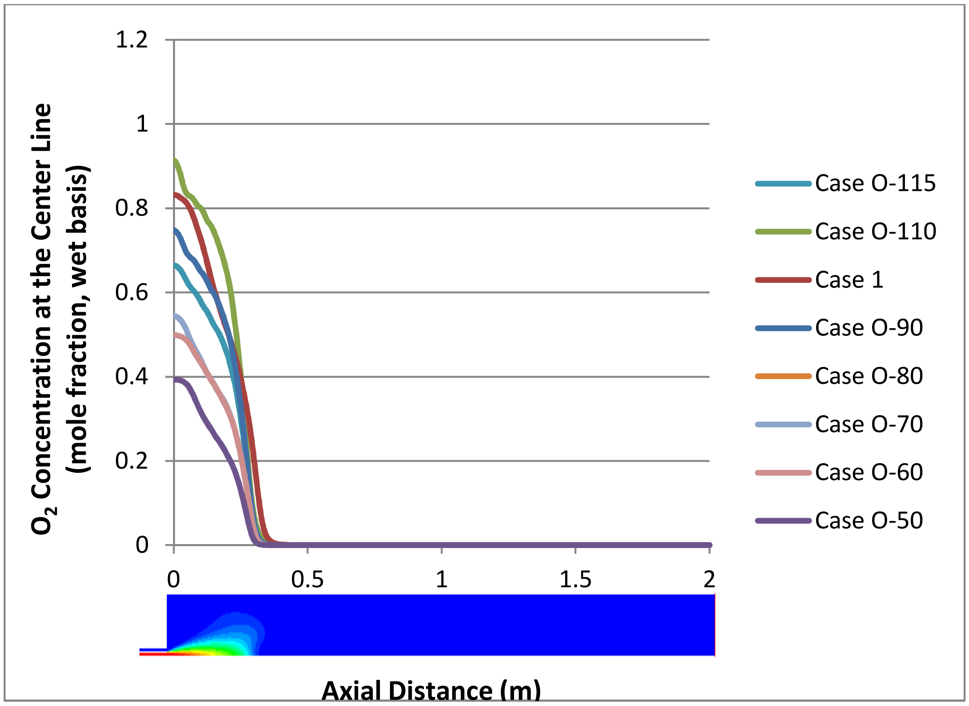

Figure 29: Comparison of concentrations from FLUENT prediction at the reactor centerline

4.5 Effect of Particle Size

This section investigates the effects of coal particle size. Studies have shown that particle size is a dominating factor governing gasifier carbon conversion [13], [21], [22], [23]. It is generally thought that by decreasing the particle size the increased surface area/volume ratio will cause smaller particles to react more quickly, increasing carbon conversion. Kumar et. al. reports;

> *"Determining the impact of particle size on carbon conversion is critical for two important reasons:*
>
> *(1) Depending on the particular gasifier design and stoichiometric ratio within specific regions of the gasifier, fine grinding of coal may or may not have a significant impact on carbon conversion rate. Accurate modeling can reveal this dependence and help make informed decisions.*
>
> *(2) There have been studies indicating that there is a premium in fine grinding of coal. Although the grinding energy itself might remain a miniscule fraction of the heating value, a more stringent requirement on grinding leads to a reduction in the mill capacity.*

> *The extent of reduction depends on the particular grinding mill employed and the grindability index of the coal used [7].”*

It has been found that fine grinding helps accelerate carbon conversion when the reactions are diffusion limited, but smaller particle sizes have been found to be detrimental when reactions are kinetically limited [22].

The effects of particle sizes were investigated by varying the individual particle sizes from “Case 1” to sizes 30% smaller and larger than the Case 1 size distribution. The particle size distribution for each case is shown in Table 8. For reference, the symmetrical contours of each species from the original case “Case 1” predictions are shown at the bottom of each figure in this section.

Table 8: Injection Pont Properties for Coal Particle Size Investigation.

Case	Case 1	30% Smaller	30% Larger
X-Velocity (m/s)	50.0	50.0	50.0
Y-Velocity (m/s)	0.0	0.0	0.0
Coal Particle Diameter 0(µm)	3.0	2.1	3.9
Coal Particle Diameter 1(µm)	20.0	14.0	26.0
Coal Particle Diameter 2(µm)	28.0	19.6	36.4
Coal Particle Diameter 3(µm)	50.0	35.0	65.0
Coal Particle Diameter 4(µm)	80.0	56.0	104.0
Temperature (K)	367.0	367.0	367.0
Total Flow Rate (kg/s)	0.001327	0.001327	0.001327

The mass fraction of converted carbon was calculated from the FLUENT predictions. The mass fraction of converted carbon is plotted in Figure 30. Figure 30 shows that as the particle size is decreased the mass fraction of converted carbon increases..

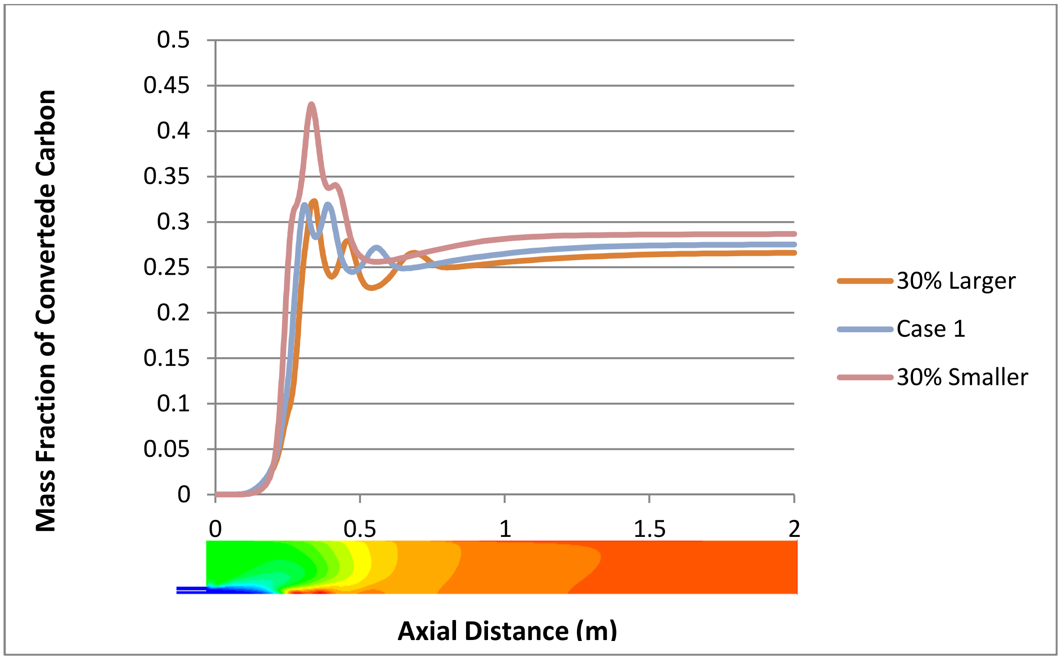

Figure 30: Mass fraction of converted carbon from FLUENT prediction at the reactor centerline for varying particle size

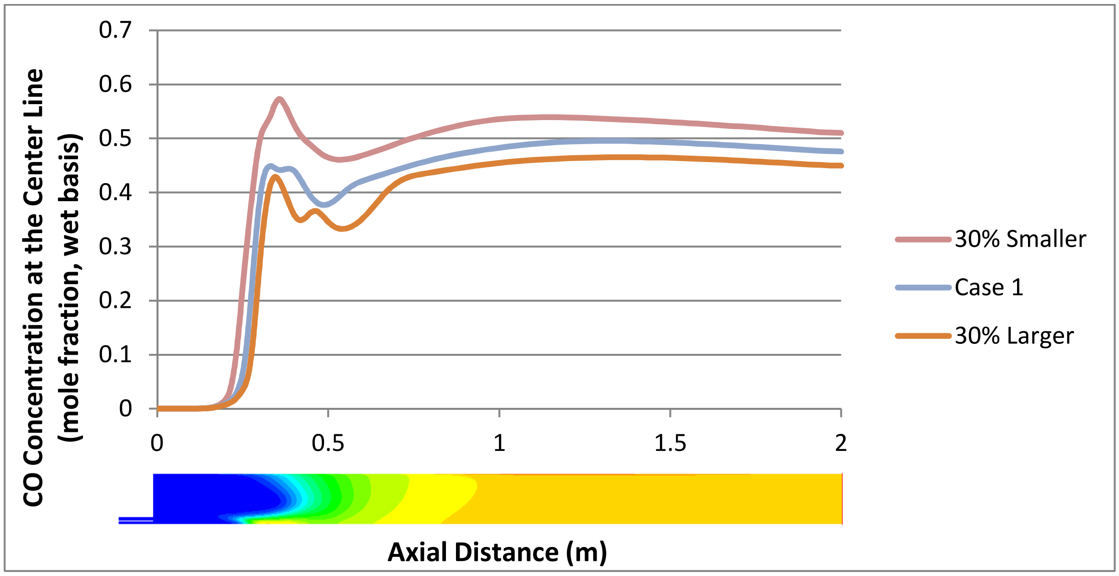

Figure 31: Comparison of concentrations from FLUENT prediction at the reactor centerline for varying particle size

Decreasing the Particle Size increases the *CO* concentrations, while decreasing the concentrations.

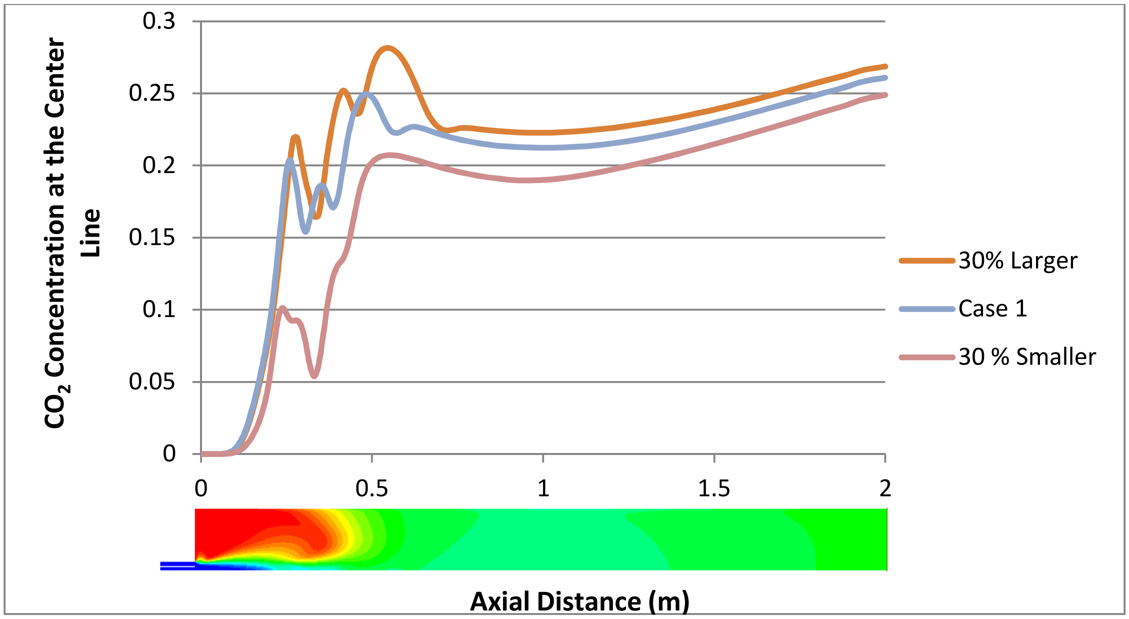

Figure 32: Comparison of concentrations from FLUENT prediction at the reactor centerline for varying particle size

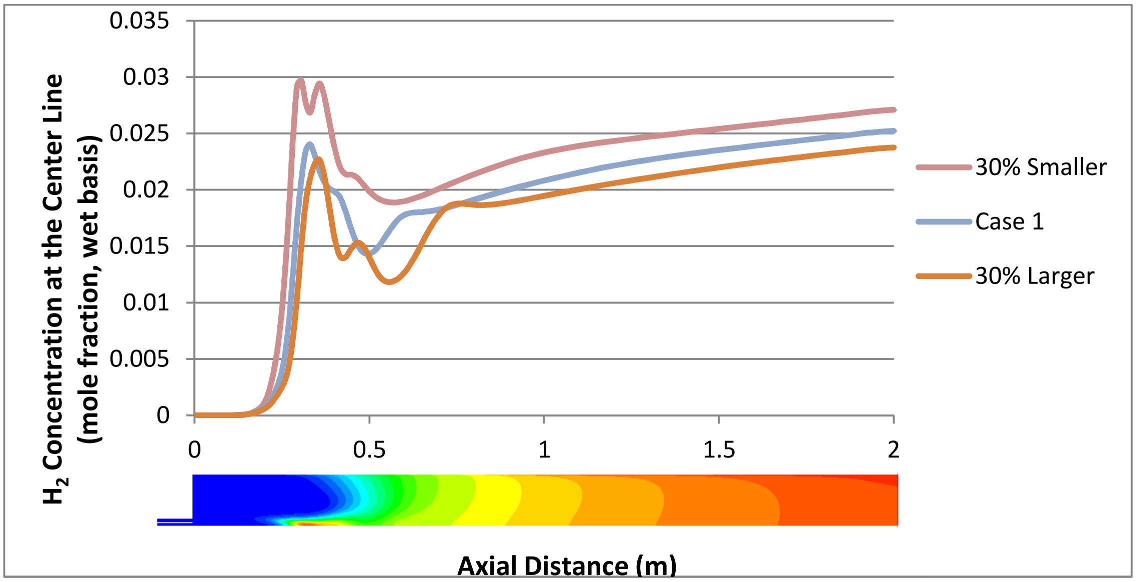

Figure 33: Comparison of concentrations from FLUENT prediction at the reactor centerline for varying particle size

Decreasing the Particle Size increases the concentrations while decreasing the moisture content.

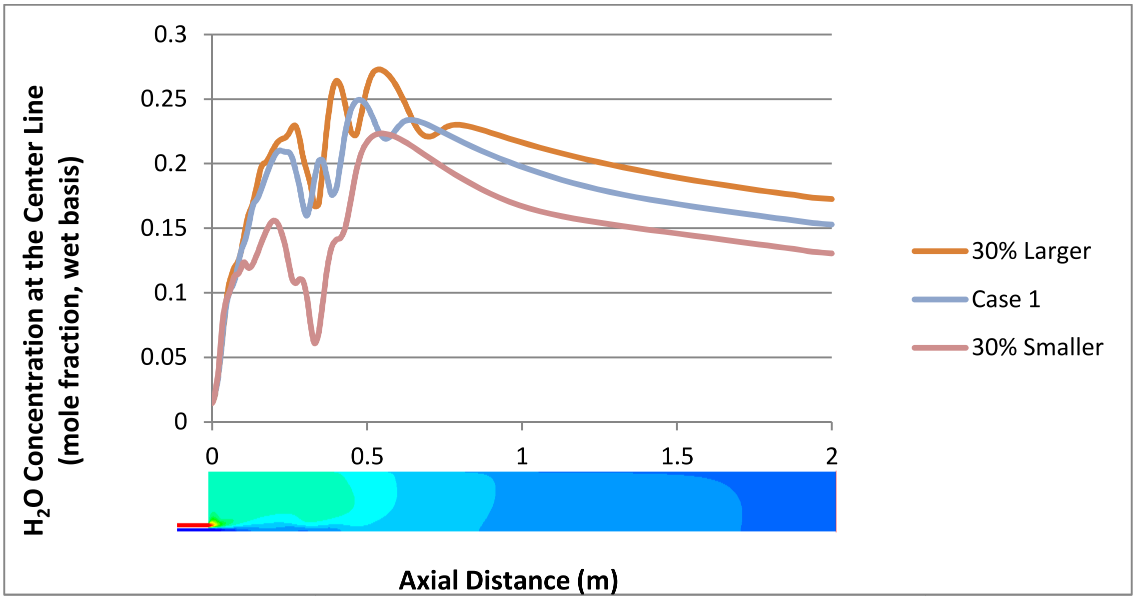

Figure 34: Comparison of concentrations from FLUENT prediction at the reactor centerline for varying particle size

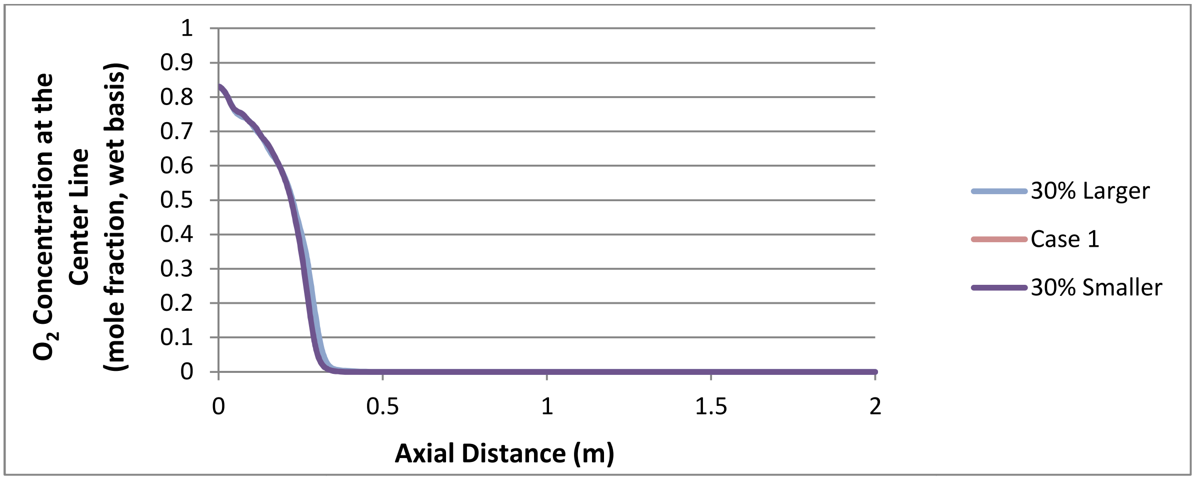

Figure 35: Comparison of concentrations from FLUENT prediction at the reactor centerline for varying particle size

Figure 35 shows no significant effect of particle size on oxygen concentrations.

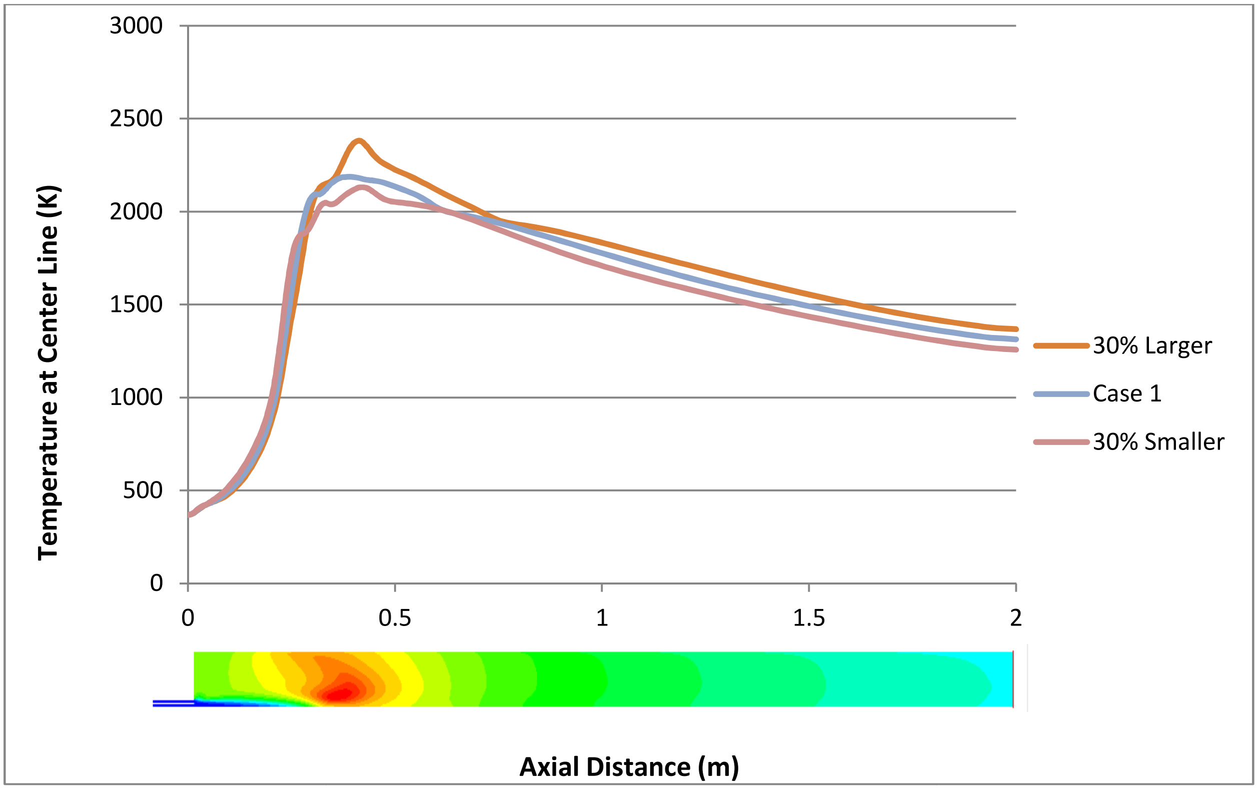

Figure 36: Comparison of Static Temperature (K) from FLUENT prediction at the reactor centerline for varying particle size

Figure 36 shows that as particle size decreases the exit gas temperatures decrease

4.6 Effects of Secondary Steam Temperatures

The effects of secondary inlet steam temperatures were investigated in this section. In the original case, Case 1, steam flows into the secondary inlet at 450 K. In order to investigate the effects of steam preheat temperatures two additional cases were run. The steam secondary inlet temperatures were raised to 1000 K and 1500 K, the cases are referred to as ST1000 and ST1500 respectively.

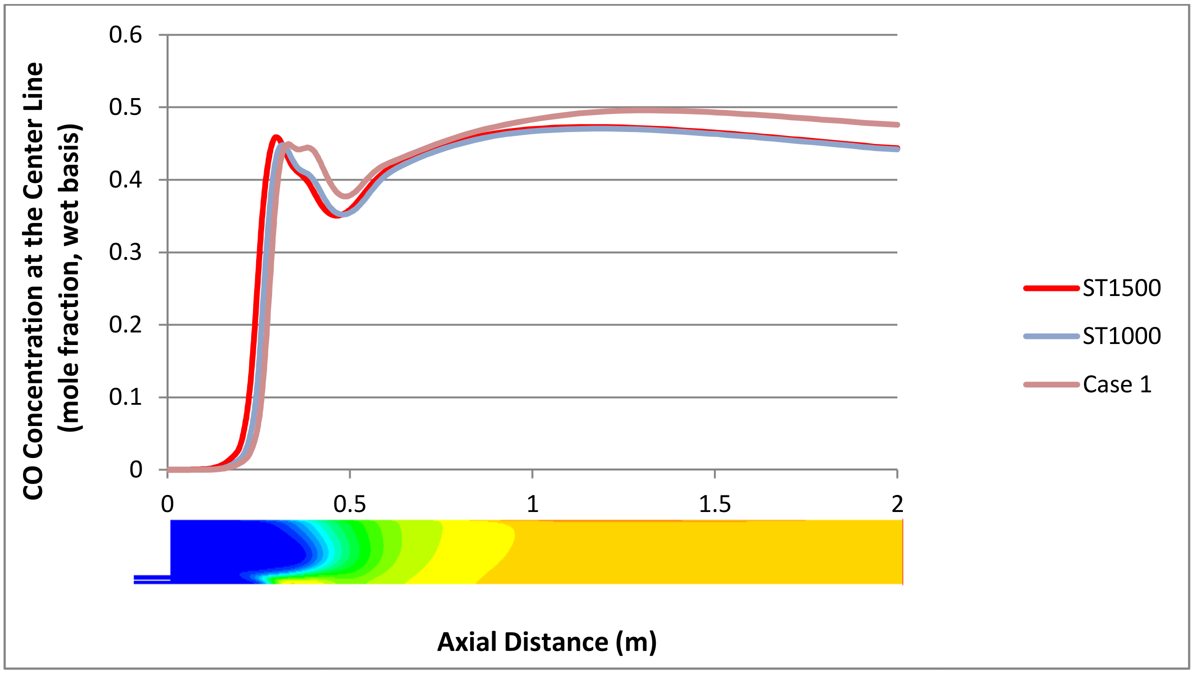

Figure 37: Comparison of concentrations from FLUENT prediction at the reactor centerline for varying steam prehat temperatures

Increasing the temperature from the original case reduced *CO* concentrations while increasing concentrations.

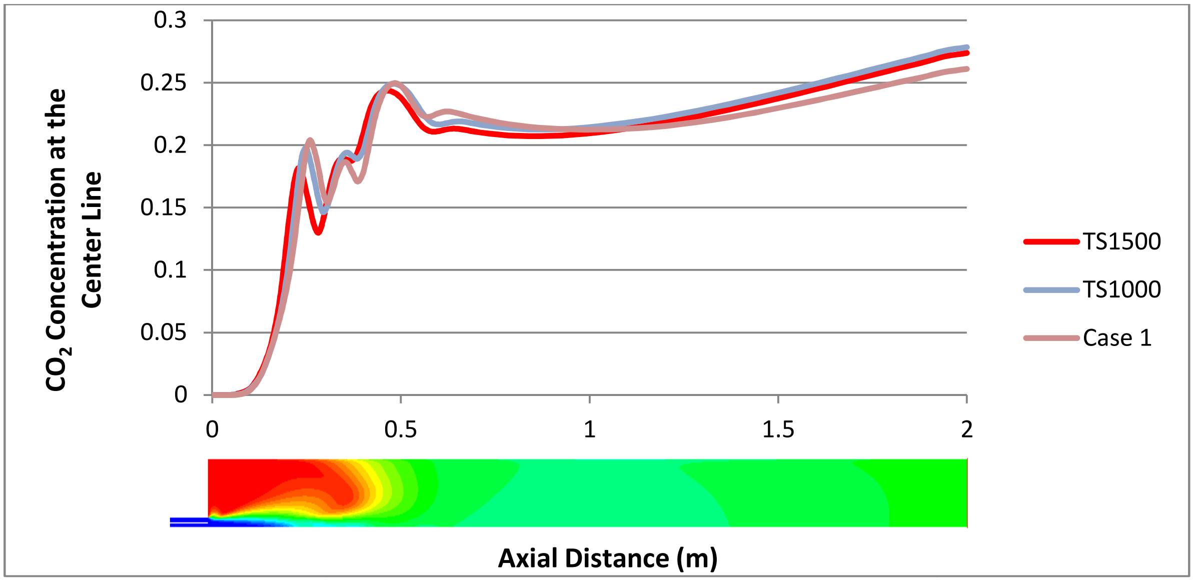

Figure 38: Comparison of concentrations from FLUENT prediction at the reactor centerline for varying steam prehat temperatures

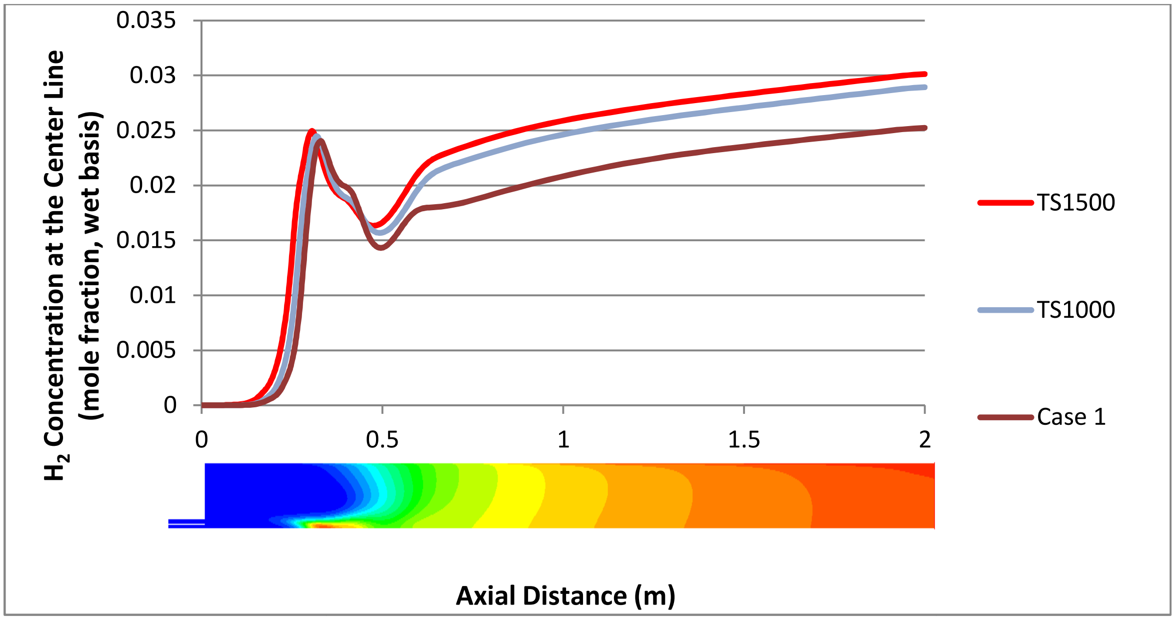

Figure 39: Comparison of concentrations from FLUENT prediction at the reactor centerline for varying steam prehat temperatures

Increasing the secondary inlet temperature increased concentrations, while increasing concentrations.

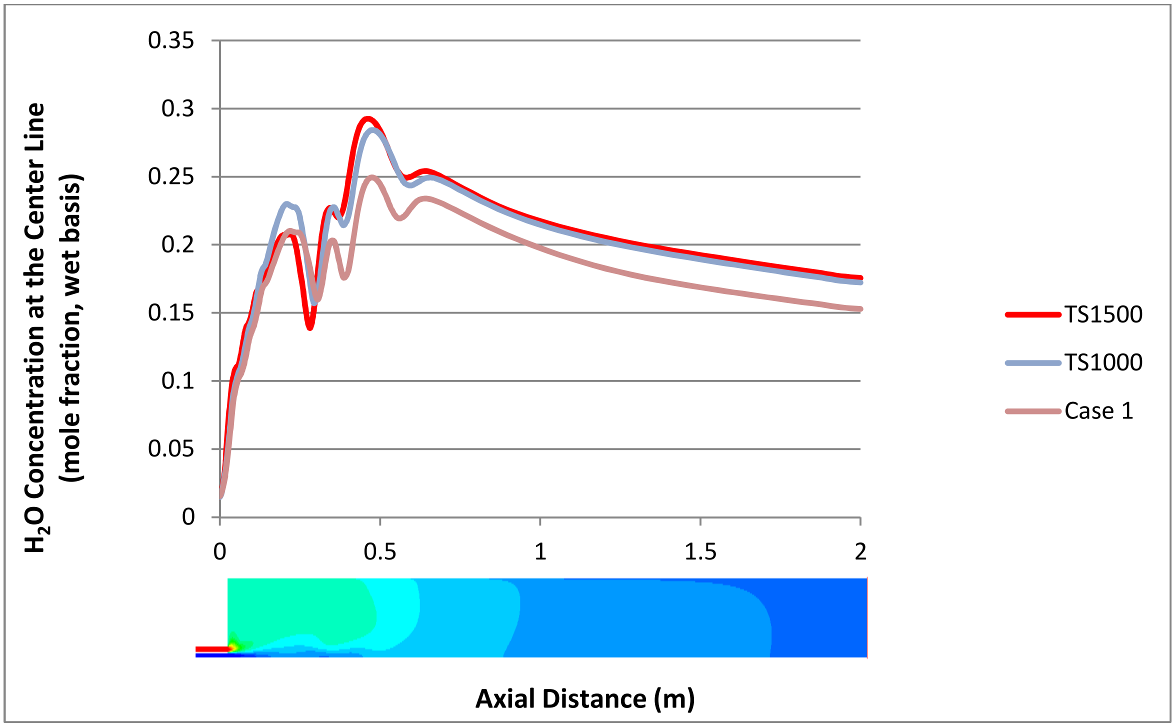

Figure 40: Comparison of concentrations from FLUENT prediction at the reactor centerline for varying steam prehat temperatures

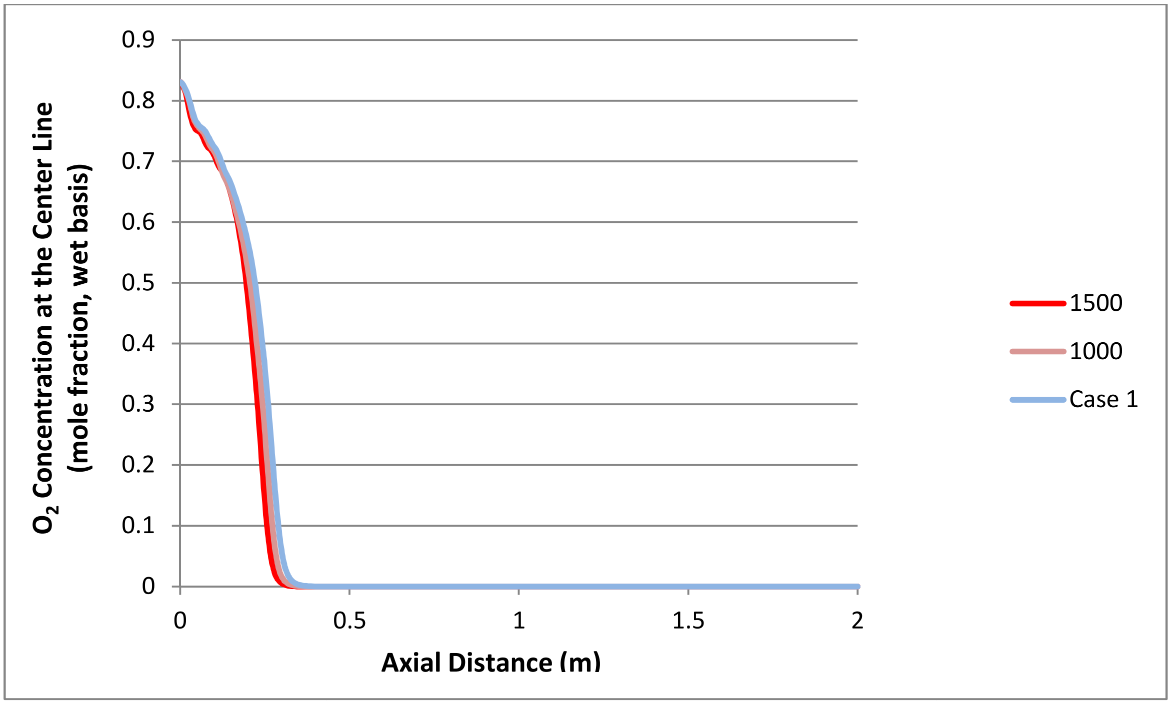

Figure 41: Comparison of concentrations from FLUENT prediction at the reactor centerline for varying steam prehat temperatures

Oxygen is consumed faster with increasing temperature.

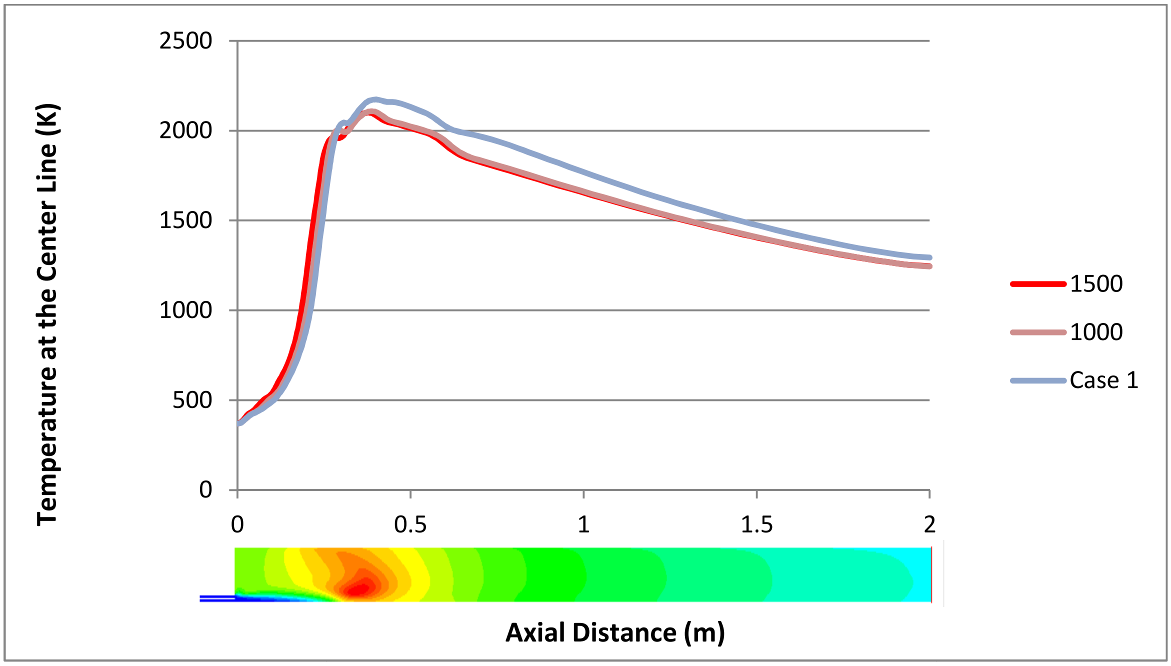

Figure 42: Comparison of Static Temperature (K) from FLUENT prediction at the reactor centerline for varying steam prehat temperatures

Increasing the temperature in the secondary inlet reduced exit temperatures.

CHAPTER 5

DISCUSSION

5.1 Effects of Steam Concentrations in the Secondary Inlet

Previouse research by Silaen et. al. has found that the higher the steam/coal ratio the lower the maximum temperature. It was also found that increasing the steam/coal ratio increases CO_2 and H_2 concentrations, while decreasing CO concentrations [22]. These trends were verivied in the present research. The effects of steam concentration in section 4.3 can be attributed to the water-gas shift reaction defined in chapter 3 as Reaction 7 and 8.

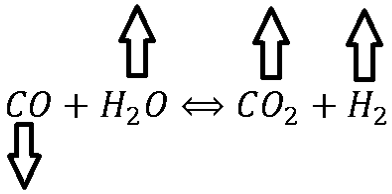

$$CO + H_2O \Leftrightarrow CO_2 + H_2$$

Figure 43: Characteristics of Reactions 7 and 8

From the forward reaction, Reaction 7, it can be seen that as H_2O is increased more CO is consumed to produce CO_2 and H_2.Thus decreasing the CO concentrations and increasing the CO_2 and H_2 concentrations.

PCGC-2 predictions showed no effect of steam input on exit hydrogen concentration which does not agree with experimental data trends [13]. Reaction rates for most coals, including Utah No. 5, were unavailable for most coals at the time. Brown states the reason for this discrepancy is that the kinetic data input to the model for the $C - CO_2$ reaction was for Wyoming coal, but the $C - H_2O$ reaction kinetic data was for graphite [13]. Using different data resulted in the predictive rate for the $C - CO_2$ reaction being much faster than the $C - H_2O$ reaction. Therefore no change in hydrogen was found because the $C - CO_2$ reaction dominated. This demonstrated the need for more reliable $C - H_2O$ reaction parameters. It can be seen from Fig. 43 that the Fluent predictions show a clear relation of steam concentration on hydrogen production. The function of steam inputs effect on exit hydrogen concentration is shown in Fig. 44 and follows a linear path. The function can be given by the equation

$$y = 0.0045x + 0.0209$$

where

$$R^2 = 0.998$$

Increasing the steam in the Secondary Inlet showed no significant effect on temperature.

5.2 Effects of Oxygen Concentrations in the Primary Inlet

The effects of oxygen concentrations on species concentrations can be attributed to the following reactions: the gas phase reaction, Reaction 6,

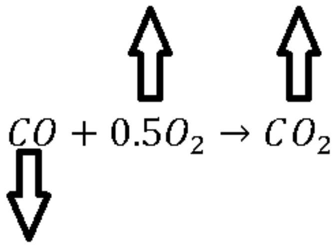

$$CO + 0.5O_2 \rightarrow CO_2$$

Figure 44: Characteristics of Reaction 6

the heterogeneous reaction, Reaction 2,

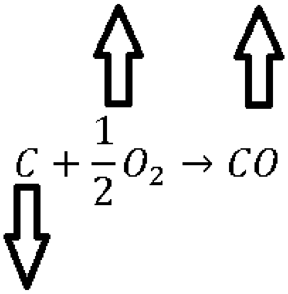

$$C + \frac{1}{2}O_2 \rightarrow CO$$

Figure 45: Characteristics of Reaction 2

as well as the volumetric combustion reaction, Reaction 5,

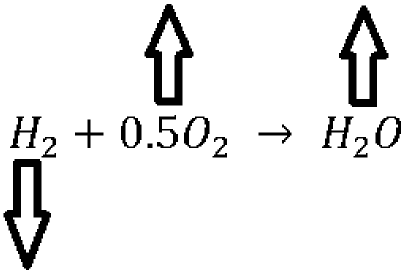

$$H_2 + 0.5O_2 \rightarrow H_2O$$

Figure 46: Characteristics of Reaction 5

From Reaction 6 it can be seen that as O_2 is increased more CO is consumed producing more CO_2. Similarly, from Reaction 2, as O_2 concentrations are increased more C is consumed producing more CO. It can be seen from Reaction 6 that as the O_2 is increased more H_2 is consumed producing more H_2O. Thus decreasing the H_2 concentrations and increasing H_2O concentrations.

The exit hydrogen concentration as a function of oxygen concentration is shown in Fig. 26 and can be describe by the second order polynomial equation

$$y = -0.0194x^2 + 0.0165x + 0.0282$$

where

$$R^2 = 0.999$$

Increasing oxygen in the primary stream generally increases temperature. The added oxygen allows for more complete combustion, thus raising the reactor temperatures.

5.3 Effects of Particle Size

It was found by Brown et. al. that decreasing the particle size increases carbon conversion. Brown found that the predicted carbon conversion approximately followed the fourth root of the particle diameter for individual particles being gasified jointly in a given distribution [13]. Silaen et. al. [23] found that, “Generally speaking, larger particles produce more H_2, less CO, higher exit gas temperature, and more CO_2, and are hence less efficient. Similar results were found by Cheng who found, “carbon conversion at the gasifier exit decreases with increasing equivalence ratio or increasing particle size [21].”

In the present research it was found that carbon conversion increases with decreasing particle size, which agrees with previous studies. As the particle size is decreased the increased surface area/volume ratio causes smaller particles to react more quickly, thus increasing carbon conversion.

Other effects of particle size observed in Figures 31 through 34 can be explained by identifying the respective limiting mechanism of char consumption, weather the char consumption reactions are dominated by heterogeneous kinetics or diffusive transport to the particle surface. This limiting mechanism depends on the particle size, temperature in the vicinity of the particle, and availability of the respective gasification/combustion agents, O_2 or CO_2 and H_2O [23]. Kumar’s research found that “While the diffusion limitation of the $C - O_2$ reaction, defined as Reaction 2, becomes stronger with increasing particle size, the kinetics limitation of $C - CO_2$ and $C - H_2O$ reactions becomes weaker with increasing particle size.”

Literature suggests that since the $C - CO_2$ reaction, Reaction 2, is more diffusion limited with increasing particle size, Reaction 2 and its products are more limited with increasing particle size. Similarly, since the kinetic limitations of $C - CO_2$ and $C - H_2O$ reactions and there products become weaker with increasing particle size, reactions 4 and 5 are stronger with increasing particle size. Kumar's research found that generally speaking, larger particle sizes produce less CO, more CO_2 and H_2, and produce higher exit gas temperatures [23].

FLUENT predictions show similar trends as reported in the literature except for the H_2 concentrations. Figure 31, and 32 respectively show that as particle size is increased CO concentration decreases and CO_2 concentration increases. Figure 33 shows the H_2 concentrations decreases with larger particle sizes which does not agree with literature. The reason for this inconsistency is unknown. Further investigation should be performed in order to better understand this discrepancy.

Kumar also found that generally the exit temperature increases with larger particle sizes. This trend can be seen in Figure 36. As the particle size is increased the exit gas temperature is increased. Kumar states that the reason for higher exit temperatures for larger particle sizes in his case could be attributed to the kinetic limited reactions. Kinetically driven reactions, larger particles, which have greater inertia, are allowed to recirculate through critical reaction zones allowing further reactions. Kumar found that smaller particles can lead to less complete combustion of syngas species due to poor convective transport of heat and species concentrations, therefore reducing the exit temperatures as particle size is decreased.

5.4 Effects of Steam Temperature in the Secondary Inlet

The effects of steam preheat temperatures is similar to the effects of steam concentrations. The trends observed in both cases can be attributed to the water gas shift reaction, discussed in detail in section 5.1. Raising the temperature of the H_2O molecules increases the energy available for the CO -H_2O reaction. Thus decreasing the CO concentrations and increasing the CO_2 and H_2 concentrations as displayed in Figure 43.

CHAPTER 6
CONCLUSIONS AND RECOMENDATIONS

The present research validates the CFD Fluent model prediction of an entrained-flow coal gasifier. Systematic examination of the model was performed by varying inlet concentrations of steam and oxygen in regular intervals. Mesh was verified by quadrupling the refinement and comparing it to the original mesh. Convergence was tested and the model was validated with experimental data from several studies performed on a laboratory scale gasifier. Two turbulence models were investigated in this study.

The Standard $k - \varepsilon$ model showed the best agreement with experimental data. The Standard $k - \varepsilon$ Fluent model shows good agreement with experimental data in the forward region of the gasifier from the inlet up to about the 0.40 meter axial position. This suggests sufficient modeling of the devolatilization. After the 0.40 meter position the experimental data and Fluent predictive data have larger relative error. The error in the aft region suggests additional studies should look further into the modeling of the volumetric heterogeneous reactions.

Model predictions found that increasing the steam concentration in the secondary inlet generally decreases CO production, increases CO_2 concentrations decreasing the CO/CO_2 ratio while increasing the H_2 concentrations. This was true except for the cases with 60 to 80 % steam concentration of the base line case. In these cases the CO and CO_2 concentrations do not follow the general trend. Further research shoud be perfomed on that region to seek insight into this deviation from the trend.It was also found that increasing the steam content in the secondary inlet showed no signifigant effect on predicted temperatures inside the gasifier. Increasing the oxygen concentration in the primary inlet generally increases temperature. As well as increasing the CO production, while decreasing the H_2 concentrations. Increasing the steam prehat temperatures followed similar trends of increased steam concentration.

It was found that decreasing the coal particle size increases carbon conversion, CO production, and H_2 production, while decreasing CO_2 concentrations. Results show good agreement with literature except for the H_2 concentrations. Literature sugests H_2 concentrations should decrease as particle size is decreased. The results from the present study show the H_2 concentrations increasing with decreasing particle size. Further research should be performed to investigate this discrepency.

Further research should also investigate the effects of steam and oxygen inlet concentrations and preheat temperatures as well as the effects particle size for different coal types. Information from this research should then be used to attempt to optimize the gasifiers operating conditions. Further research should also include the applications of different feedstock. These could include renewable energy sources such as biomass and solid waste.

BIBLIOGRAPHY

[1] A. F. Ghoniem. “Needs, resources and climate change: Clean and efficient conversion technologies”. *Prog. Energy Combust. Sci., 37*(1) (April 2010) 15–51.

[2] Energy Information Administration. *World Energy Projections Plus* (2009)

[3] Jacques Lahaye and Pierre Ehrburger. Fundamental Issues in Control of Carbon Gasification Reactivity. *NATO ASI Series.* Series E: Applied Sciences – Vol. 192. (August 1990)

[4] Perry, H. The Gasification of Coal, *Scientific American*, 220, (3) (March 1974) 19-25.

[5] James G. Speight. Handbook of Industrial Hydrocarbon Processes. *Gulf Professional Publishing.* . (December 2010)

[6] *National Energy Technology Laboratory [NETL]. Gasification Database: Active and Planned Commercial Gasification Plants* (2007)

[7] Kumar, Mayank. Multiscale CFD Simulations of Entrained Flow Gasification. Ph.D. *Massachusetts Institute of Technology* (September 2011)

[8] Pamela Fehl. Green Careers: Energy. *Infobase Publishing* (2010)

[9] Holden, J.H., et al. Operation of Pressure-Gasification Pilot Plant utilizing Pulverized Coal and Oxygen: A Progress Report. *Report of Investigations 5573, I U.S. Dept. of the Interior, Bureau of Mines* (1960)

[10] Holden, J.H., Plants, K.D., et al. Operating a Pressurized Gasification Pilot I Plant Using Pulverized Coal and Oxygen: Effect of Heat Loss on Economy. *Report of Investigations 5956, U.S. Dept. of the Interior, Bureau of Mines* (1962)

[11] Coates, R.L., High Rate Coal Gasification. American Institute of Chemical Engineers, Coal Processing Technology – Vol. 3, 89-94 (1977)

[12] McIntosh, M.J., Coates, R.L. Experimental and Process Design Study of a High Rate Entrained Coal Gasification Process. *Final Report under Contract No. EX-76-C-01-1548, Eyring Research Institute* (1978)

[13] Blain W. Brown. Effect of Coal Type on Entrained Gasification. Ph.D. *Brigham Young University*. (August 1985)

[14] Nakles, D.V. et. al. Formation/decomposition of condensable hydrocarbons during the gasification of coal. *Department of Energy, Pittsburgh, PA (USA). Pittsburgh Energy Technology Center; Carnegie-Mellon Univ., Pittsburgh, PA (USA). Dept. of Chemical Engineering.* (March 1982)

[15] Chiang liu Chen et. al. Mountain fuel resources 30 tons per day entrained flow coal gasification process development unit. *Questar Development Corporation.*

[16] Skinner, F.D. Mixing and Gasification of Pulverized Coal. Ph.D. *Brigham Young University* (1980)

[17] Wen, C. Y., Chaung, T. Z. Entrainment coal gasification modeling. *Ind. Eng. Chem. Process Des. Dev., 18*(4) (1979) 684–695.

[18] Chen, C., Horio, M., Kojima, T. Numerical simulation of entrained flow coal gasifiers. part ii: effects of operating conditions on gasifier performance. *Chem. Eng. Sci., 55*(18) (September 2000) 3875–3883

[19] Chen, C., Horio,M., Kojima, T. Use of numerical modeling in the design and scale-up of entrained flow coal gasifiers. *Fuel, 80*(10), (November 2001) 1513–1523.

[20] Watanabe, H., Otaka ,M. Numerical simulation of coal gasification in entrained flow coal gasifier. *Fuel, 85*(12-13), (November 2006) 1935–1943.

[21] Zhang, Cheng. Numerical Modeling of Coal Gasification in an Entrained-Flow Gasifier. *ASME International Mechanical Engineering Congress & Exposition.* (November 2012)

[22] Mayank Kumar, Cheng Zhang, Rory F.D. Monaghan, Simica L. Singer, Ahmed F. Ghoniem. *CFD Simulation of Entrained Flow Gasification with Improved Devolatilization and Char Consumption Submodels.* Proceedings of the ASME 2009 International Mechanical Engineering Congress & Exposition IMECE2009 (November 2009)

[23] Armin Silaen. Comprehensive Modeling and Numerical Investigation of Entrained-Flow Coal Gasifiers. Ph. D. University of New Orleans (May, 2010)

Appendix A

"Case 1" Contours

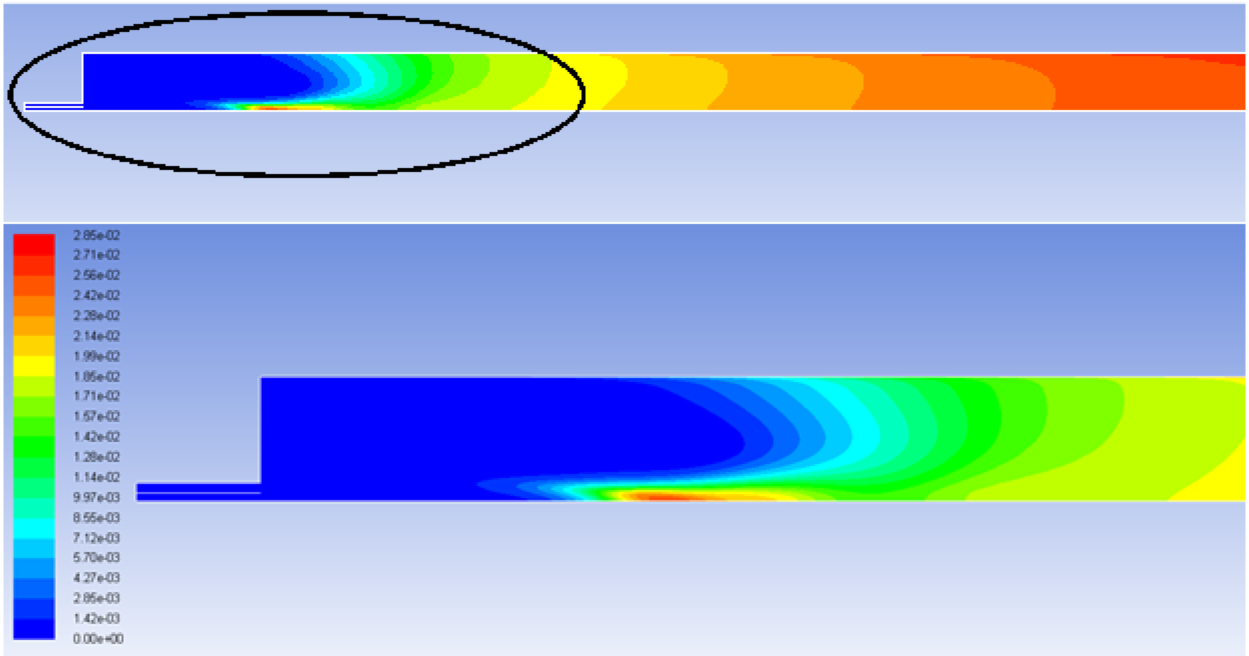

Figure 47: Contours of H_2 Mass Fraction from Fluent Prediction

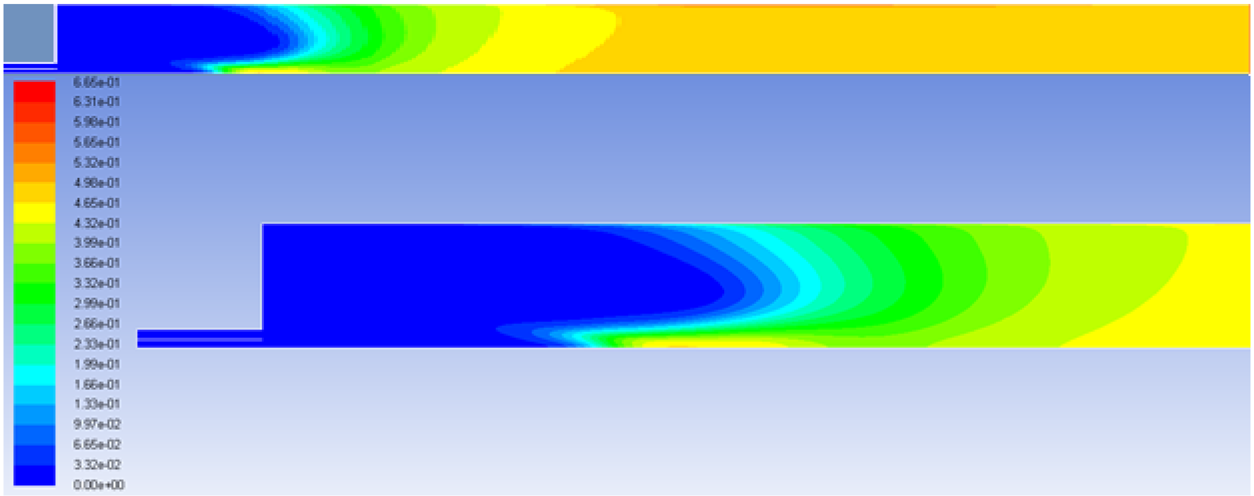

Figure 48: Contours of CO Mass Fraction from Fluent Prediction

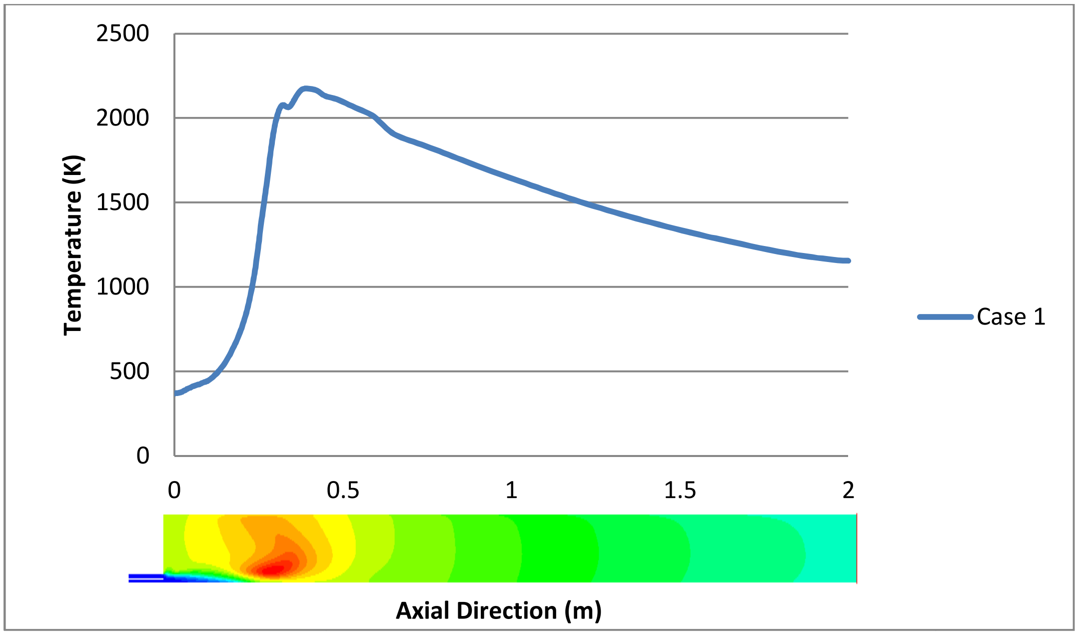

Figure 49: Static Temperature (K) at Centerline

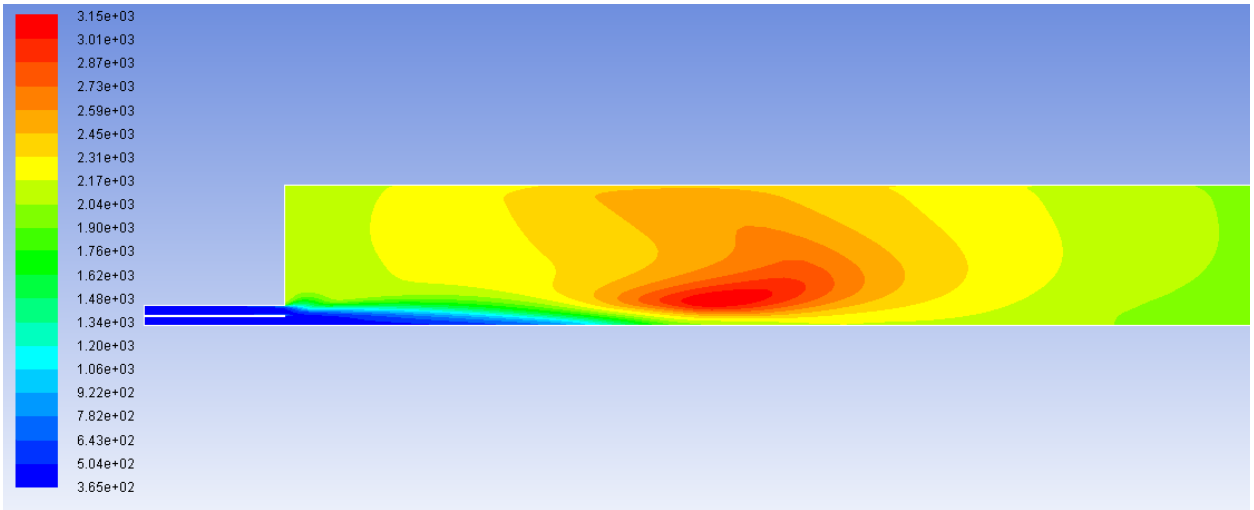

Figure 50: Contours of Static Temperature (K) from Fluent Prediction

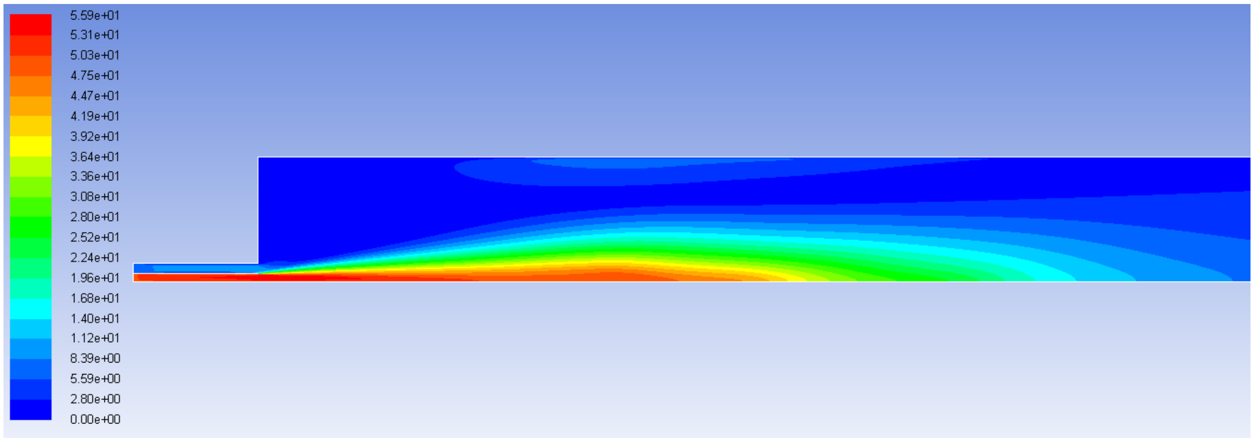

Figure 51: Contours of Velocity Magnitude from Fluent Prediction

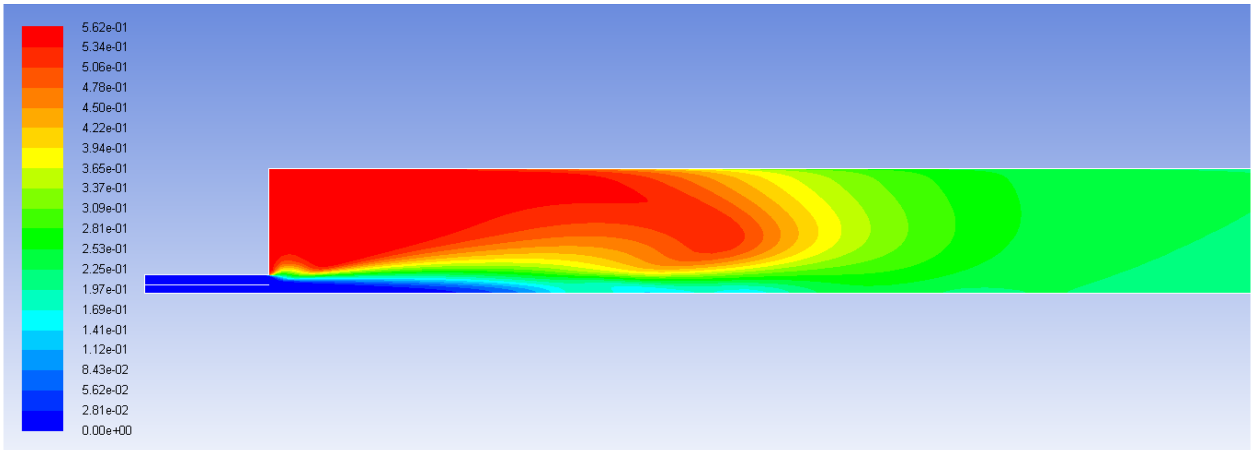

Figure 52: Contours of CO_2 Mass Fraction from Fluent Prediction

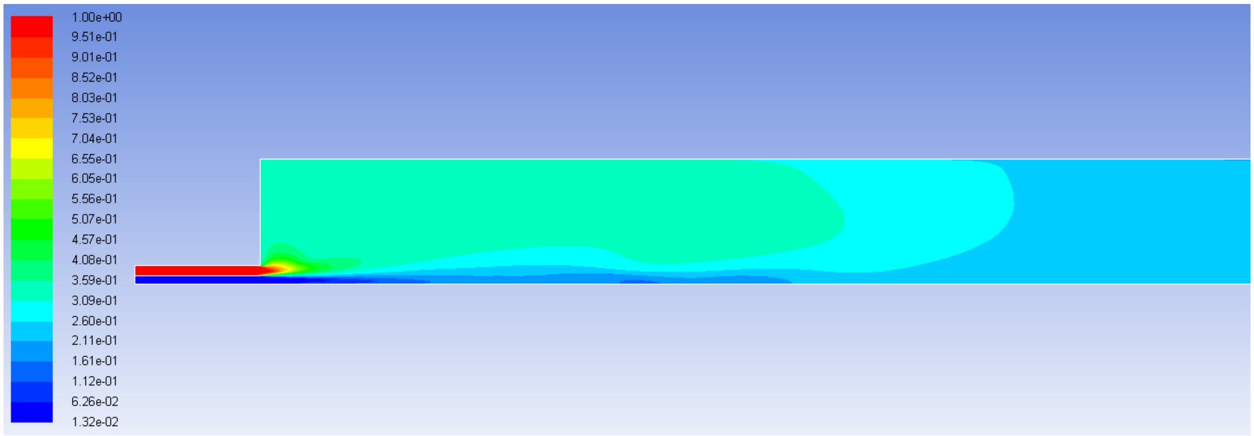

Figure 53: Contours of H_2O Mass Fraction from Fluent Prediction

Appendix B

Species Radial Profile Comparison of Brown's 1985

Experimental Data and the "Case 1" FLUENT Predictions

Radial Profiles for *CO* concentration.

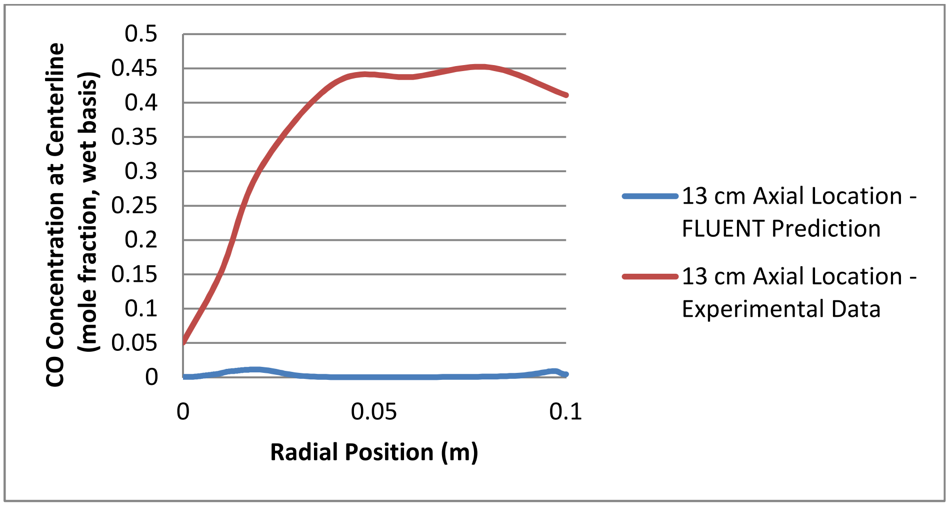

Figure 54: Axial Location 13 cm: Radial profile of *CO* concentration from Brown's 1985 Experimental Data and the "Case 1" FLUENT Predictions

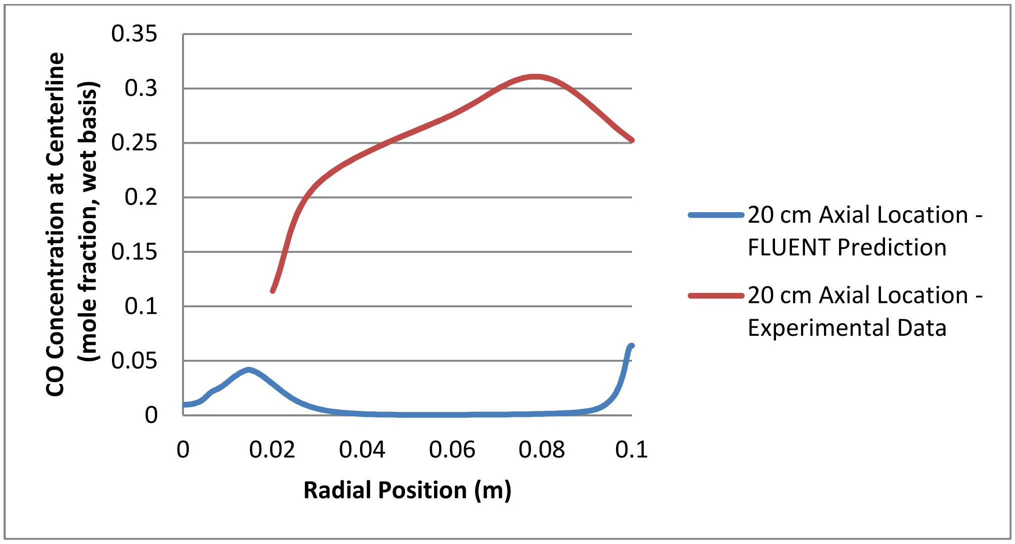

Figure 55: Axial Location 20 cm: Radial profile of *CO* concentration from Brown's 1985 Experimental Data and the "Case 1" FLUENT Predictions

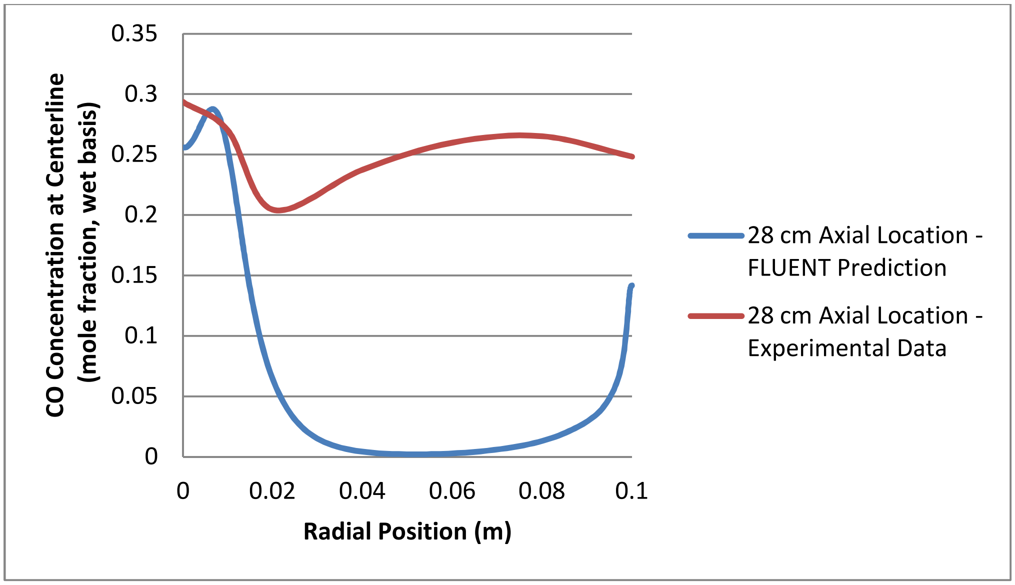

Figure 56: Axial Location 28 cm: Radial profile of *CO* concentration from Brown's 1985 Experimental Data and the "Case 1" FLUENT Predictions

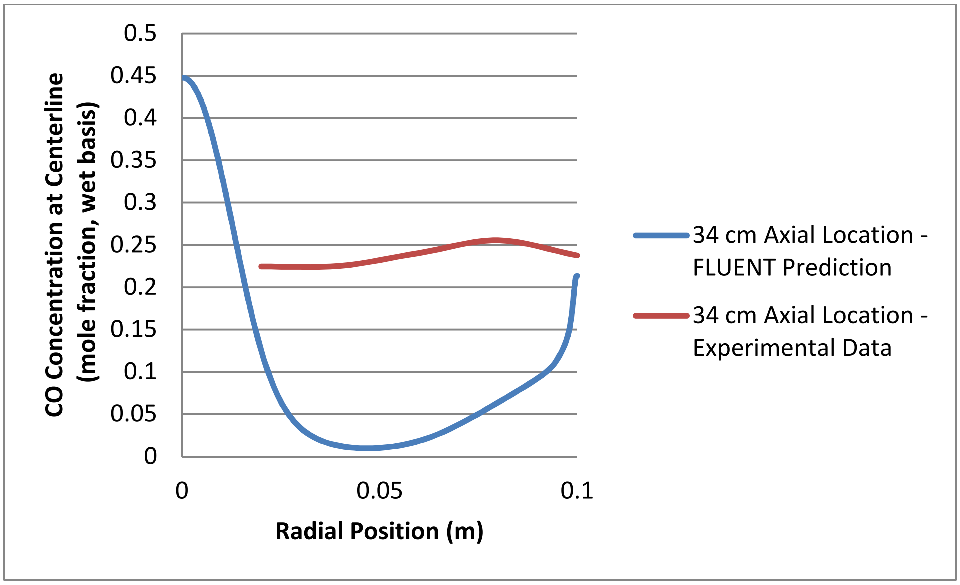

Figure 57: Axial Location 34 cm: Radial profile of *CO* concentration from Brown's 1985 Experimental Data and the "Case 1" FLUENT Predictions

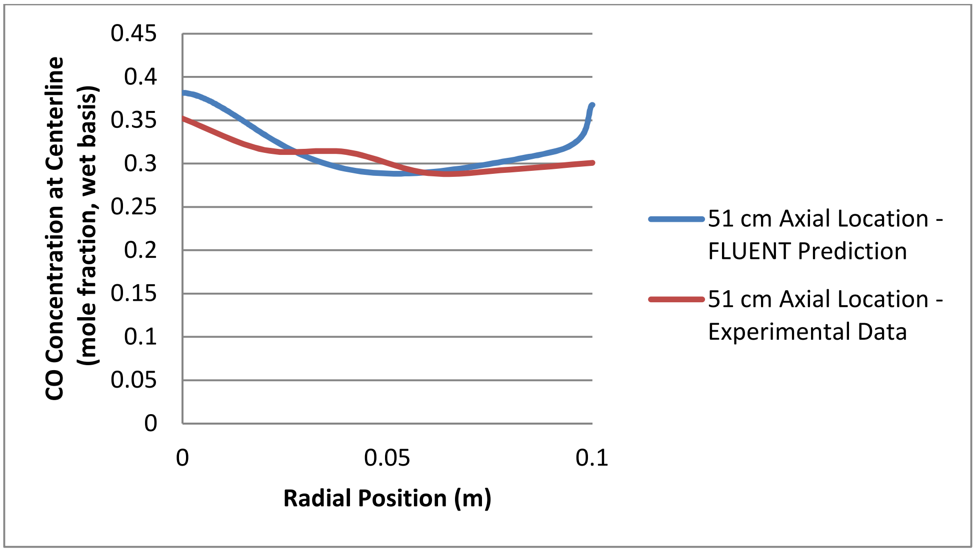

Figure 58: Axial Location 51 cm: Radial profile of *CO* concentration from Brown's 1985 Experimental Data and the "Case 1" FLUENT Predictions

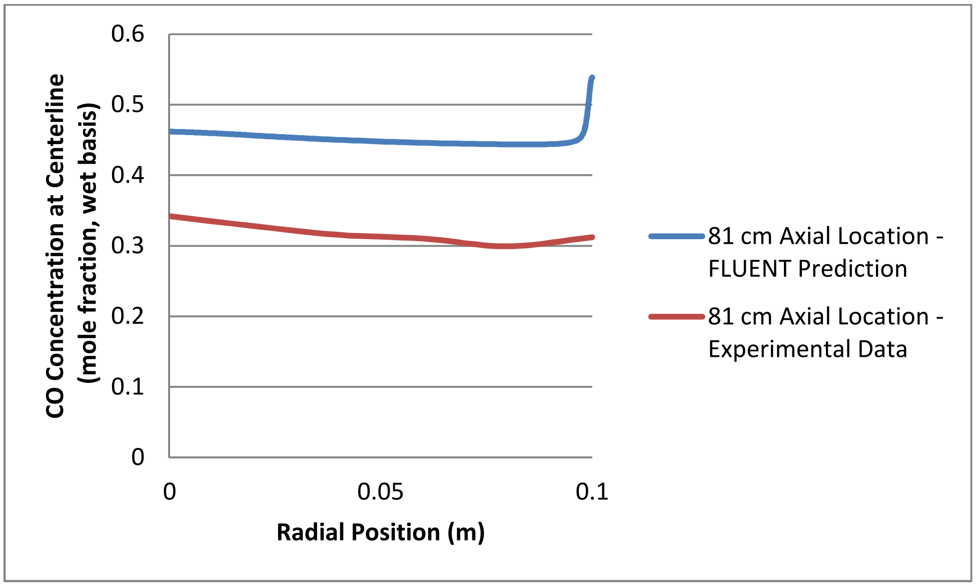

Figure 59: Axial Location 81 cm: Radial profile of *CO* concentration from Brown's 1985 Experimental Data and the "Case 1" FLUENT Predictions

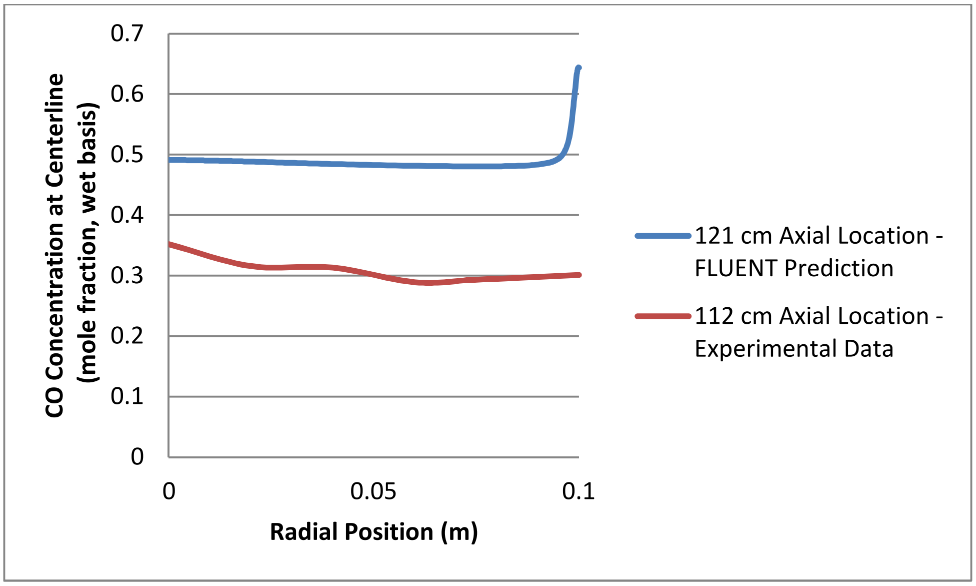

Figure 60: Axial Location 112 cm: Radial profile of *CO* concentration from Brown's 1985 Experimental Data and the "Case 1" FLUENT Predictions

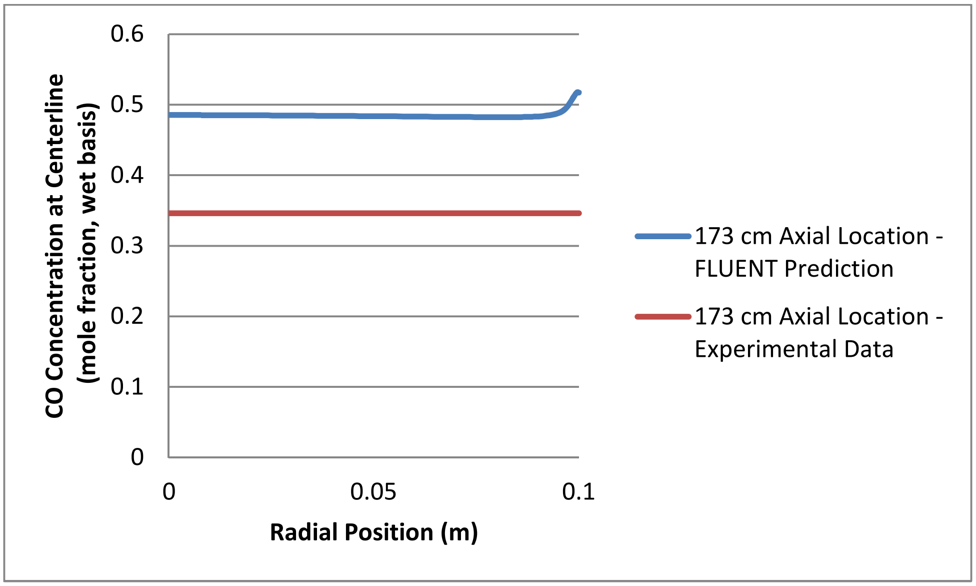

Figure 61: Axial Location 173 cm: Radial profile of *CO* concentration from Brown's 1985 Experimental Data and the "Case 1" FLUENT Predictions

Radial Profiles for CO_2 concentration.

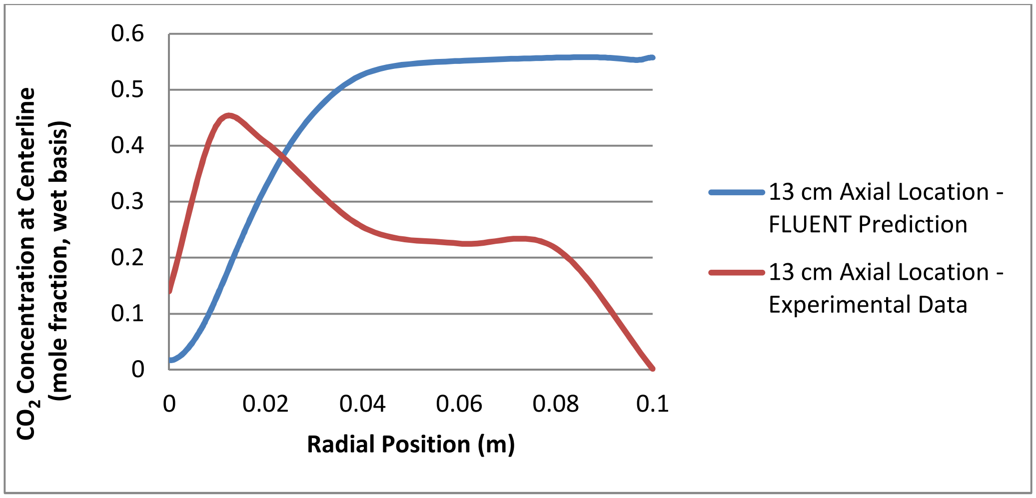

Figure 62: Axial Location 13 cm: Radial profile of CO_2 concentration from Brown's 1985 Experimental Data and the "Case 1" FLUENT Predictions

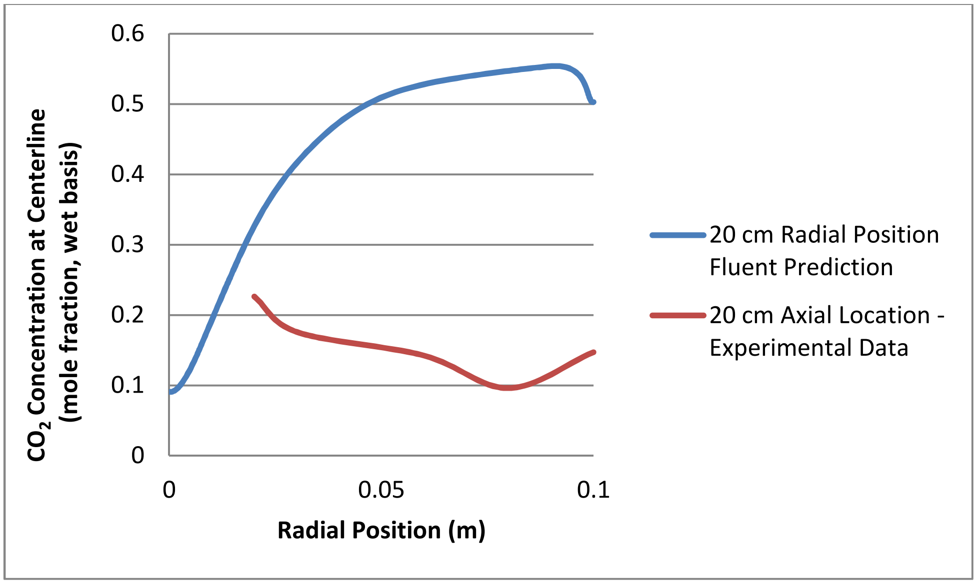

Figure 63: Axial Location 28 cm: Radial profile of CO_2 concentration from Brown's 1985 Experimental Data and the "Case 1" FLUENT Predictions

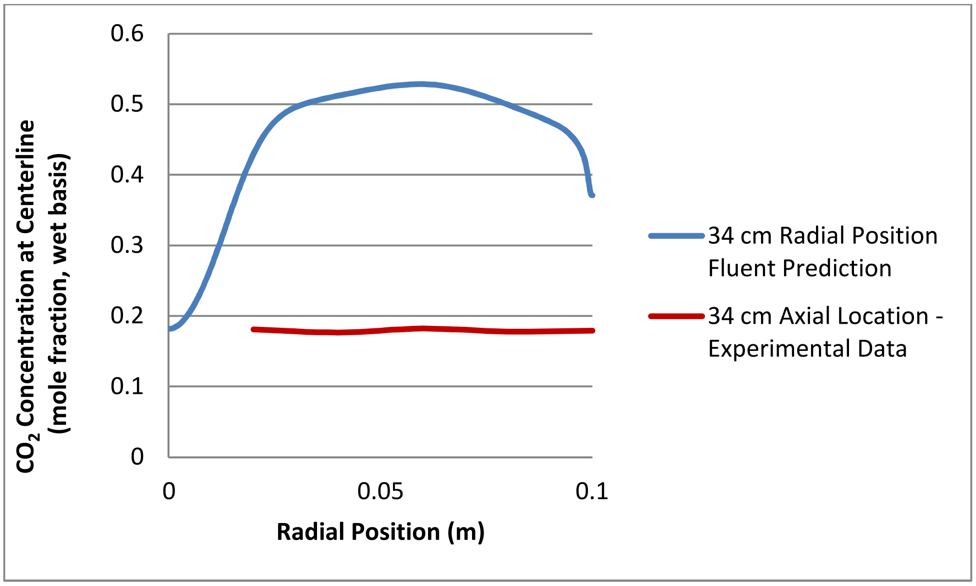

Figure 64: Axial Location 34 cm: Radial profile of CO_2 concentration from Brown's 1985 Experimental Data and the "Case 1" FLUENT Predictions

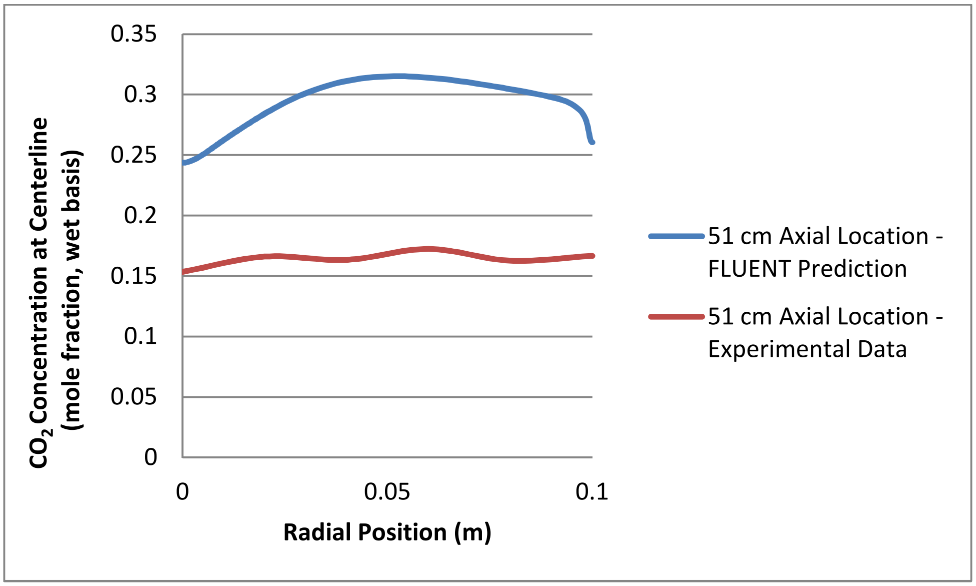

Figure 65: Axial Location 51 cm: Radial profile of CO_2 concentration from Brown's 1985 Experimental Data and the "Case 1" FLUENT Predictions

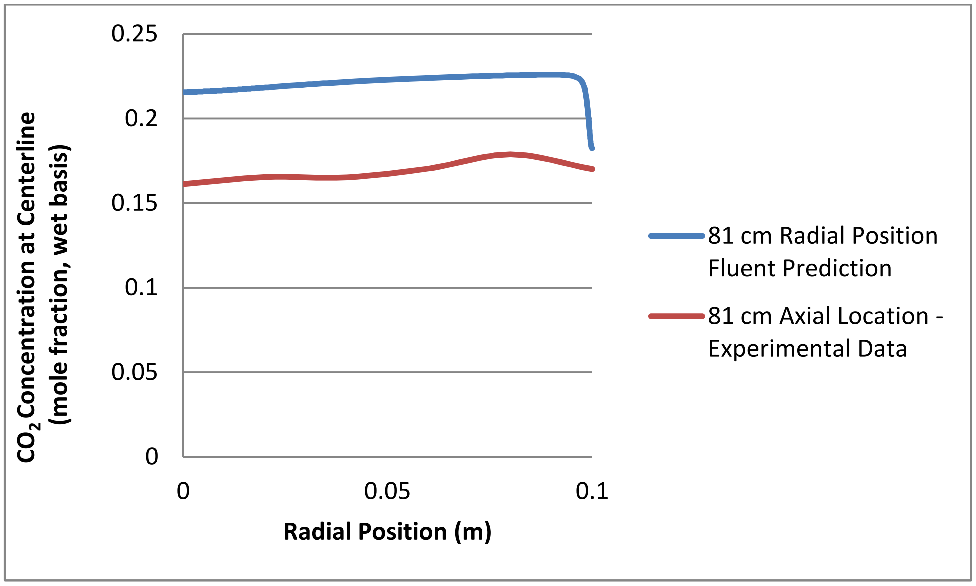

Figure 66: Axial Location 81 cm: Radial profile of CO_2 concentration from Brown's 1985 Experimental Data and the "Case 1" FLUENT Predictions

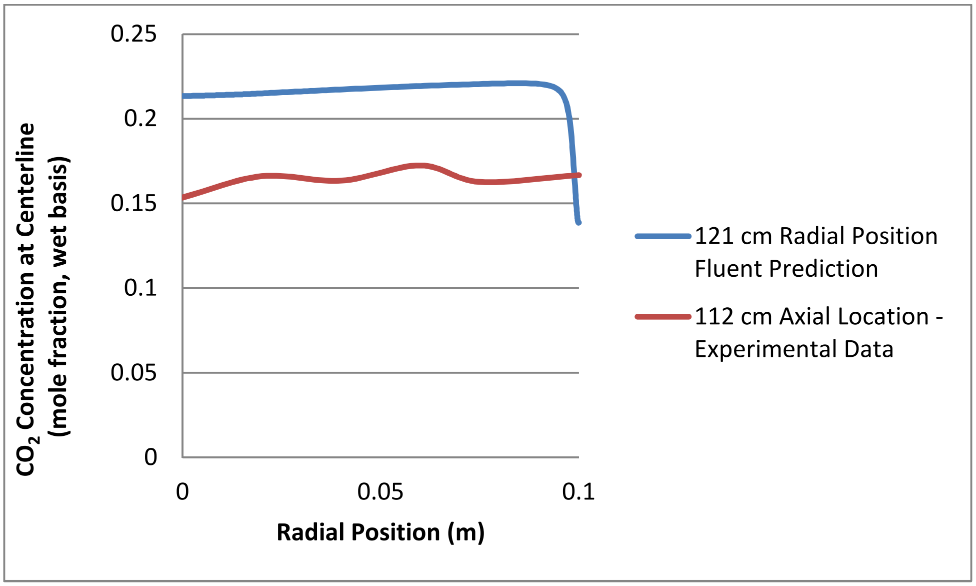

Figure 67: Axial Location 121 cm: Radial profile of CO_2 concentration from Brown's 1985 Experimental Data and the "Case 1" FLUENT Predictions

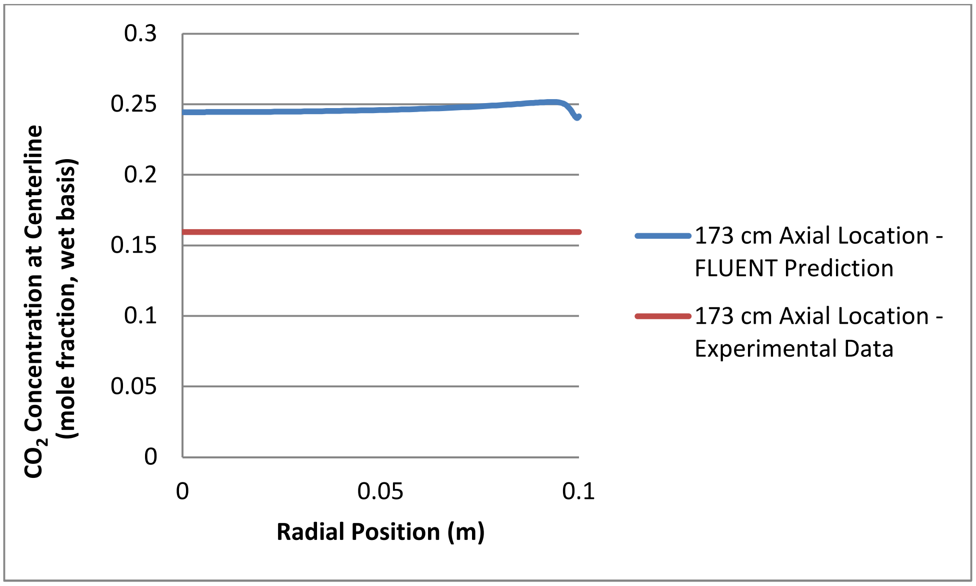

Figure 68: Axial Location 173 cm: Radial profile of CO_2 concentration from Brown's 1985 Experimental Data and the "Case 1" FLUENT Predictions

Radial Profiles for H_2 concentration.

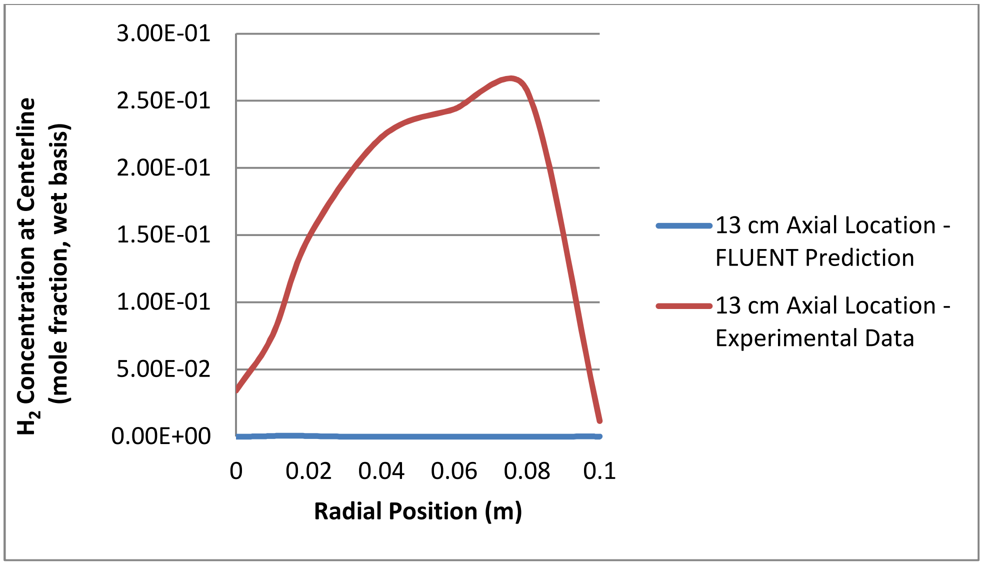

Figure 69: Axial Location 13 cm: Radial profile of H_2 concentration from Brown's 1985 Experimental Data and the "Case 1" FLUENT Predictions

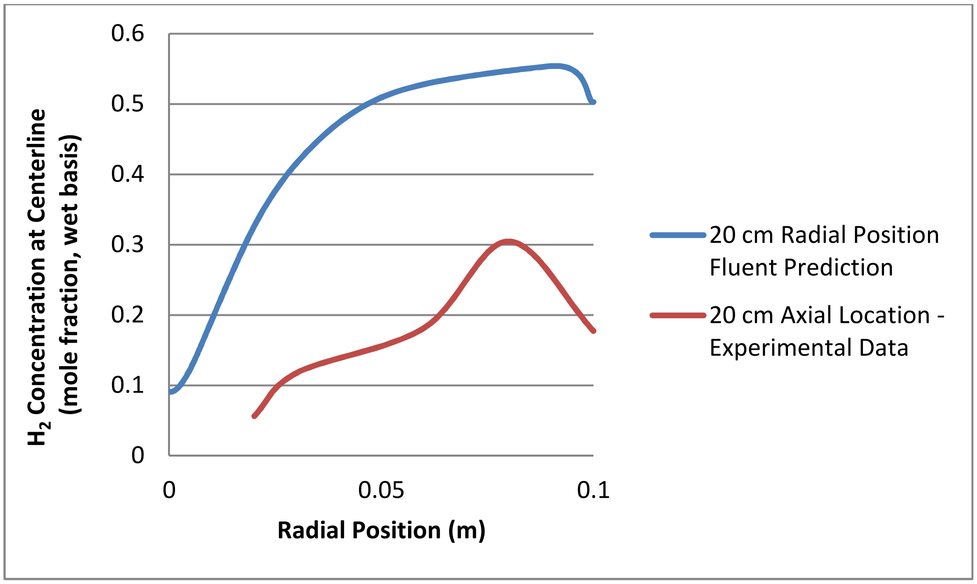

Figure 70: Axial Location 20 cm: Radial profile of H_2 concentration from Brown's 1985 Experimental Data and the "Case 1" FLUENT Predictions

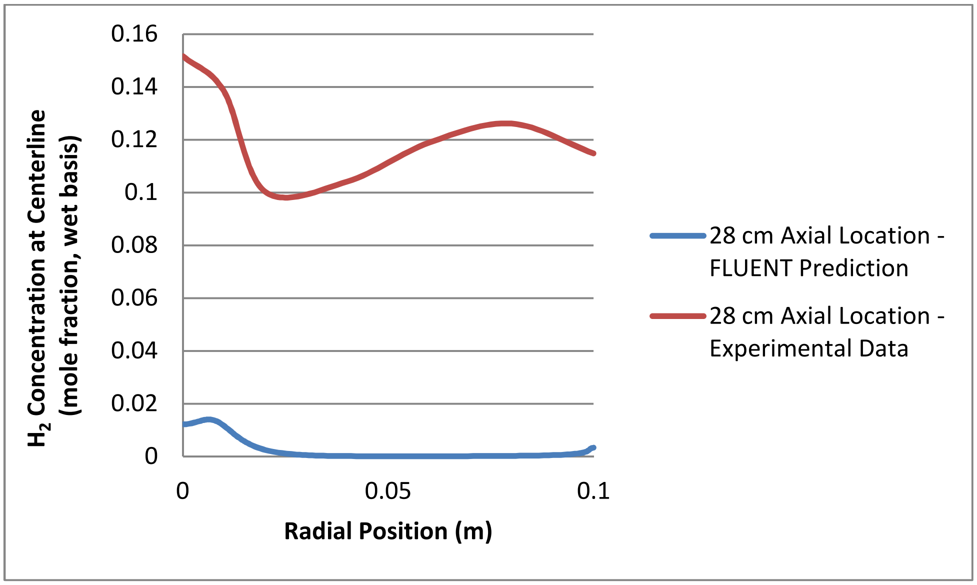

Figure 71: Axial Location 28 cm: Radial profile of H_2 concentration from Brown's 1985 Experimental Data and the "Case 1" FLUENT Predictions

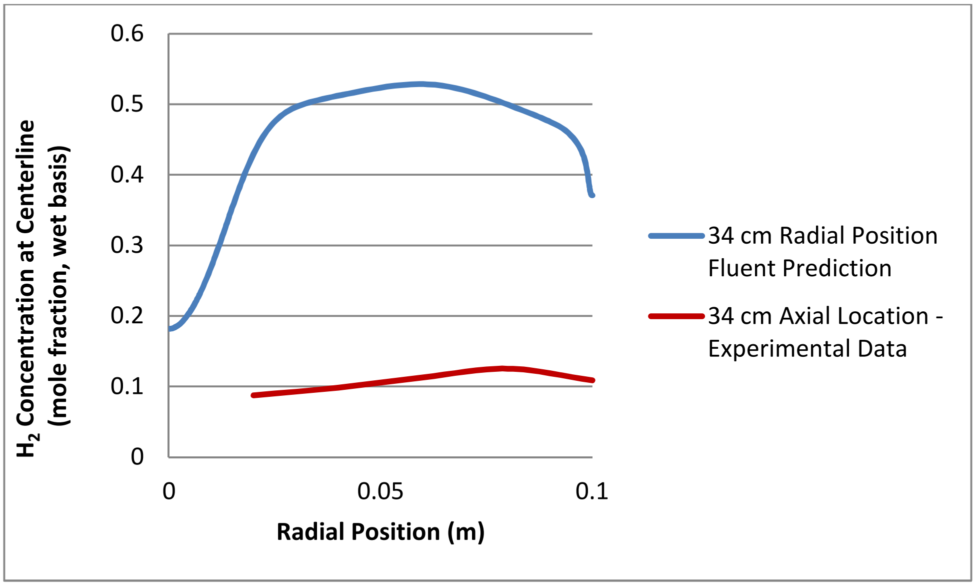

Figure 72: Axial Location 34 cm: Radial profile of H_2 concentration from Brown's 1985 Experimental Data and the "Case 1" FLUENT Predictions

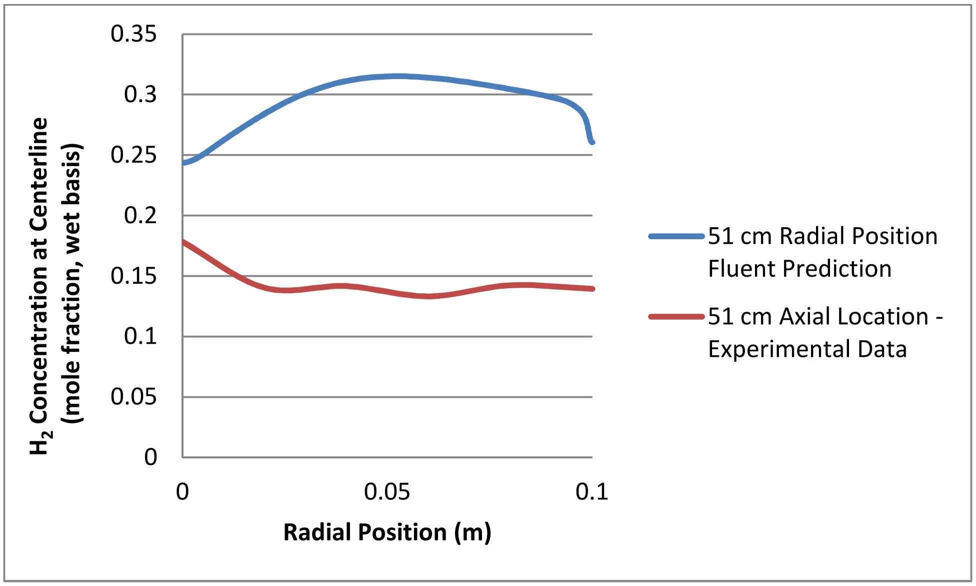

Figure 73: Axial Location 51 cm: Radial profile of H_2 concentration from Brown's 1985 Experimental Data and the "Case 1" FLUENT Predictions

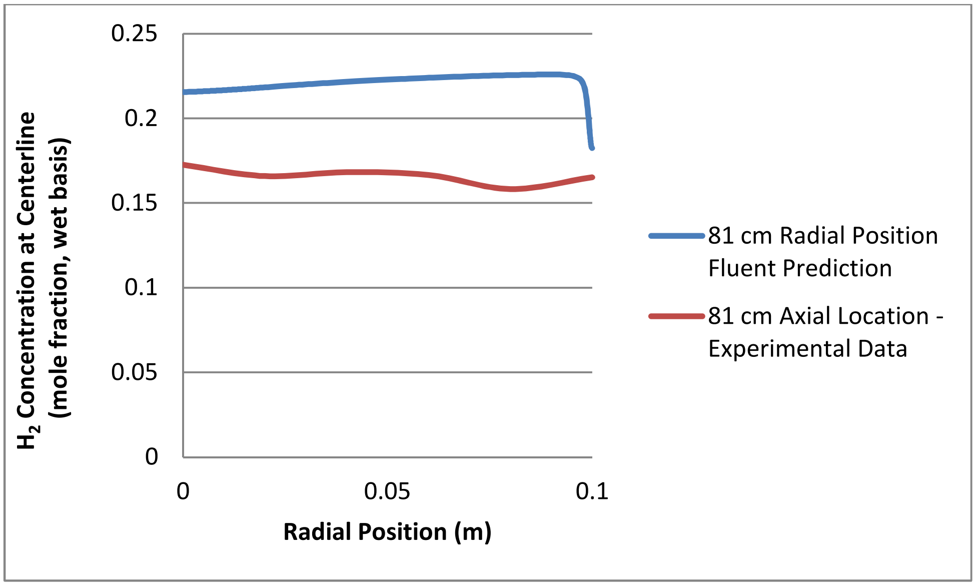

Figure 74: Axial Location 81 cm: Radial profile of H_2 concentration from Brown's 1985 Experimental Data and the "Case 1" FLUENT Predictions

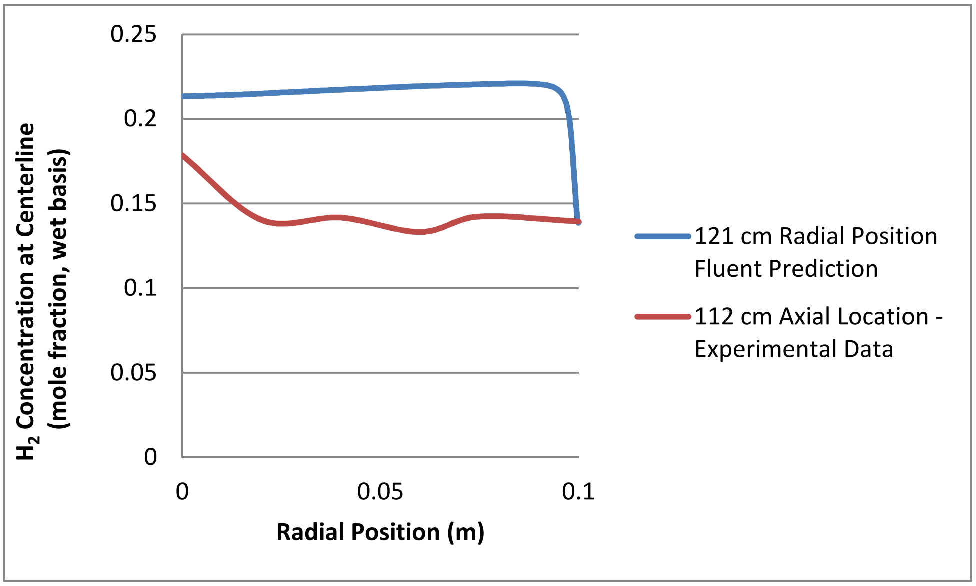

Figure 75: Axial Location 121 cm: Radial profile of H_2 concentration from Brown's 1985 Experimental Data and the "Case 1" FLUENT Predictions

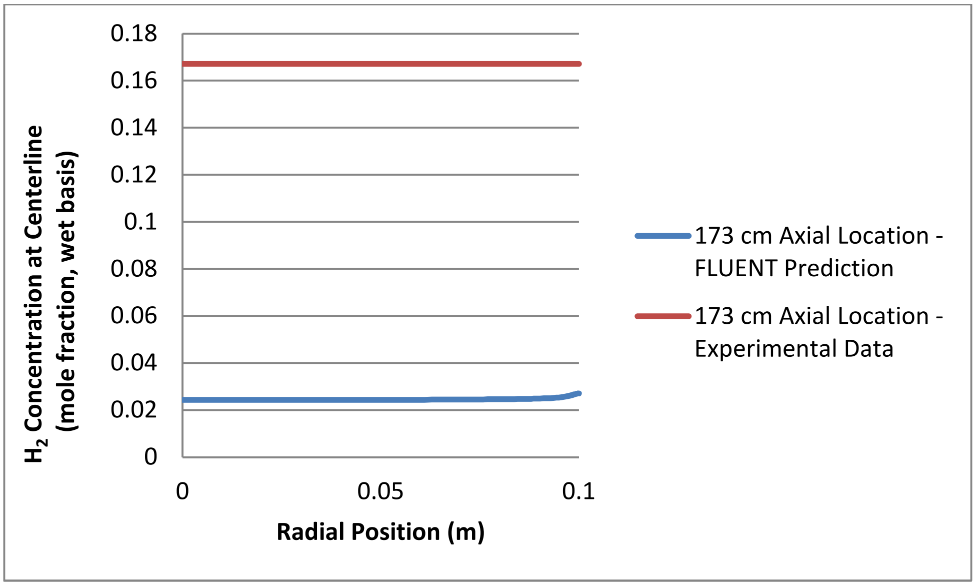

Figure 76: Axial Location 173 cm: Radial profile of H_2 concentration from Brown's 1985 Experimental Data and the "Case 1" FLUENT Predictions

Radial Profiles for O_2 concentration.

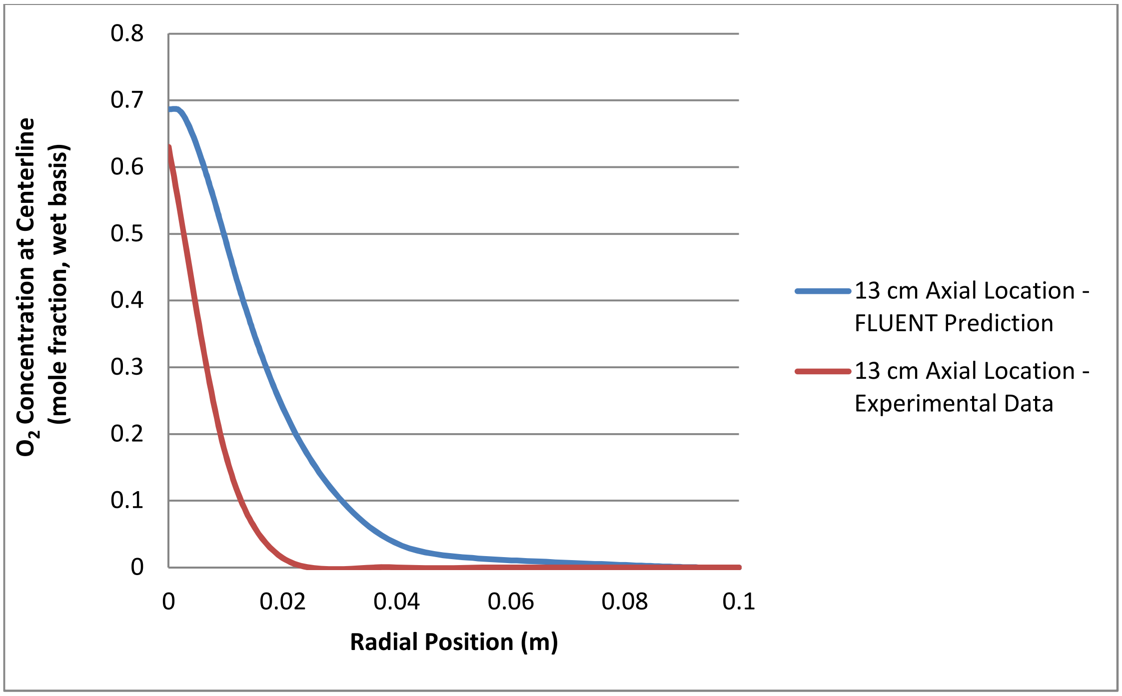

Figure 77: Axial Location 13 cm: Radial profile of O_2 concentration from Brown's 1985 Experimental Data and the "Case 1" FLUENT Predictions

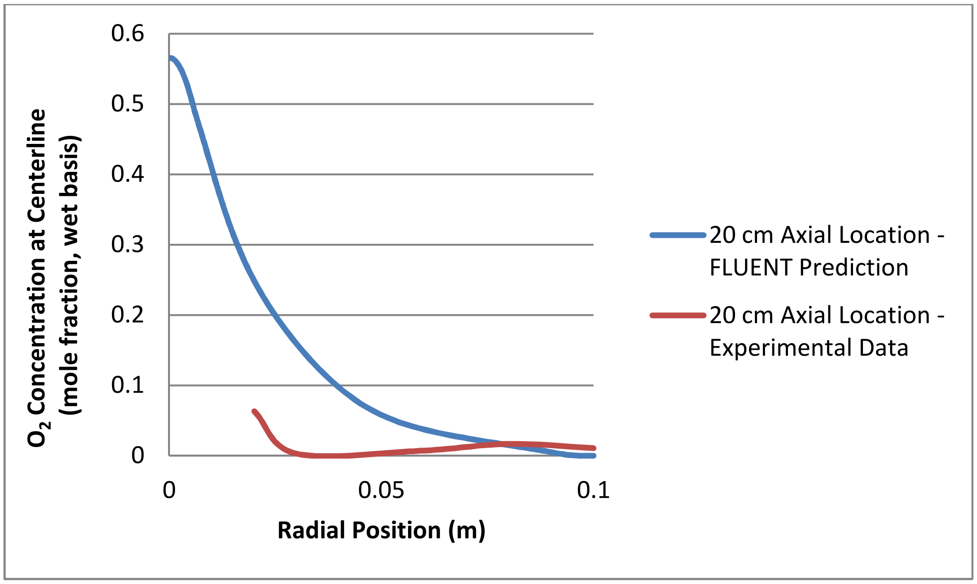

Figure 78: Axial Location 20 cm: Radial profile of O_2 concentration from Brown's 1985 Experimental Data and the "Case 1" FLUENT Predictions

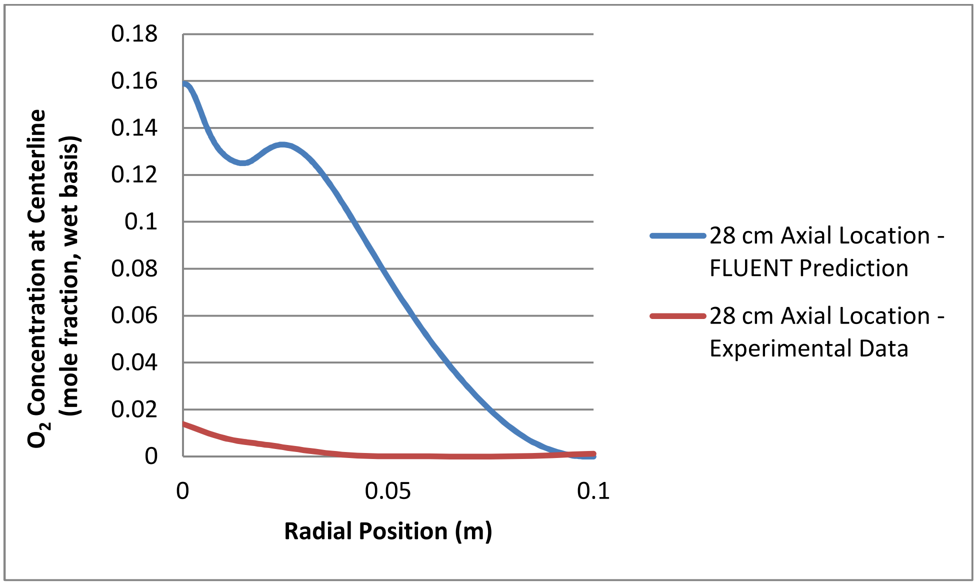

Figure 79: Axial Location 28 cm: Radial profile of O_2 concentration from Brown's 1985 Experimental Data and the "Case 1" FLUENT Predictions

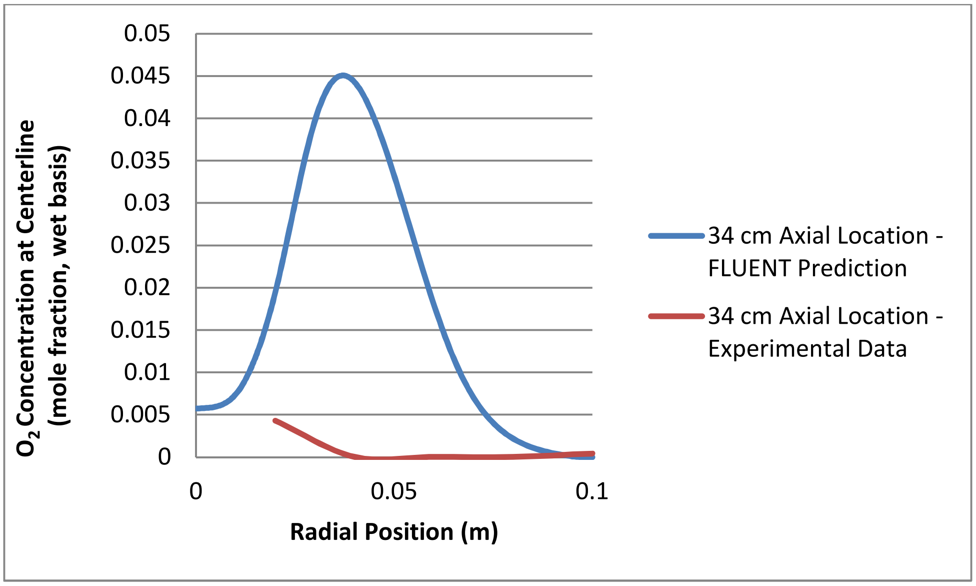

Figure 80: Axial Location 34 cm: Radial profile of O_2 concentration from Brown's 1985 Experimental Data and the "Case 1" FLUENT Predictions

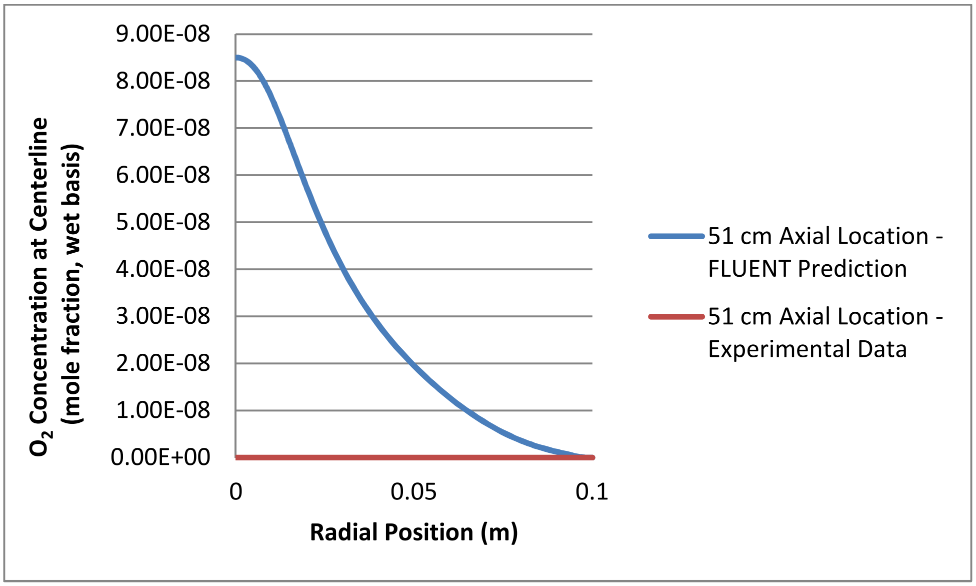

Figure 81: Axial Location 51 cm: Radial profile of O_2 concentration from Brown's 1985 Experimental Data and the "Case 1" FLUENT Predictions

Oxygen concentrations after the 51 cm axial location are under 6×10^{-14} mole fraction (wet basis) and thus can be considered negligable.